2008

Structurally integrated luminescence based oxygen sensors with Organic LED/ oxygen sensitive dye and PECVD grown thin film photodetectors

Debju Ghosh
Iowa State University

Structurally integrated luminescence based oxygen sensors with Organic LED/ oxygen sensitive dye and PECVD grown Thin Film Photodetectors

by

Debju Ghosh

A dissertation submitted to the graduate faculty

in partial fulfillment of the requirements for the degree of

DOCTOR OF PHILOSOPHY

Major: Electrical Engineering

Program of Study Committee:
Vikram Dalal, Major Professor
Gary Tuttle
Joseph Shinar
Mani Mina
Rana Biswas

Iowa State University

Ames, Iowa

2008

TABLE OF CONTENTS

LIST OF FIGURES **v**

ABSTRACT **xi**

CHAPTER 1. INTRODUCTION **1**

1.1 Research Motivation 1

1.2 Types of Oxygen Sensors 2

1.2.1 Resistive Oxygen Sensor 3

1.2.2 Thermoelectric Sensor 3

1.2.3 Automobile Oxygen Sensors 4

1.2.4 Oxygen Probe 6

1.2.5 Paramagnetic Oxygen Sensor 7

1.2.6 Fluorescence quenching based sensing 8

1.3 Scope of research 9

CHAPTER 2. TYPES OF PHOTO DETECTION **10**

2.1 Introduction 10

2.2 Photomultiplier tube 11

2.3 Photodiodes 12

2.3.1 PIN Photodiode 14

2.3.2 Schottky Photodiode 15

2.3.3 Avalanche Photodiode 16

2.3.4 Quantum Dot Photodetectors 18

2.3.5 Nanoparticle photodiode 19

2.3.6 Resonance cavity enhanced photodiode 20

2.3.7 Pyroelectric detectors 20

2.4 Charge Coupled Devices (CCD) 21

CHAPTER 3 LITERATURE REVIEW **22**

3.1 Photoluminescence based sensing 22

3.2 Frequency response of photodiode 28

3.2.1 Factors determining frequency response 28

3.2.2 Methods for measuring frequency response 30

3.2.3 Readout circuits 31

CHAPTER 4: PLASMA CVD DEPOSITION SYSTEMS **32**

4.1 Introduction 32

4.2 ECR (Electron Cyclotron Resonance) deposition 32

4.3 VHF PECVD 34

CHAPTER 5: MATERIALS FOR FABRICATION OF DEVICES **39**

5.1 Introduction 39

5.2 Amorphous Silicon 39

5.3 Amorphous SiGe 41

5.4 Nanocrystalline silicon 42

CHAPTER 6 CHARACTERIZATION TECHNIQUES **45**

6.1 Thickness measurement 45

6.1.1 Optical Measurements 45

6.1.2 Electrical Measurements 46

6.2 Electrical characterization 46

6.2.1 I-V Characteristics 46

6.2.2 Quantum efficiency 47

6.2.3 Capacitance Voltage measurements 50

6.2.4 Frequency response 51

6.3 Crystallinity measurements 51

6.3.1 X-ray Diffraction 51

6.3.2 Raman Spectroscopy 53

CHAPTER 7 SENSOR DESIGN AND FABRICATION **55**

7.1 Sensor design 55

7.2 Integration of the components and challenges 56

7.3 Fabrication process flow 56

7.3.1 Lithography of ITO 57

7.3.2 ZnO deposition 58

7.3.4 Device layer deposition 58

7.3.5 Metallization 58

7.3.6 OLED deposition 58

7.3.7 Encapsulation 59

CHAPTER 8 RESULTS AND DISCUSSIONS **61**

8.1 Sensor design 61

8.2 OLED fabrication and its emission spectrum 62
8.3 Sensor dye film 63
8.4 Optimization and development of photodiodes 64
8.4.1 Transparent contact characterization 64
8.4.2 ECR grown devices 65
8.4.3 Optimization of ZnO layer 68
8.4.4 Effect of adding Germanium 70
8.4.5 Effect of deposition pressure 74
8.4.6 Effect of adding Silicon Carbide on dark current 74
8.4.7 Effect of intrinsic layer thickness 76
8.5 Modes of oxygen sensor operation 77
8.5.1 Intensity mode measurements 79
8.5.2 Effect of intensity on sensitivity 82
8.5.3 Effect of adding titania particles to sensor film 83
8.5.4 Lifetime mode measurement 84
8.5.5 Wavelength dependent frequency response of Photodiode 85
8.6 Frequency response studies 87
8.6.1 Effect of TMB grading in the I layer 88
8.6.2 Effect of boron diffusion at p-i interface during growth 90
8.7 Sensor integration with OLED 93
8.7.1 Effect of excitation frequency on sensitivity 94
8.7.2 Effect of OLED generated noise on sensitivity 95
8.7.3 Shielding of OLED noise 96
8.8 Nanocrystalline devices 99
8.8.1 Effect of hydrogen dilution 99
8.8.2 Factors affecting frequency response of nanocrystalline devices 100
8.9 Sensor performance in the frequency response mode 102
8.10 Nanocrystalline passivation using amorphous silicon 103
8.10.1 Effect of amorphous phase on electrical properties 104
8.10.2 Effect of amorphous phase on frequency response 106
8.10.3 Effect of TMB and hydrogen grading 106
CONCLUSION **108**
FUTURE WORK AND DIRECTIONS **110**
PUBLICATIONS FROM THIS WORK **111**
ACKNOWLEDGEMENTS **112**
REFERENCES **113**

LIST OF FIGURES

Figure 1.1: Resistive type oxygen sensor 3

Figure 1.2: Schematic of Thermoelectric Sensor 4

Figure 1.3: Cross-sectional view of an aperture type limiting current sensor. 5

Figure 1.4 (a): Cross-section of porous layer limiting current sensor. 5

Figure1.4 (b): Limiting current behavior. 5

Figure 1.5: Limiting current sensor configuration 6

Figure 1.6: Cross sectional view of a planar oxygen sensor 6

Figure 1.7: Schematic of Oxygen probe 7

Figure 1.8: Basic Elements of a Paramagnetic Auto-null Balance Oxygen Sensor 8

Figure1.9: Main Elements of Fiber-optic Oxygen Sensor 8

Figure 2.1: Absorbed photons generate electron hole pairs, swept by electric field 10

Figure 2.2: Schematic of Photomultiplier tube 11

Figure 2.3: Photdiode equivalent circuit 14

Figure 2.4 (a): Carriers in pin diode 14

Figure 2.4 (b): Band diagram of pin diode 14

Figure 2.5: Schematic of Schottky photodiode 15

Figure 2.6 (a): Avalanche photodiode 16

Figure 2.6 (b): Avalanche effect 16

Figure 2.7: Avalanche carrier movement 17

Figure 2.8: Noise in avalanche photodiode 17

Figure 2.9: Layer by layer deposition 18

Figure 2.10: Band diagram of the quantum structure 19

Figure 2.11 (a): Nanoparticle device 20

Figure 2.11 (b): Bandgap chart of materials 20

Figure 2.12: Principle of CCD 21

Figure 3.1: Luminescence quenching process by oxygen 22

Figure 3.2: Response for PtOEP in silica glass when switching from 100% N_2 to O_2 23

Figure 3.3: Color variation of the sensor at various oxygen concentrations 24

Figure 3.4: Sensor arrangement (A) LED; (B) deposited sensing film; (C) photodetector 25

Figure 3.5: Schematic of sensor architecture with VSCEL 25

Figure 3.6: Functional block diagram of the electronic system 26

Figure 3.7: Principle of phase fluorometric technique 26

Figure 3.8: Schematic of phase fluorometric sensor 27

Figure 3.9: Phase change of fluorometric sensor at different oxygen concentrations 27

Figure 3.10: Deciphering from photodetctor waveforms 30

Figure 3.11: Dual modulated method 30

Figure 3.12: Test circuit for charge readout 31

Figure 4.1: Schematic of ECR Plasma Reactor 33

Figure 4.2 (a): Stress as a function of plasma excitation frequency and deposition temperature 34

Figure 4.2 (b) Defect density as a function of plasma excitation frequency and deposition temperature 34

Figure 4.3: Dependence of ion energy with excitation frequency 35

Figure 4.4: A schematic of ICP plasma 36

Figure 4.5: Capacitively coupled VHF deposition system 37

Figure 4.6: VHF Plasma Reactor 38

Figure 5.1: A schematic for the model of plasma film deposition 39

Figure 5.2: Density of states of amorphous silicon 40

Figure 5.3: Dependence of collection efficiency on device thickness 40

Figure 5.4: Variation of bandgap with Ge content (x) 41

Figure 5.5: Variation of grain size with hydrogen dilution 42

Figure 5.6: Effect of hydrogen plasma treatment on nanocrystalline growth 43

Figure 5.7: Seed formation and nanocrystalline growth 43

Figure 5.8: Nanocrystalline growth at different dilution R =$[H_2]/[SiH_4]$ 44

Figure 5.9: Schematic representation genesis of powder formation 44

Figure 6.1: Dual beam spectrometer 45

Figure 6.2: Interference spectra in reflectance measurement 45

Figure 6.3: Photodiode under dark and illuminated conditions 47

Figure 6.4: Schematic for Quantum Efficiency setup 48

Figure 6.5: Sample QE of a-Si photodiode 49

Figure 6.6: Kimberling method of defect density estimation 50

Figure 6.7: Interference from crystals planes in XRD 51

Figure 6.8: A typical XRD spectra 52

Figure 6.9: Stokes and antistokes shift in the raman scattering 53

Figure 6.10: Raman spectra from nanocrystalline silicon 54

Figure 7.1: Schematic comparison of front and back detection sensor design 55

Figure 7.2: Design of the developed structurally integrated sensor 56

Figure 7.3: Schematic showing the fabrication process flow 60

Figure 8.1: Schematic of design of the oxygen sensor in front detection 61

Figure 8.2: OLED device structure 62

Figure 8.3: Narrower spectrum for coumarin doped OLED 63

Figure 8.4: Molecular structure of the sensor dye films 63

Figure 8.5 (a): Effect of hydrogen plasma 65

Figure 8.5 (b): ITO after hydrogen plasma treatment 65

Figure 8.6: QE of a-Si device 66

Figure 8.7: Device structure for evaluating the efficacy of using ZnO layer 67

Figure 8.8: Improvement of QE on having ZnO layer 68

Figure 8.9: ZnO resulting in higher dark current 68

Figure 8.10: QE remains unchanged with new ZnO 70

Figure 8.11 (a): No Ge in p+ layer 71

Figure 8.11 (b): Ge in p+ layer 71

Figure 8.12: Comparison of QE of photodetectors 72

Figure 8.13: Comparison of I-V of photodetectors 73

Figure 8.14: Comparison of dark current of photodetectors 73

Figure 8.15: Effect of lower pressure deposition 74

Figure 8.16: Effect of adding silicon carbide at p-i interface 75

Figure 8.17: Effect of adding silicon carbide as window layer 75

Figure 8.18: Effect of I layer thickness on QE 76

Figure 8.19: Different carrier generation position for different wavelengths 77

Figure 8.20: Reduction of dark current with mesa structure 77

Figure 8.21: Experimental setup for quantum efficiency 78

Figure 8.22: Sensor film response detection with photodiode 78

Figure 8.23: PtOEP response under different ambient 79

Figure 8.24: Effect of measurement method on sensor response 80

Figure 8.25: PtOEp and PdOEp sensor dye absorption spectra comparison 81

Figure 8.26: PdOEP response under different ambient 82

Figure 8.27: Independence of sensor response with excitation intensity 83

Figure 8.28: Effect of adding TiO_2 to sensor response 83

Figure 8.29: Scattering of light due to TiO_2 particles 84

Figure 8.30: Lifetime mode of sensor operation 85

Figure 8.31: Response of a-Si device at different wavelengths 85

Figure 8.32: Response of a-SiGe at different wavelengths 86

Figure 8.33 : Comparison of a-Si and a-SiGe device 87

Figure 8.34: Frequency response measurement setup 88

Figure 8.35: Effect of TMB grading on I-V 88

Figure 8.36: Built-in electric field with TMB grading 89

Figure 8.37: Effect of TMB grading on frequency response 89

Figure 8.38: Effect of growth temperature on frequency response 90

Figure 8.39: Boron diffusion during growth 90

Figure 8.40: SIMS profile of the p-i interface 91

Figure 8.41: Improvement of frequency response with structural modification 91

Figure 8.42: Effect of direction of illumination on I-V 92

Figure 8.43: Effect of illumination side on QE 93

Figure 8.44: Effect of frequency in response at different ambient 93

Figure 8.45: Effect of frequency on sensitivity ratio 94

Figure 8.46: Decreasing integrated intensity with higher frequency 94

Figure 8.47: Efficacy of noise shielding 95

Figure 8.48: Effect of applied voltage frequency on OLED generated noise 96

Figure 8.49: Shielding mechanism 96

Figure 8.50: Sensor response with single shield 97

Figure 8.51: Sensor response with double shield 98

Figure 8.52: Improved sensitivity with coumarin doped OLED 98

Figure 8.53: Effect of crystallinity on I-V 99

Figure 8.54: Effect of crystallinity on QE 100

Figure 8.55: Effect of grain boundary defects in frequency response 101

Figure 8.56: Effect of nx-Si p layer thickness frequency response 101

Figure 8.57: Sensor operation in the lifetime mode 102

Figure 8.58: XRD change with higher amorphous content 104

Figure 8.59: Effect of amorphous phase on IV 105

Figure 8.60: Enhanced QE with higher amorphous content 105

Figure 8.61: Frequency response improvement with passivation layers 106

ABSTRACT

There have been increasing efforts for the development of compact and miniaturized oxygen sensor for various applications including multianalyte sensor and sensors with a reliable and accurate monitoring of oxygen concentration in controlled environments requiring measurements under low oxygen concentration. This work has been devoted to the development of structurally integrated luminescence quenching based sensors, the structure comprising of Organic Light Emitting Diode (OLED) as excitation source, oxygen sensitive dyes as the sensing element and PECVD based thin film photodiodes for detection. The whole structure can also be extended towards the development on flexible substrates.

The developed sensor is less cumbersome and bulky and easy to use compared to the existing sensors. The commonly used Clark electrode for measuring dissolved oxygen suffers from interference from the ambient, requires frequent maintenance and electrolyte change, and also consumes oxygen during the measurement resulting in a little inaccurate measurement and hence restricts the resolution of the sensor. In addition the whole set-up is very bulky, which further motivates the development of these luminescence-based sensors. Another advantage of these luminescence-based sensors is the ease of tunability of sensitivity for different oxygen levels merely by changing the sensor dye.

This work has been devoted mainly to the development of appropriate thin film, low temperature grown thin film photodiodes optimized for best possible performance of the whole sensor configuration. In addition the three component integration issues were solved by overcoming all the challenges due to electromagnetic noise generated by the OLED, interfering with the photodiode response and hence limiting the sensitivity.

Amorphous silicon/silicon germanium and nanocrystalline silicon thin films were characterized for better performance in photodiodes. The sensitivity spectrums of the photodiodes were engineered to have maximum sensitivity around 640nm and minimum around 535nm, which is the peak emission wavelength of OLED. This process development resulted in enhanced immunity of the photodiode to the background resulting in enhanced sensitivity.

Two types of detection modes were used: intensity monitoring and PL lifetime monitoring mode. In the intensity mode, the reduction of the PL intensity in presence of oxygen due to quenching effects was monitored. The oxygen sensitive film partially absorbs the OLED light at 535 nm and then it emits at around 640 nm. Two filters were used, one bandpass on top of OLED to reduce the background tail emission followed by the sensor film and then a longpass filter to stop any unabsorbed OLED light. Sensor dyes films were either platinum or palladium based (PtOEP or PdOEP) respectively. A lock-in amplifier was used, to reduce the noise during detection and hence enhancing the sensitivity. But the major challenges were the OLED tail extending to 650nm, which was solved by coumarene doping of the Alq_3 based OLED resulting in narrower spectrum.

The photoluminescence lifetime of the sensor dye film also changes with higher oxygen concentration and thus provides an alternate method of oxygen monitoring. For the PL lifetime based technique, the OLED was pulsed and it was off during the measurement. This resulted in the possibility of elimination of the filters and hence further minimizing and simplifying the sensor configuration. At this point the frequency response of the photodetectors becomes very important and their response time becomes the major issue. Proper impedance matching of the detecting circuit is critical for fast operation of the photodetectors. The boron diffusion during growth was observed to dominantly affect the frequency response, which was partially solved by using nip structure instead of pin structure photodiode. Using nanocrystalline and development of quantum dot photodetectors with amorphous layer grain boundary passivation further improved the response speed. Absolute quantum efficiencies were improved for the detectors. The thin film photodiodes were grown using PECVD, using both ECR (Electron Cyclotron Resonance) and VHF (Very High Frequency) PECVD techniques.

CHAPTER 1. INTRODUCTION

1.1 Research Motivation

There has been demand for structurally integrated field deployable and less cumbersome oxygen sensors. The existing automobile oxygen sensors work at very high temperatures typically around 600^0C and are unusable for biological applications. These sensors also are unusable for the dissolved oxygen estimation. The existing Clark oxygen probes, which works on the electrochemical principle are bulky, uses membranes and require frequent electrolyte replacement and maintenance. Also these probes consume oxygen during the measurement affecting the accuracy especially for low oxygen levels.

The luminescence quenching seems to be the most promising of the sensing techniques due to its non-intrusive nature and its ability to operate at room temperatures. An oxygen sensitive poryphyrin film is exposed to the desired ambient, where its luminescence gets quenched in presence of oxygen. By monitoring the luminescence from the film, the oxygen concentration can be determined. Since the sensing is based on optical monitoring, the actual sensing element and the detection monitoring systems can be totally isolated. Also the oxygen sensitive range is tunable by using different sensor dyes.

Till date this monitoring has been done using fiber optics setup along with laser excitation. But the system has been very bulky and cumbersome. There were some attempts by a group at Stanford University to miniaturize the system by using Vertical Cavity Surface Emitting Laser (VSCEL) and photodetector on a single silicon wafer chip. Also some groups have tried integrating LED and photodetectors[1]. But for better integration, where it will also be possible to fabricate on flexible substrates, Organic LED (OLED) and thin film Plasma Enhanced CVD (PECVD) grown photodetector seems to be the best option. Monitoring the luminescence demands fast and highly sensitive thin film photodetectors, which can be integrated with OLEDs to form the integrated sensor. So it’s first important to understand the factors affecting the detection and also the fabrication conditions which can be used to improve the overall sensor performance.

In addition the thin film photodiodes are becoming important due to the applications in the CMOS sensor arrays and for various other applications. In addition thin film material

characterization is also important for image sensing for especially flexible substrates. There has been some research on the roll-on displays and image sensors [2]. So far many materials have been characterized, including amorphous, nanocrystalline and polycrystalline materials, which is low temperature processed alternatives compared to the conventional crystalline silicon wafer processing. This has opened a new horizon for development especially for large area applications at a lower production cost.

Amorphous silicon has now been used in liquid crystal displays, and has been a host for many other applications. It is a versatile material with a direct bandgap with application limited by the low mobility but is sufficient for display applications. Also it can be reliably grown at very low temperatures (~200C), but suffers from bias stress and light induced degradation effects. Polycrystalline silicon on the other hand has much higher mobilities due to the presence of crystallites, and hence is suitable for high-speed CMOS applications. But it requires processing at higher temperatures. Although there are methods for converting amorphous silicon to polycrystalline silicon using laser induced crystallization where one of the main advantages is being position selective crystallization, which has come to recent interest.

Nanocrystalline silicon is characterized by higher mobility and hence faster response of the photodiodes. But the grain boundary passivation is very critical in these materials and proper characterization is required to improve the passivation and reduce the occurrence of recombination centers resulting in the deterioration of the device performance.

1.2 Types of Oxygen Sensors

First we will have an overview of the status of existing oxygen sensors along with their advantages and disadvantages. Most of the current oxygen sensors are more sensitive for higher oxygen concentrations and the fluorescence and phosphorescence based sensors show tremendous prospect due to their high sensitivity in low oxygen range. The different types of possible oxygen sensors are listed below along with their advantages and limitations.

Types of oxygen sensors

- Resistive Oxygen sensors
- Thermoelectric sensor
- Automobile oxygen sensors
- Oxygen Probe (room temperature)
- Paramagnetic oxygen sensors (room temperature)
- Fluorescence Based Sensing (room temperature)

1.2.1 Resistive Oxygen Sensor

The resistive oxygen sensors [3] are based on change of resistance of the materials in oxygen ambient. The typical materials used are TiO_2 and CeO_2. These sensors work in temperatures much higher than the room temperature. The structure though is very simple comprising of metal contacts and a block of the sensing element as shown in the figure 1.1.

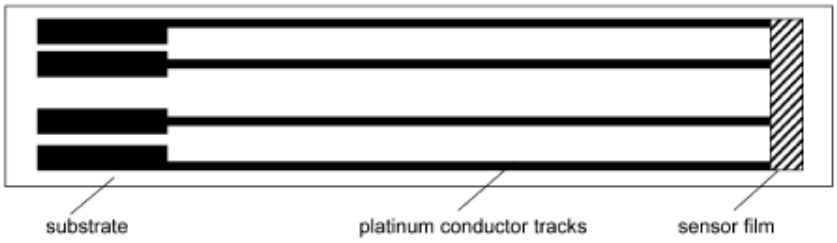

Figure 1.1: Resistive type oxygen sensor [3]

The change of resistance results in a change of current with constant voltage, which can be monitored to estimate the oxygen concentration. This is the most simple oxygen sensor. These sensors are especially sensitive for high oxygen concentration making it ideal for use in automobile industry.

1.2.2 Thermoelectric Sensor

In principle, all materials that are suitable for resistive gas sensing can also be used for direct thermoelectric gas sensors [4]. The electronic Seebeck coefficient and the resistance of materials are influenced by the concentration of the mobile charge carriers, electrons in the conduction band and holes in the valence band. These sensors have its

highest sensitivity at the intrinsic minimum, where electrons and holes concentrations are same resulting in lower temperature dependence of resistance.

Two additional functional elements are required: one heating element to generate temperature difference oscillations, it is denoted by “modulation heater”, second element to determine the temperature difference ΔT precisely. But the response time of the sensor is limited by the thermal response time of the entire gas sensor. A schematic of the thermoelectric sensor is shown in figure 1.2.

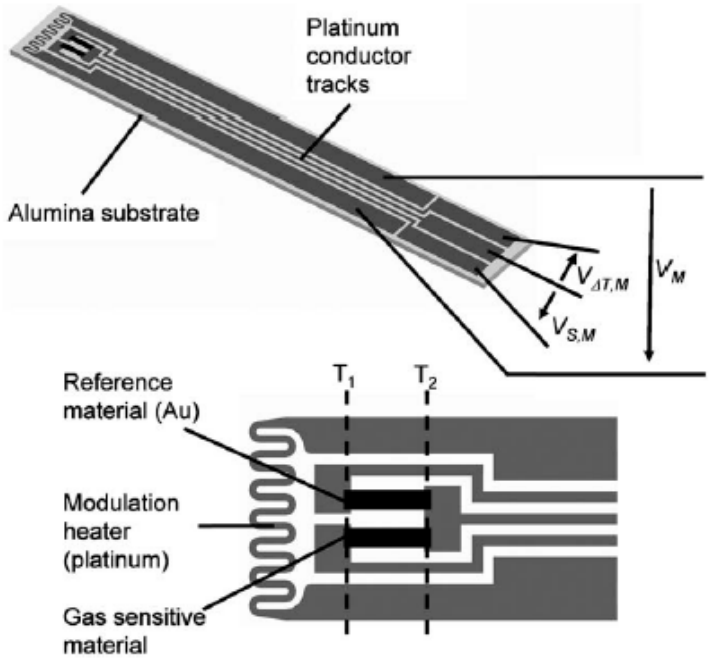

Figure1.2: Schematic of Thermoelectric Sensor [4]

1.2.3 Automobile Oxygen Sensors

The electrochemical zirconia solid electrolyte oxygen sensor is extensively utilized in automobiles to monitor the exhaust gas composition. They are extensively used for high temperature applications. Zirconia oxygen sensors [5], are divided into two classes:

(1) Potentiometric or logarithmic air/fuel sensors

They are suited to monitor the air-to-fuel ratio close to the complete combustion, but are less sensitive to oxygen partial pressure changes away from stoichiometric point due to the logarithmic dependence. These are very reproducible with sensitivity in ppm levels [6].

(2) Amperometric or linear air/fuel sensors.

These sensors can work away from stoichiometry and have higher sensitivity than the potentiometric sensor. These sensors operate on using gas diffusion limited electrochemical pumping of oxygen in a platinum electrode-zirconia electrolyte cell. The sensor current is linearly proportional to the concentration of oxygen. Two types of gas diffusion barriers are currently being evaluated:

- Aperture-type with a small diffusion hole, which is relatively difficult to manufacture as shown in the figure 1.3.

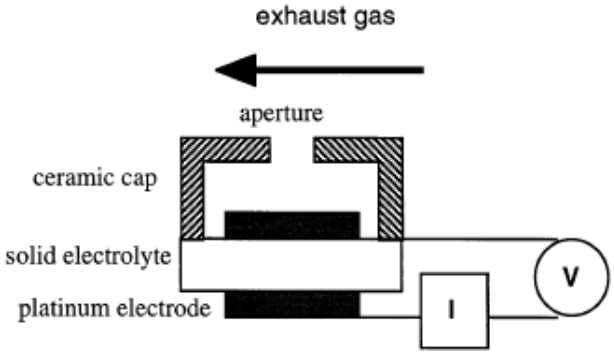

Figure1.3: Cross-sectional view of an aperture type limiting current sensor. [6]

- Porous ceramic layer on the cathode to limit the oxygen transfer rate from the ambient gas. They are easy to manufacture, but control of the porosity is difficult. A schematic is shown in the figure 1.4.

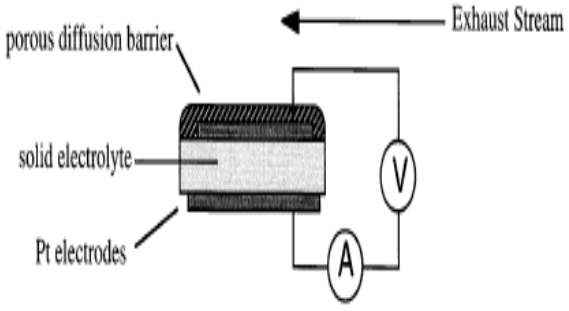

Figure1.4 (a): Cross-section of porous layer limiting current sensor. [6]

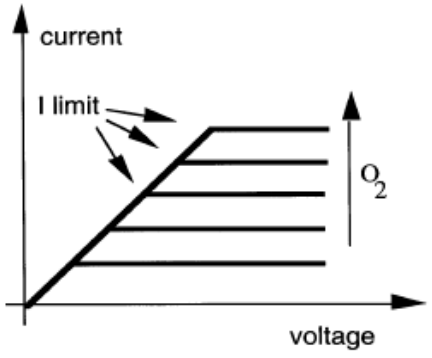

Figure1.4 (b): Limiting current behavior. [6]

The problems associated with pore based diffusion barriers may be overcome by using a mixed electronic and ion-conduction solid membrane as a diffusion barrier [7]. The diffusion of oxygen through the mixed conduction materials is much slower than in a gas, which consequently linearises the sensor performance. A schematic is shown in the figure 1.5.

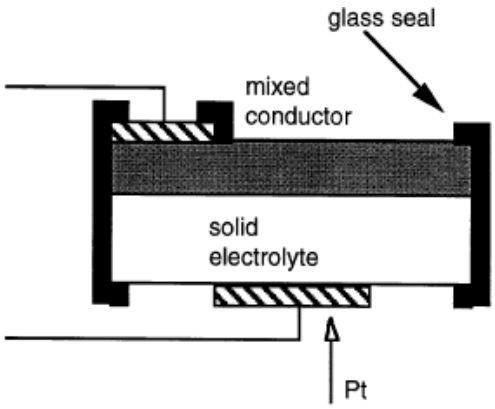

Figure1.5: Limiting current sensor configuration [6]

In 1976, Bosch introduced a YSZ-based oxygen sensor which was unheated O_2 sensor relied on the exhaust gases to reach the operating which was improved by planar sensor with faster response characteristics due to reduced size. Cross sectional view is shown in figure 1.6.

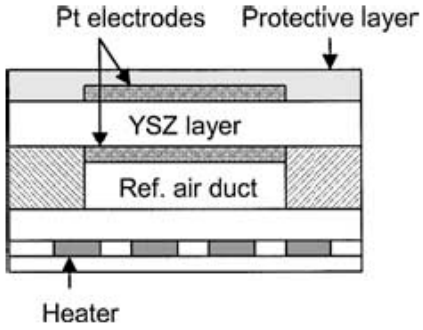

Figure 1.6: Cross sectional view of a planar oxygen sensor [8]

1.2.4 Oxygen Probe

These detectors are based on the change of surface potential with the presence of oxygen ions at the surface [9]. The oxygen potential probe should be made on a micrometer

scale. Since the electrolyte layer on the probe is porous, gas phase oxygen transport is not prohibited. A schematic of the probe is shown in figure 1.7.

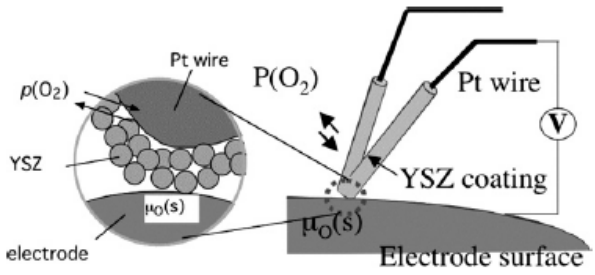

Figure 1.7: Schematic of Oxygen probe [9]

The contact inside the YSZ layer with the Pt–Rh wire gives the reference equilibrium potential. Under current flow, the sample surface may come out of equilibrium from the gas to give a driving force for the surface reaction, when the potential shift can be detected as developed voltage over the porous electrolyte.

Limitations

- This measurement relies on the assumption that the tip of the probe is equilibrated with the sample surface but not with the gas phase. The surface of the probe electrolyte must be catalytically inactive except for the contact point. This requires frequent change and maintenance of the electrolyte
- The probe impedes the oxygen exchange between the sample and the gas phase. The lateral diffusion of oxygen on the sample surface should be fast enough.

1.2.5 Paramagnetic Oxygen Sensor

These sensors exploit the paramagnetic properties of oxygen [10]. It comprises of a dumb-bell made of glass spheres filled with nitrogen having a reflecting mirror in the center and suspended in a strong non-uniform magnetic field. When oxygen is introduced into the chamber, it is attracted towards the stronger part of the magnetic field and alters the dumb-bell motion. It is accurate and interference free but is expensive and cannot be easily miniaturized. The schematic is shown in figure 1.8.

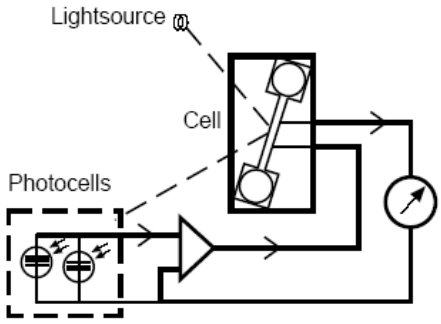

Figure 1.8: Basic Elements of a Paramagnetic Auto-null Balance Oxygen Sensor [10]

1.2.6 Fluorescence quenching based sensing

Most optical chemical oxygen sensors are based on the quenching of the luminescence of an oxygen-sensitive dye by molecular oxygen. The quenching of luminescence is caused by the energy transfer during the collision of O_2 molecule and excited triplet state resulting in singlet state and hence the quenching of luminescence [11]. These sensors are characterized by especially high sensitivity in low oxygen concentrations unlike other sensors. This property makes it extremely useful for monitoring blood oxygen and hence blood glucose concentrations. It will be also useful for monitoring the low oxygen concentrations inside chambers requiring low oxygen levels like aircraft fuel chamber. A typical fiber optic based sensor is shown in figure 1.9.

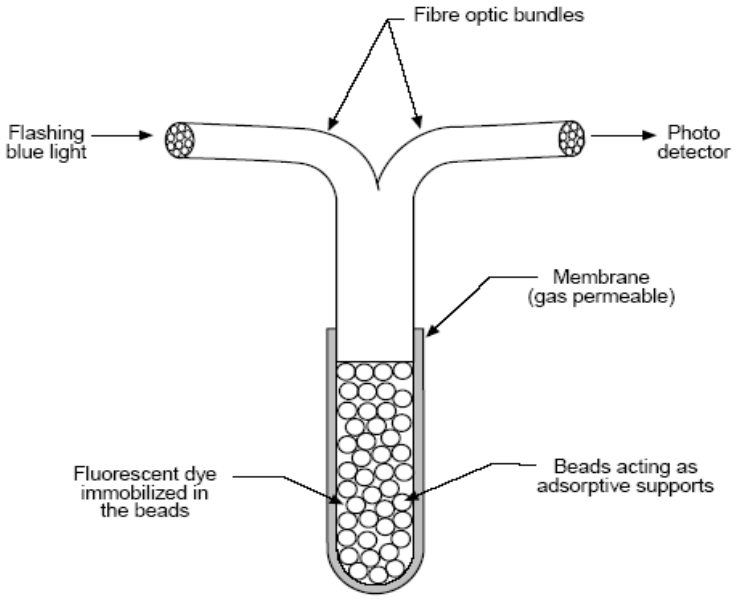

Figure1.9: Main Elements of Fiber-optic Oxygen Sensor [10]

Advantages

- Interference free detection
- Room temperature operation makes ideal for biological application
- Easy miniaturization is possible

The currently existing sensors incorporate lasers as excitation source with optical fibers. This makes the systems very cumbersome and bulky. This detection method has been studied in this work. Efforts have been made to achieve a miniaturized, interference free sensor system for a structurally integrated sensor device. The thin film plasma enhanced CVD grown photodetectors have been studied for their better performance and integration challenges were solved for the oxygen sensing applications.

1.3 Scope of research

In this study, organic light emitting diode (OLED) excitation 535nm (green), an oxygen sensitive photoluminescence film emitting at 640nm and a thin film photodetector was integrated in a single chip to realize a miniaturized and compact sensor configuration. Many challenges such as synchronous noise generation in OLED was the major hindrance in the final integration, which was solved using a transparent electromagnetic shielding that damped this noise and increased the sensitivity of the oxygen sensing unit. In addition the photodiodes were optimized for best possible sensitivity. Two sensing methods, intensity quenching and photoluminescence lifetime shortening methods were utilized for the measurements. The viability of the photodiodes were studied and optimized for highest possible sensitivity. The quantum efficiency spectrum was also engineered to increase the sensitivity in desired wavelengths, also to reduce the sensitivity in the background OLED wavelengths.

CHAPTER 2. TYPES OF PHOTO DETECTION

2.1 Introduction

Photodiodes are used for a huge variety of purposes ranging from telecommunications via optical interlocks to precision photometry. In this work, the silicon photodiode has been utilized for detection of the response obtained from the sensor dye film. The generalized structure of a silicon photodiode is presented in figure 2.1. In practice the depletion layer is intentionally made thicker to facilitate more light absorption compared to p layer, which is usually made as thin to reduce carrier generation in p layer.

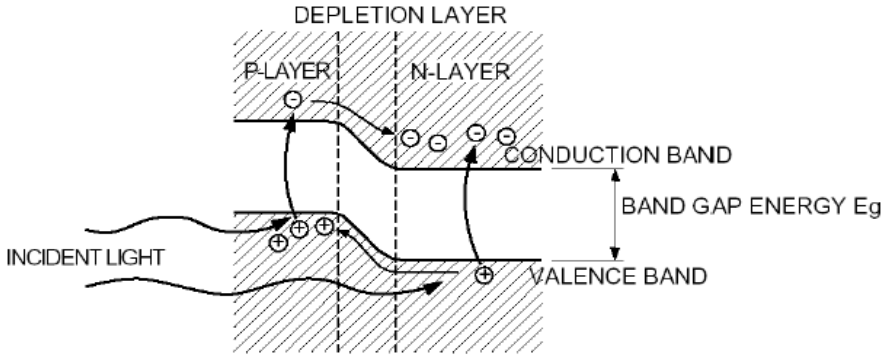

Figure 2.1: Absorbed photons generate electron hole pairs, swept by electric field [12]

Photodiodes work usually under reverse bias condition. In photodiode, electric field across the depletion layer is used for collecting the generated charge carriers unlike solar cells that work with no bias and has to depend on built-in voltage for carrier collection. Ideally the lowest wavelength detected should correspond to the bandgap of the material, but the lowest wavelength point can also be tuned by changing the bandgap and thickness of p layer. For planar devices this is above the depletion zone, where, due to surface recombination the minority carriers have very short diffusion lengths – the carriers generated above the depletion zone are recombined before they can diffuse to the depletion zone. The protective layers on top of the photodiode can also influence the short wavelength limit, where short wavelengths may suffer from significant reflection and absorption losses. The types of photodetectors are listed in the latter paragraphs.

Photo detection is also possible by capacitive methods of detection. In this method the variation of capacitance is measured by variation of capacitance under dark and illuminated conditions [13]. This detection methodology is especially good for infrared detection up to 2400nm under forward bias at low temperature ~ 198K as reported by Wind and Miller [14].

2.2 Photomultiplier tube

The first photoelectric tube was produced in 1913 by Elster and Geiter, but the first photomultiplier tube was invented by the RCA laboratories in 1936 and became a commercial product. Further innovations such as metal-channel dynodes, mesh dynodes and micro channel plates have resulted in higher sensitivity and new capabilities.

Photomultipliers have a light transmitting window covered at the inner side by a semitransparent photocathode which is made from a thin layer of semiconductor material, some focusing electrodes and a number of so-called dynodes for the electron multiplication. The mechanics is complicated; need hand-work and makes photomultipliers rather expensive. In Fig.2.2 the cross-section of a typical photomultiplier is shown.

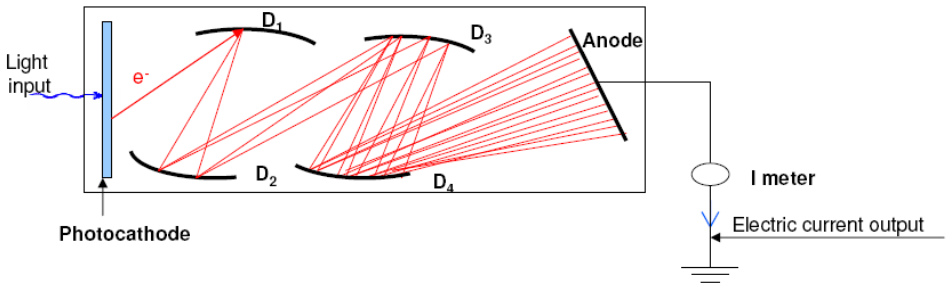

Figure 2.2: Schematic of Photomultiplier tube

The main characteristic of a photomultiplier is its high quantum efficiency (QE), which describes the probability that a photon creates an output signal. The amplification in a photomultiplier depends on the number of dynodes, the dynode material and the electric potential between the dynodes. Dynode material is a metal sheet made of copper and beryllium. A photomultiplier with 12 stages has thus a gain of 10^6 – 10^7, resulting in one of the highest sensitivity of all light detecting sources.

Advantages

- Large gain > 10^6
- Low internal noise introduced
- High bandwidth ~ GHz

Disadvantages

- Large size and limited lifetime
- Fragile and needs high operating voltages

2.3 Photodiodes

The important parameters are diffusion length, quantum efficiency, responsivity, response speed, temperature effects and noise. Typically photodiodes are operated under reverse bias.

Diffusion length

Diffusion length depends on diffusion constant and the carrier lifetime. It is an indicator of the length the carrier will travel without recombination. The relation for diffusion length is given by equation 2.1

$$L = \sqrt{D\tau} \tag{2.1}$$

Quantum efficiency

It's an indicator of number of electron-hole pairs generated with an incident photon. The maximum value for the quantity is unity.

$$\eta = \left(\frac{I_p}{q}\right)\left(\frac{P_0}{h\nu}\right) \tag{2.2}$$

Where I_p is the photocurrent, q is the charge of an electron; P_o is the incident power and ν is the frequency of the incident light.

Responsivity

Responsivity is the measure of sensitivity of the photodiode. The relation is given by equation 2.3.

$$\Re = I_p/P_o \tag{2.3}$$

In order to increase responsivity, the absorption of the material should be high; depletion width should be high and junction close to the surface. There should be antireflective layer at the surface.

The responsivity of a photodiode can also be tuned by interfacial layers and bandgap engineering of the subsequent layers. The response of the device can be also tuned by varying the bias in the device[15].

Response speed

Response speed is mainly limited by three factors: charge collection time slow diffusion of carriers and RC time constant. The RC time constant is determined by the capacitance and also by the resistance either due to the device or due to external load. The response time in turn affects the bandwidth of the detector.

Temperature effects

There is shift in quantum efficiency at higher temperatures and also the dark current increases affecting the reliability of device. The dark current can be reduced by bandgap engineering and also by introduction of SiC at p-i interface [16].

Noise

Shot noise is one of the dominant noises in the photodetector. The shot noise comprises of three components, photocurrent noise, dark bulk and surface noise. So the expression is given by equation 2.4.

$$I_S^2 = I_{S,photo}^2 + I_{S,dark}^2 + I_{S,surface}^2 \tag{2.4}$$

There is also Johnson noise, due to random movement of free electron. The expression is given below:

$$I_T = \sqrt{\frac{4kT.BW}{R}} \qquad (2.5)$$

Equivalent Circuit

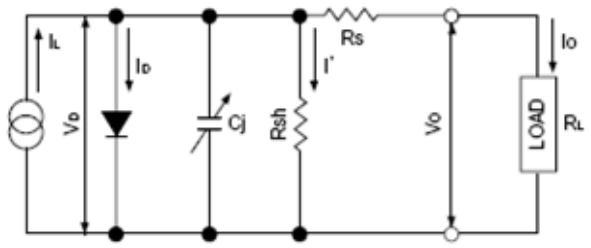

Figure 2.3: Photdiode equivalent circuit

I_L : Light generated current
I_D : Diode current
C_j : Junction capacitance
R_{sh} : Shunt resistance
R_s : Series resistance
I' : Shunt resistance current
V_D : Voltage across diode

Using the above equivalent circuit, the output current Io is given by equation 2.5.

$$I_o = I_L - I_s(\exp\frac{qV_D}{kT} - 1) - I' \qquad (2.5)$$

2.3.1 PIN Photodiode

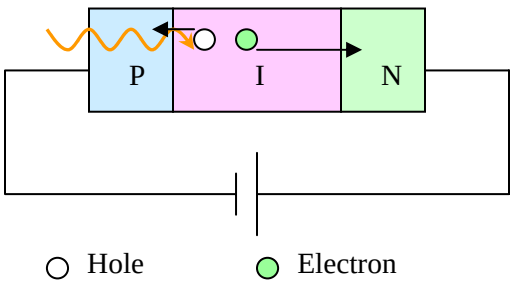

Figure 2.4 (a): Carriers in pin diode

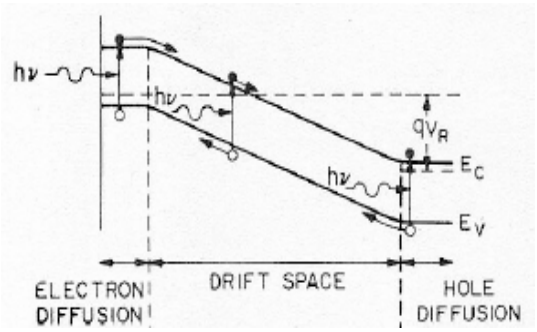

Figure 2.4 (b): Band diagram of pin diode

The absorbed photon generates electron-hole pair, which is collected by n, and p layers respectively due to the applied bias resulting in photocurrent and the consequent light detection. The absorbed light has to greater then bandgap of the material. The reverse bias ascertains that the intrinsic region is fully depleted.

Advantages

- Easy to fabricate
- High quantum efficiency due to better absorption in I layer

- Lower capacitance due to thicker I layer ➔ faster speed
- The QE can be tuned with different I layer thickness
- Low wavelength QE can be tuned by p layer thickness
- Collection dependence with bias is lower

Disadvantages

- The p-i and n-i junctions very critical to device performance
- p-i and n-i junctions are effective recombination centers
- Carrier transit time become dominant at higher thickness reducing speed
- Electric field is lower hampering carrier collection

2.3.2 Schottky Photodiode

It comprises of metal semiconductor junction acting as a rectifying contact. Its one of the fastest photodiode, but problem is the poor quantum efficiency. There are two ways of generation of photocurrent: band-to-band generation and electron photocurrent. The diode is extremely fast since it comprises of only a single junction as shown in the figure 2.5.

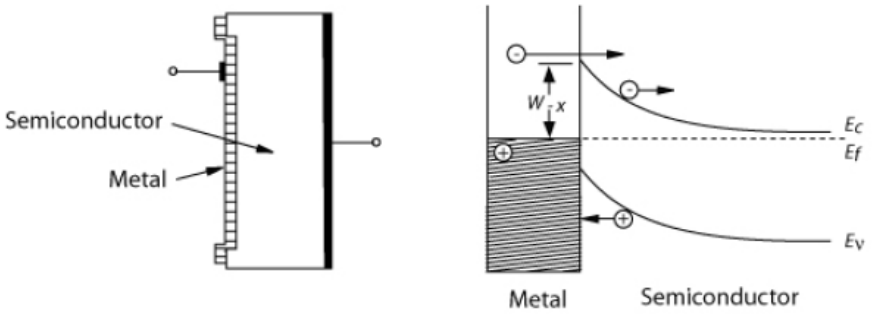

Figure 2.5: Schematic of Schottky photodiode

Advantages

- Very fast response

Disadvantages

- Low QE due to lower depletion width
- Doping level very critical

2.3.3 Avalanche Photodiode

Avalanche Photodiodes (APD) are high speed, high sensitivity photodiodes utilizing internal gain mechanism under reverse bias. The APD internally multiplies the photocurrent resulting in more sensitivity than p-i-n diode. The diode is polarized above its breakdown voltage resulting electron-hole pairs to be further accelerated by high fields resulting in impact ionization. The diode structure and the process are shown in the figure 2.6.

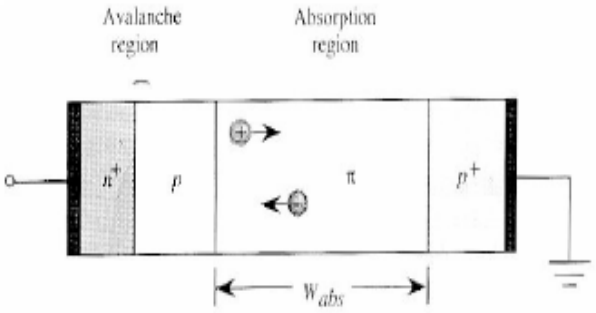

Figure 2.6 (a): Avalanche photodiode

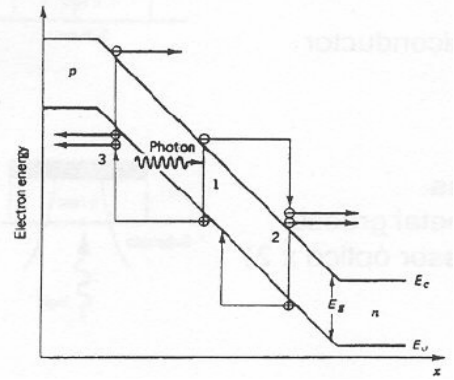

Figure 2.6 (b): Avalanche effect

The avalanche multiplications begin to take place when the electric field reaches 2 x 10^6V/cm. Typically the gain is higher for higher reverse voltage. However for higher voltage, voltage drops occurs due to the current flowing though the device, resulting in decreases avalanche layer [17]. Also the gain tends to reduce at higher temperatures. Also the spectral response tends to change with reverse bias. The ratio of ionization rate of holes to that of electrons is called ionization ratio, which is an indicator of device noise. The terminal capacitance is not temperature dependent, but reduces at higher reverse voltages resulting in faster response as shown in the figure 2.7.

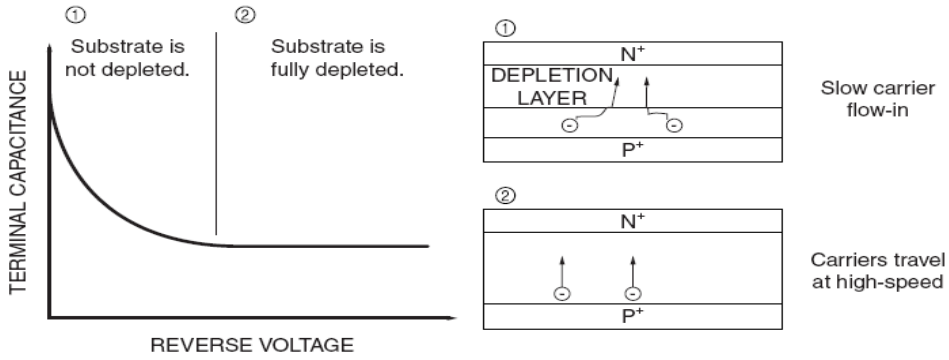

Figure 2.7: Avalanche carrier movement

However, the thermal noise generally determines the lower limit for light detection. A typical variation of thermal and shot noise is shown in figure 2.8.

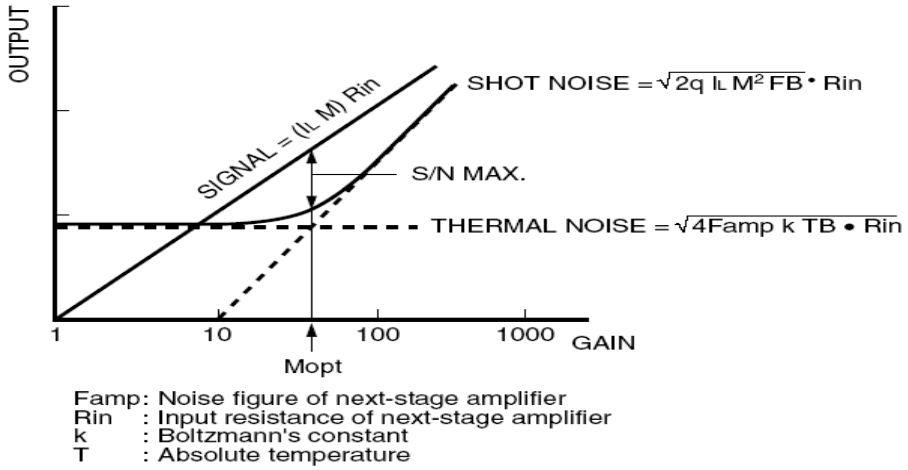

Figure 2.8: Noise in avalanche photodiode

Advantages

- Very fast response
- Internal gain resulting in better sensitivity

Disadvantages

- Noise also gets multiplied by the avalanche effect
- The dark current is higher for higher gain
- Gain changes with temperature
- The spectral response changes with different reverse voltages
- Consume more power than PIN

2.3.4 Quantum Dot Photodetectors

They are ideal because of their tunable, narrowband response, obtained in point detectors and focal plane arrays. Using epitaxial growth techniques, each with an independent electrical readout, can be stacked vertically in a pixel to provide multi-spectral sensing. Below is a schematic of growth using layer by layer technique is shown in figure 2.9. At this small dimension, the quantum effect starts affecting the characteristics of the devices. The sizes of this quantum dots are typically 2 to 4nm.

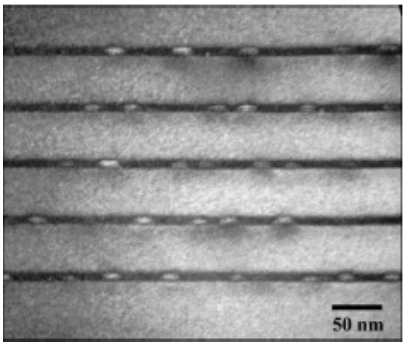

Figure 2.9: Layer by layer deposition

Advantages

- Narrow wavelength spectrum response
- The sensitivity wavelength can be tuned by the size of quantum dot

Disadvantages

- Difficult to fabricate
- Alignment of the dots very hard to control
- The dot size tend to change in a-Si and nx-Si interface
- Too thick separating layers can result in tunneling problems

The quantum well is formed by the nanocrystalline silicon which has lower bandgap compared to the amorphous silicon. Typically for quantum devices, insulators are used as higher bandgap material. But those devices suffer from carrier collection problem, restricting the thickness of the insulator layers. The band diagram is shown in the figure 2.10:

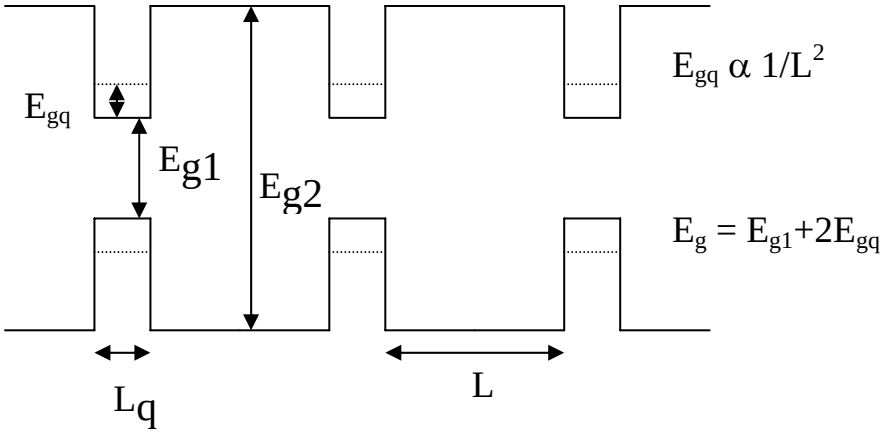

Figure 2.10: Band diagram of the quantum structure

2.3.5 Nanoparticle photodiode

The Si nanoparticle photodetectors are hot area especially for the UV detection. The Si nanoparticles are dispersed from the Si wafer by electrochemical etching [6]. Typically Si with a bandgap of ~1.1 eV has a pretty good response around 700-800 nm. But with nanoparticles it shows quite a decent response in the UV region. The nanoparticles show direct bandgap like characteristics and hence resulting in a higher effective bandgap and better UV response. This is also the basic principle behind the revolutionary Si based laser technology from indirect bandgap materials.

Contrary to bulk Si or large particles, the electron hole pairs do not appreciably recombine via nonradiative processes, allowing charge separation and collection. Nonradiative recombination is not strong in ultra-small Si nanoparticles due to strong quantum confinement. The schematic of the photodiode along with the bandgap of the particle is given in figure 2.11

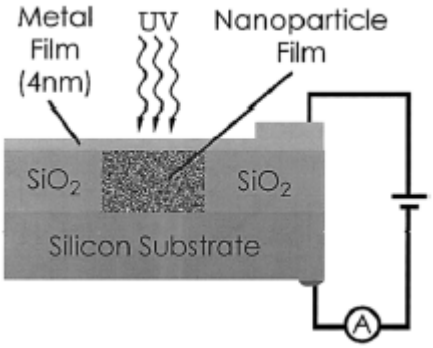

Figure 2.11 (a): Nanoparticle device [18]

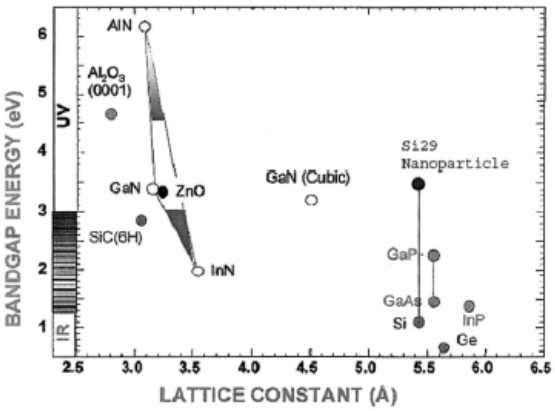

Figure 2.11 (b): Bandgap chart of materials

Advantages

- Enhanced responsivity
- Lower thickness can be used
- Particle size doesn't need to be controlled

Disadvantages

- No control on degree of packing of particles
- More susceptible to non-uniformity and cracks

2.3.6 Resonance cavity enhanced photodiode

Resonant enhanced photodetector is the latest type, which has being experimented with for high sensitivity. It involves Fabry-Perot resonator, resulting in higher quantum efficiency and a much narrower detection band. The narrow band gives extremely high noise margin, but is much more difficult to fabricate.

2.3.7 Pyroelectric detectors

Detector absorb photon ➔ changes temperature ➔ dielectric constant change

The change in dielectric constant is indicated in the capacitance, typically resulting in a flat response over a range of temperature, but the detector is very slow.

2.4 Charge Coupled Devices (CCD)

It consists of detector array to detect entire image. The charge needs to transfer from one detector to another and then to electronic storage. There are different clock voltages shifted in time to facilitate the transfer. This type of waveform is called push clock. The process is very similar to the movement of ship in the Panama Canal. The charges are read along the bit line and hence the total intensity is estimated. The principle of working of CCD is shown in figure 2.12.

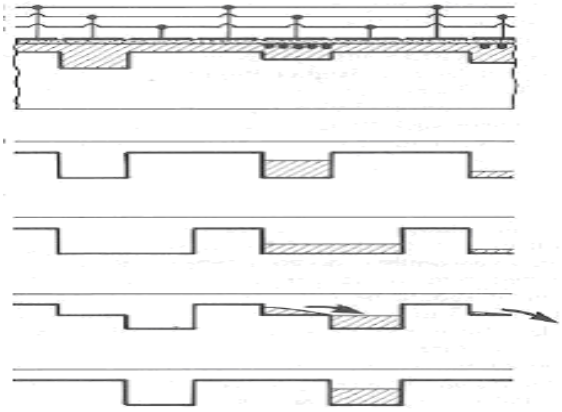

Figure 2.12: Principle of CCD

The CCD technology has been in a very advanced stage of development. It’s still dominant in the cameras. The CMOS image sensors are providing a competition, but they are still behind in terms of the image quality. It is the cost of fabricating which is the driving force towards the development of the CMOS imagers.

CHAPTER 3 LITERATURE REVIEW

3.1 Photoluminescence based sensing

The photoluminescence based oxygen sensing is based on the principle of quenching of the luminescence from the lumophores due to collision with the oxygen molecules. Due to the collision, the energy of the excited triplet state gets transferred to the oxygen molecule resulting in quenching of radiation from the lumophores. The process is shown in the figure 3.1.

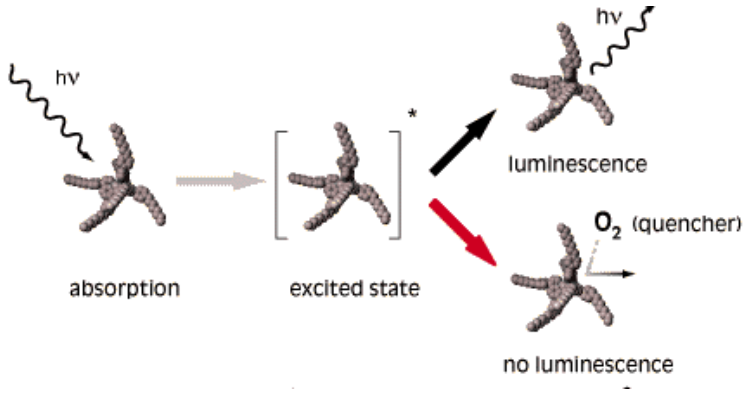

Figure 3.1: Luminescence quenching process by oxygen [19]

The quenching of the luminescence by the presence of oxygen is monitored for the oxygen sensing capabilities. The quenching is characterized by Stern-Volmer equation as shown in equation 3.1. The intensity quenching is also along with reduction of decay lifetime.

$$\frac{I_O}{I} = 1 + K_{SV}.P_{Oxygen} \tag{3.1}$$

So we see that the quenching is also dependent on the partial pressure of oxygen. The typical polymers dyes used are Ru doped, Pt doped and Pd doped films. The sensitivities of those dyes are given in the table 3.1 [6]:

Table 3.1: Sensitivity comparison of different oxygen sensitive dyes

Lumophore	Polymer	Natural life-time $\tau_0(\mu s)$	Oxygen sensitivity, K_{SV}
Fluoranthene	Vycor glass	–	0.003
$[Ru(bpy)_3^{2+} (ClO_4^-)_2]$	Silicon rubber-RTV 118	0.62	0.003
$[Ru(phen)_3^{2+} (ClO_4^-)_2]$	–do–	0.92	0.009
$[Ru(ph_2phen)_3^{2+} (ClO_4^-)_2]$	–do–	5.3	0.033
–do–	Poly(acrylic acid)	–	0.0015
–do–	Poly(sodium 4-styrene sulfonate)	–	0.002
PtOEP	Ethyl cellulose	81	0.196
PdOEP	–do–	1410	3.475

We see that the Pt doped dye is most sensitive along with the longest lifetime resulting in lower requirement of frequency response of the photodetector used. A typical response of PtOEp film under N_2 and O_2 ambient is shown in the figure 3.2

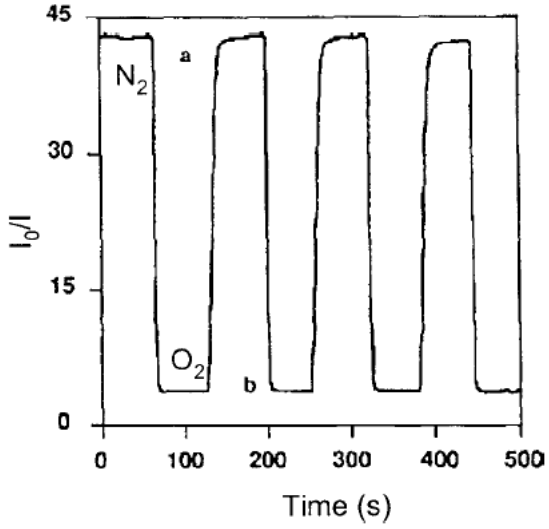

Figure 3.2: Response for PtOEP in silica glass when switching from 100% N_2 to O_2 [6]

The lifetime based sensing have obvious advantage over intensity based sensing. The main advantage being immune to excitation intensity variation, which may vary with time due to degradation of effects of both the sensor dye film and the excitation source. The recent initiative of using OLED as excitation source due to its easy tunability has made the excitation source degradation even more important. Importantly, the lifetime method provides a possibility to expand the sensitive analyte concentration range using probes with spectral shifts. But florescence method provides a non contact way of monitoring.

PtOEP (Platinum octaethylporphyrin) in polystyrene film has a strong absorption band around 383 nm and a weaker one at 535 nm, with the maximum luminescent wavelength at 647 nm [20]. PtOEp (Palladium octaethylporphyrin) has absorption near 535nm compared to 550nm for PdOEp. People have also tried other derivatives to PtOEp to make it absorb around 591nm to make it useful with the available leds [20]. The use of OLED brings tenability to the excitation source. It has been seen that high concentration of ammonia and nitrous oxide has some interference in oxygen concentration.

There has been another group working on the development of color based oxygen sensor, where the color of the dye is dependent on the oxygen concentration [21]. But the resolution of this type of sensor is limited by the spectral color resolution of the sensor dye as shown in the figure 3.3.

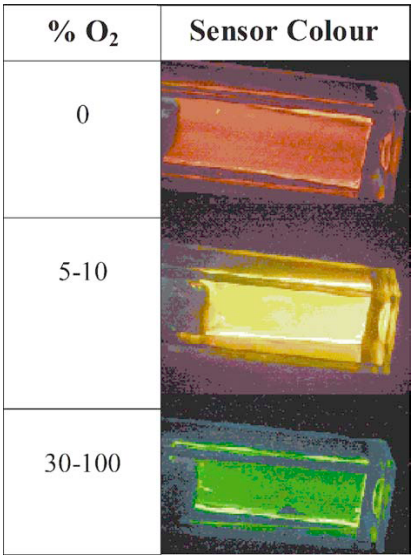

Figure 3.3: Color variation of the sensor at various oxygen concentrations [21]

One of the other most commonly used methods for oxygen monitoring in the phase resolved measurement technique, which is turn is pretty similar to lifetime measurements. Here we monitor the change of phase and hence make it independent of the intensity of the excitation source. Recently one group in Spain is developing portable oxygen sensors incorporating a commercial LED using PtOEp as sensor and then the photodetector at the back for oxygen detection [22]. A filter is incorporated between the sensor and the

photodetector to cut off the LED background. The schematic of the setup is shown in the figure 3.4.

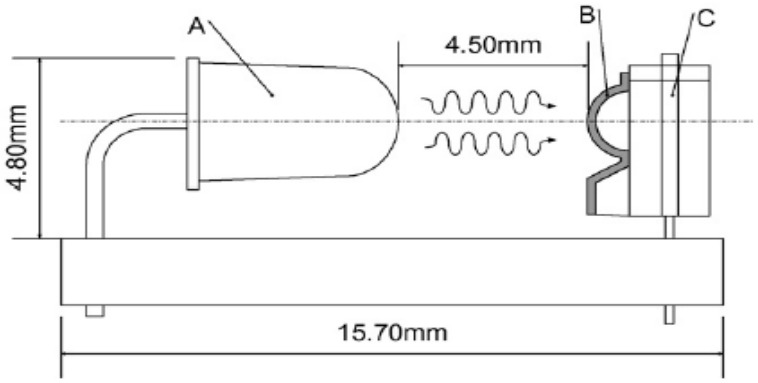

Figure 3.4: Sensor arrangement (A) LED; (B) deposited sensing film; (C) photodetector [1]

There is also significant research going on Stanford University by Thrush et. al where VSCEL (vertical cavity surface emitting laser) has been integrated with a photodiode array to achieve integrated luminescence based sensor for biosensing applications. The schematic of the sensor is shown in the figure 3.5

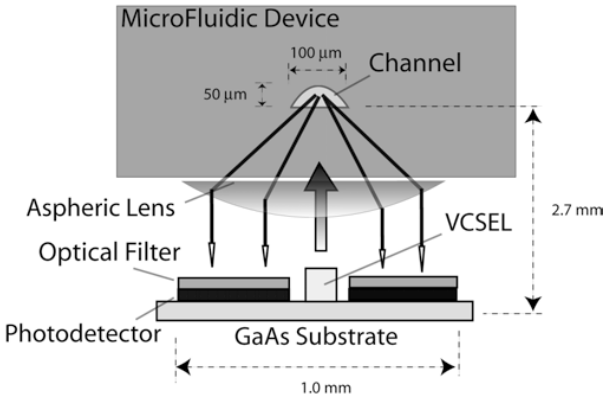

Figure 3.5: Schematic of sensor architecture with VSCEL [23]

This arrangement is the compact form suggested till date, but it is still not integrated to a single chip as being tried in the current scope of this work. Considering the complexity for the instrumentation for lifetime measurements, frequency domain offers several advantages as compared to time-domain measurement techniques [24]. The arrangement comprises of two LEDs working at different frequencies and hence having the modulating effect. A schematic is shown in the figure 3.6.

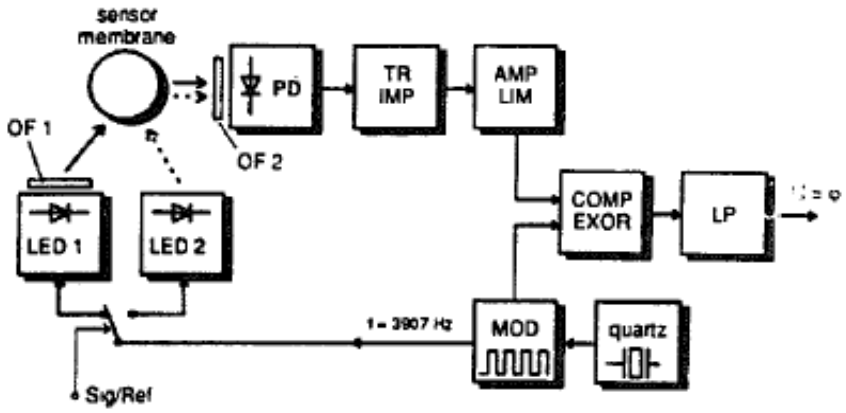

Figure 3.6: Functional block diagram of the electronic system [24]

The advantage is that the instrumentation bandwidth can be theoretically reduced as much as desired resulting in better noise ratio with least effect of background scattering. The change of phase is more significant for lower oxygen concentrations than for higher concentrations. The principle of working of this method is shown in the figure 3.7 [25].

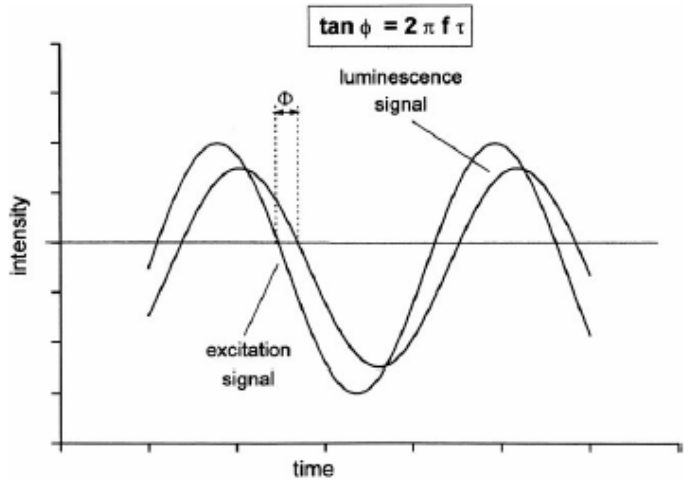

Figure 3.7: Principle of phase fluorometric technique [25]

The sensor used was based on xerogel sensing layer with the use of appropriate filter. LED was used as the excitation source and the gasses were flown in the chamber. The sensor structure is shown in the figure 3.8.

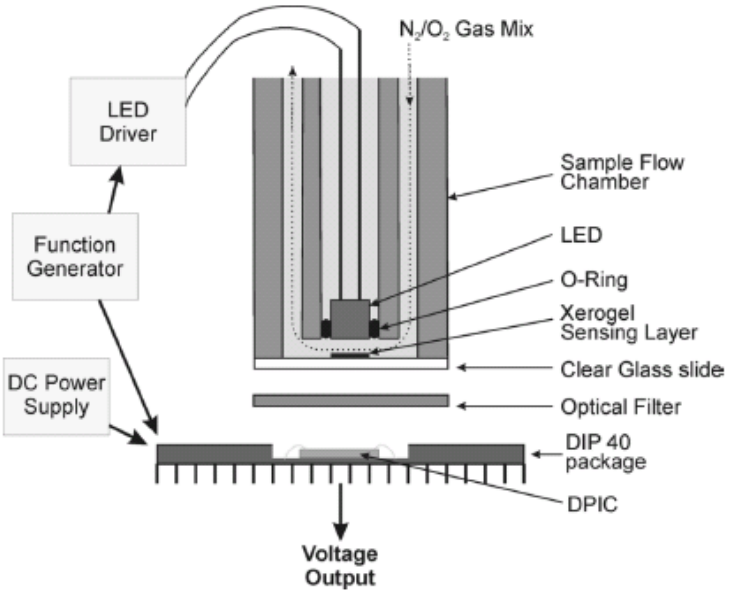

Figure 3.8: Schematic of phase fluorometric sensor [26]

The phase difference measured by the sensor is also dependent on the frequency used for the measurements for best spectral resolution; the lifetime of the sensitive dye should be of the order of the time period corresponding to the excitation frequency. The phase shift obtained for the sensor is shown in the figure 3.9.

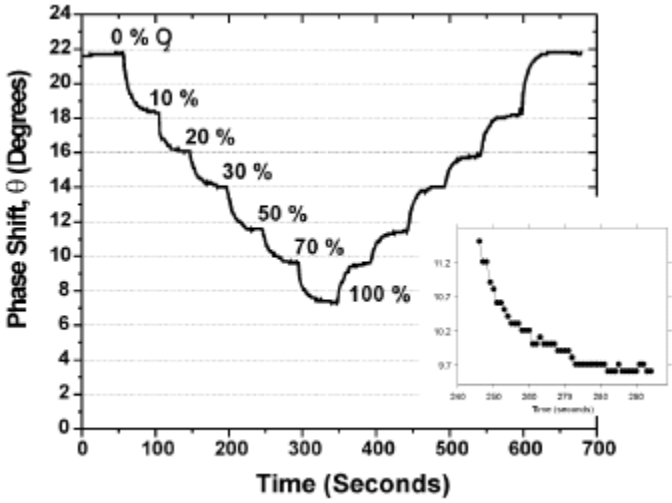

Figure 3.9: Phase change of fluorometric sensor at different oxygen concentrations [26]

For the lifetime-based measurements, we start the measurement after the excitation source is off. So we put a pulse of excitation light and then measure the lifetime of sensor response after the sensor is off. This method is independent of the excitation intensity and

hence is tolerant of any degradation effects of both light source and sensor films. The sensors films like PtOEp and PdOEP are well known to show photobleeching and they degrade with time in illuminated conditions. For this reason the lifetime method seems to work out best for these types of sensors. But the lifetime method requires the photodetectors to be fast and also requires complicated circuit to accomplish the same. For this reason the frequency response of the photodetectors become really important especially when we are using integrated thin film sensors made of amorphous Si and amorphous SiGe. This makes the study of plasma enhanced CVD grown photodetectors very important.

3.2 Frequency response of photodiode

3.2.1 Factors determining frequency response

The response speed of a photodiode is a measure of the time required for the accumulated charge to become an external current and is generally expressed as the rise time or cut-off frequency. The rise time is the time required for the output signal to change from 10 % to 90 % of the peak output value and is determined by the following factors:

1) *Terminal capacitance C_t and time constant t_1 of load resistance R_L*

Time constant t_1 determined by the terminal capacitance C_t of the photodiode and the load resistance R_L. C_t is the sum of the package capacitance and the photodiode junction capacitance. t_1 is given by

$$t_1 = 2.2 \times C_t \times R_L$$

To shorten t_1, the design must be such that either C_t or R_L is made smaller. C_j is nearly proportional to the active area A and inversely proportional to the second to third root of the depletion layer width d. Since the depletion layer width is proportional to the product of the resistivity r of the substrate material and reverse voltage V_R, the following equation is established as:

$$C_j \propto A \{(V_R + 0.5) \times \rho\}^{-1/2 \text{ to } -1/3}$$

Accordingly, to shorten t_1, a photodiode with a small A and large r should be used with a reverse voltage applied. However, reverse voltage also increases dark current so caution is necessary for use in low-light-level detection.

2) *Diffusion time t_2 of carriers generated outside the depletion layer*

Carriers may generate outside the depletion layer when incident light misses the P-N junction and is absorbed by the surrounding area of the photodiode chip and the substrate section which is below the depletion area. The time t_2 required for these carriers to diffuse may sometimes be greater than several microseconds.

3) *Carrier transit time t_3 in the depletion layer*

The transit speed v_d at which the carriers travel in the depletion layer is expressed using the traveling rate μ and the electric field E developed in the depletion layer, as in $v_d = \mu E$. If the depletion layer width is d and the applied voltage is V_R, the average electric field $E=V_R/d$, and thus t_3 can be approximated as follows:

$$t3 = d / vd = d^2 / (\mu V_R)$$

To achieve a fast response time for t_3, the moving distance of carriers should be short and the reverse voltage larger. The above three factors determine the rise time tr of a photodiode and rise time tr is approximated by the following equation:

$$tr = \sqrt{t1^2 + t2^2 + t3^2} \ .$$

PIN photodiodes and avalanche photodiodes are designed such that fewer carriers are generated outside the depletion layer, Ct is small and the carrier transit time in the depletion layer is short. Therefore, these types are ideally suited for high-speed light detection. The cut-off frequency fc is the frequency at which the photodiode output decreases by 3 dB from the output at 100 kHz when the photodiode receives sine wave-modulated light from a laser diode. The rise time tr roughly approximates this fc in the formula:

$$tr = \frac{0.35}{fc}$$

The problem can be pin pointed by observing the output waveform from the photodetector as shown in the figure 3.10.

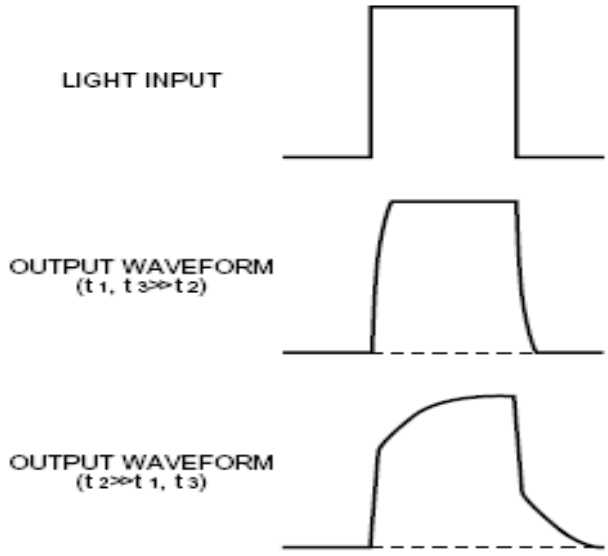

Figure 3.10: Deciphering from photodetctor waveforms [12]

Hence the waveform gives indication about the dominant parameter affecting the frequency response of the photodiode.

3.2.2 Methods for measuring frequency response

Dual modulated method

This method uses light whose intensity is modulated twice [27]. A distinctive feature is that it contains two frequency components that essentially have equal intensities. This technique is independent of the modulation depth of modulators. The measurement principle is shown in the figure 3.11.

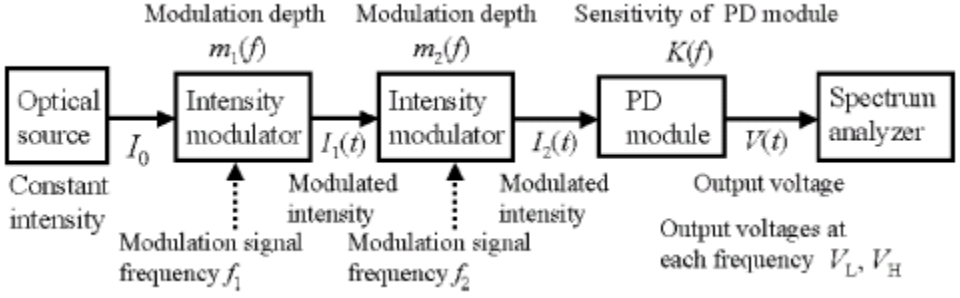

Figure 3.11: Dual modulated method [27]

3.2.3 Readout circuits

The readout circuits are very critical for proper impedance matching between the photodiode and the measurement circuitry. In addition the circuit has to be fast enough to have negligible effect on the measurement. A simple but efficient circuit is shown in the figure below:

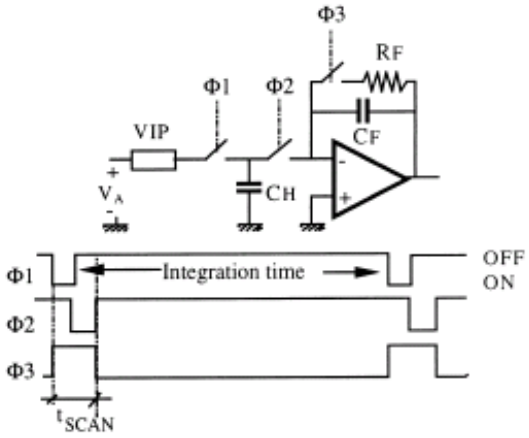

Figure 3.12: Test circuit for charge readout [28]

CHAPTER 4: PLASMA CVD DEPOSITION SYSTEMS

4.1 Introduction

Plasma is defined a distinct state of matter containing a significant number of electrically charged particles, sufficient enough to affect its electrical properties and behavior. An external energy source is required for sustaining the plasma. The most widespread method used is either the DC or radiofrequency (RF) electrical discharge. High electric fields applied at low pressures yield non-equilibrium plasmas, where free electrons are accelerated to 1-10eV, while ions and neutrals have low energy (0.1 eV). These "hot" electrons can initiate chemical reactions through collisions with the "cold" neutrals. This results in processing temperatures much lower than in thermal CVD, which has tremendous consequences for the applicability of PECVD. The density and the energies of the charged particles significantly affect the deposition conditions. Plasma enhanced deposition systems make low temperature deposition possible since part of the energy required for dissociation of reactants is provided by the plasma power rather than only temperature in conventional CVD. The low temperature deposition makes thin film deposition on flexible substrates possible. Different plasma deposition techniques have been studied for better deposition and etching [29]. Types of PECVD deposition systems are listed in the subsequent sections.

4.2 ECR (Electron Cyclotron Resonance) deposition

In the ECR setup there were three tuner stubs for establishing the resonance condition using the microwave power. A microwave generator operating at a frequency of 2·45 GHz is used to produce microwaves, which enter the chamber through the quartz window and it powers the plasma. The quartz window requires regular cleaning due to film deposition on the window resulting in variation of the effective process parameters. Three tuners are provided to tune the resonance condition inside the chamber. Constant magnetic field was maintained using DC supply to the magnetic coils to produce a magnetic field. The cooling water coils keeps a check on heating of the magnetic coils. Any electrons produced by the plasma in this region of magnetic field results in a helical path due to the lorentz force acting on the electrons. This causes the microwaves to be more efficiently absorbed by the

electrons, and the extra energy is dissipated through kinetic collisions with other gas species to increase the ion density of the plasma to be ~1000 times greater than in RF-PECVD. The substrate holder is used for leading the sample and the gasses are fed into the chamber through two different manifolds. Constant pressure was maintained during the deposition by maintaining a balance between pumping rate and the flow rate using the control gate valve.

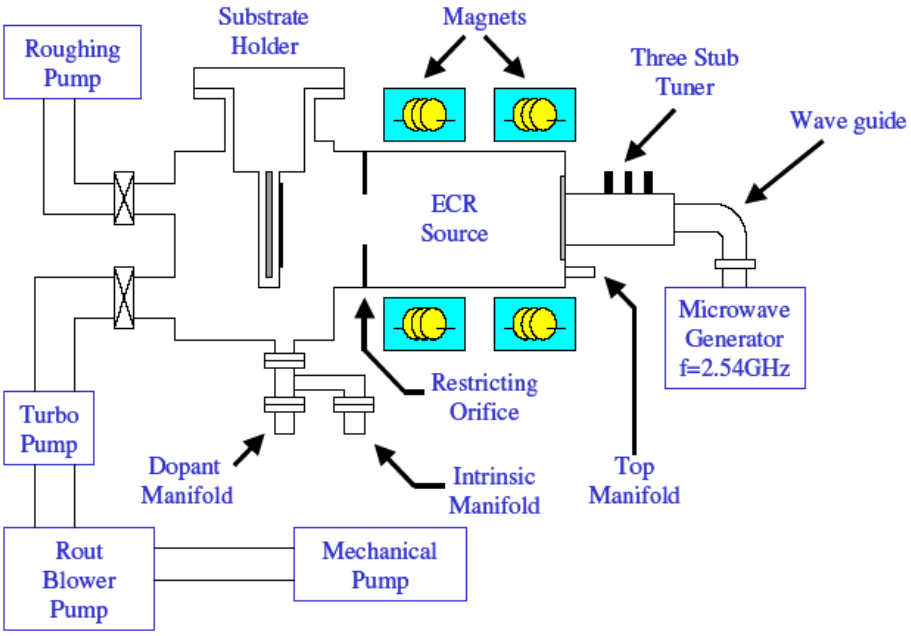

Figure 4.1: Schematic of ECR Plasma Reactor [30]

Advantages

- High ion densities in the plasma
- Low ion energies reducing the ion bombardment
- Ion density and ion energies can be controlled independently
- Better deposited film quality

Disadvantages

- Low deposition rate
- Non uniformity of the plasma and as well as the deposited film over larger area
- Regular cleaning required for the quartz window

4.3 VHF PECVD

The VHF stand for very high frequency and typically the frequency is in MHz range. The deposition method utilizes the interaction of the gas molecules with the supplied field resulting in plasma formation. The frequency determines the ion density and the ion energies and hence amount of ion bombardment, determining the quality of the deposited film. The device growth has been done using RF frequency of 13.5 MHz until in 1987, Neuchetal, introduced a new method of 'VHF' plasma enhanced CVD method [31]. This method is characterized by higher deposition rates, which increases with increasing frequencies as shown by other groups [32, 36, 33].

The VHF grown a-Si has been studied extensively due to their good adhesion properties in the films compared to other techniques along with higher deposition rate. The frequency response can be correlated to the defect density in the intrinsic layer for a p-i-n photodetector. The effect of VHF frequency and the deposition temperature has been well studied as shown in the figure below [34]:

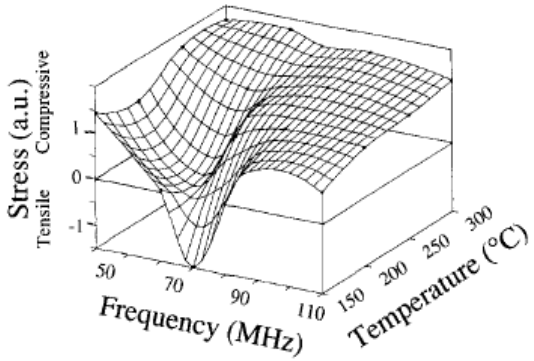

Figure 4.2 (a): Stress as a function of plasma excitation frequency and deposition temperature.

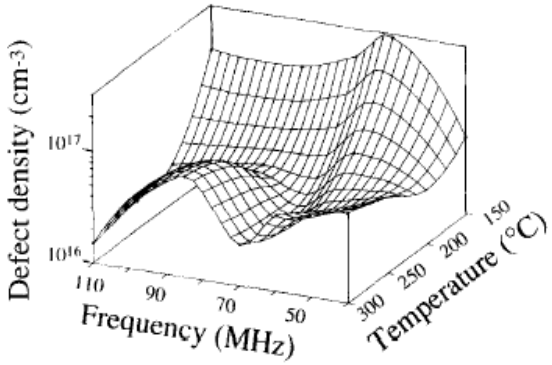

Figure 4.2 (b) Defect densities as a function of plasma excitation frequency and deposition temperature.

The VHF plasma has following significant characteristics

a) At constant plasma power, the sheath potential (which governs the maximum ion energy at lower frequencies) decreases at higher excitation frequencies and gives rise to reduced stress in the layers.

b) As the sheath thickness decreases at higher plasma excitation frequencies, but the mean free path of the energetic ions that impinge on the substrate is constant at constant pressure, less thermalisation of maximum ion energy due to ion neutral collisions occurs. As at excitation frequencies above 60 MHz only a slow further decrease of the sheath potential can be observed, this lack of thermalisation could explain the increase in the peak ion energy [35], which was confirmed experimentally from ion energy measurements at constant plasma power by Howling [36].

c) At excitation frequencies above 60 MHz, the sheath potential is more due to the plasma potential and less due to the peak-to-peak voltage. The plasma impedance decreases at higher excitation frequencies, increasing the total discharge current at constant plasma power resulting in higher bulk electron density.

Using higher frequency gives better film quality due to lower ion bombardment on the growing surface. The thinner plasma sheaths at higher frequencies results in a lower sheath potential and hence correspondingly ion bombardment on the growing layer is reduced. The power coupling efficiency improves resulting in higher electron densities and hence better silane dissociation at moderate sheath voltages as shown in figure 4.3 [37].

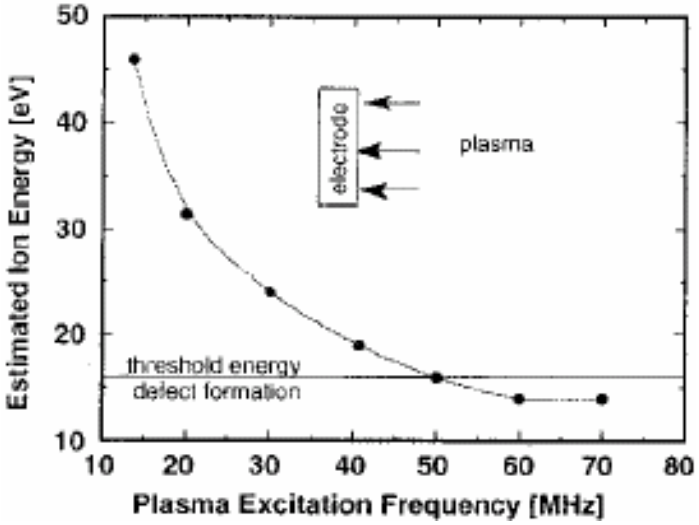

Figure 4.3: Dependence of ion energy with excitation frequency

The VHF plasma can be divided into two major subcategories:

1. *ICP (inductively coupled plasma)*

An ICP source comprises a single-turn inductively-coupled RF (13.56 MHz) discharge with a superimposed static transverse magnetic field. During operation, the application of a magnetic field results in the formation of an electrically anisotropic plasma.

At resonance there is a strong absorption of energy by the electrons in the plasma as the rotation of the electric field vector of the right-hand polarised wave coincides with the gyration direction of the plasma electrons. Hence the plasma is heated very efficiently. Combined with a reduction in electron losses to the walls through electron cyclotron motion around the magnetic field lines, this resonant energy transfer enables high plasma densities to be achieved even for excitation frequencies of 13.56 MHz (n_e ~ 10^{10} to 10^{13} compared with 10^8 to 10^9 for conventional RF based plasma processing discharges). Consequently, highly ionised plasmas may be produced at both low operating powers and pressures. Due to its high plasma densities, nowadays it has been extensively used for the etching system with better controllability over the etching species.

The coupling in ICP plasma is not purely inductive, but has a capacitive component as well through the wall of the reactor. A schematic of the ICP plasma is shown in the figure 4.4.

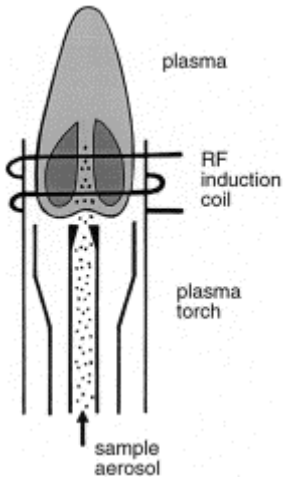

Figure 4.4: A schematic of ICP plasma [29]

2. Capacitively coupled plasma

The capacitively coupled plasma is characterized by two parallel plates with one powered electrode and other grounded. The plasma is generated within the plates and their ion densities and the energies can be controlled by varying the RF power, chamber pressure and by changing the deposition frequency. The schematic of a capacitively coupled system is shown in the figure below:

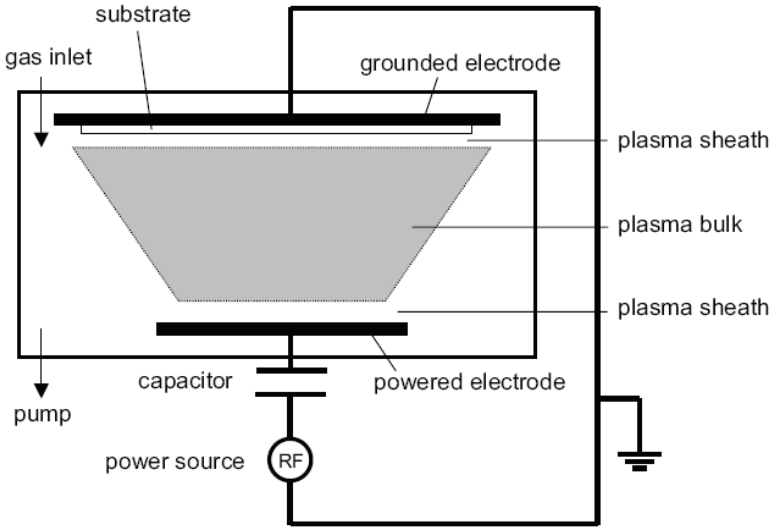

Figure 4.5: Capacitively coupled VHF plasma

The plate area is also varied in the chamber to develop a DC voltage variation and hence assisting the ion movement. The plasma typically form a sheath region near the electrodes and this voltage varies by the equation given below:

$$\frac{V_1}{V_2} = \left(\frac{A_2}{A_1} \right)^m \tag{4.1}$$

The schematic for the capacitively coupled reactor is shown in figure 4.5.

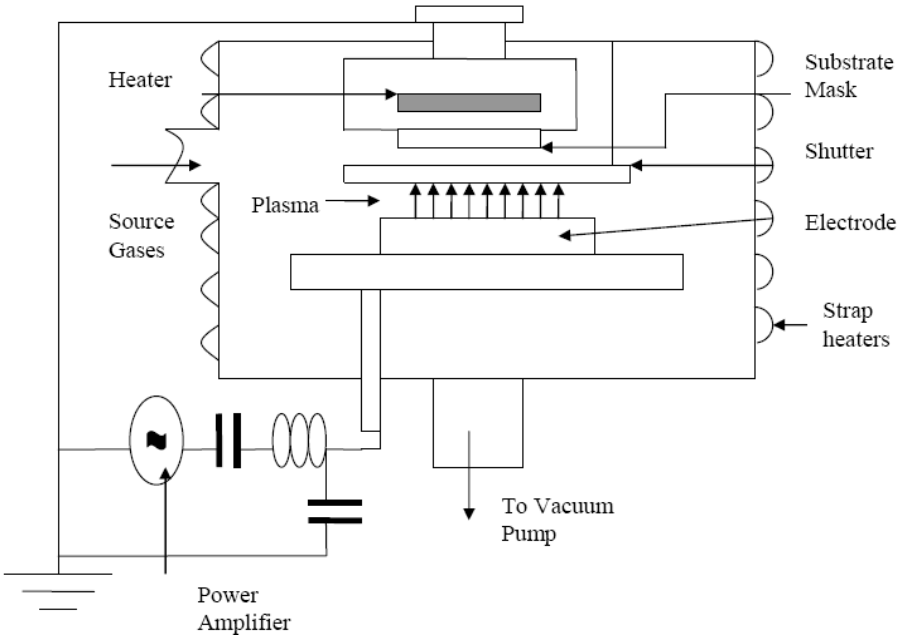

Figure 4.6: VHF Plasma Reactor [38]

The electrode size variation results in variation of the plasma sheath voltage and hence the plasma potential. On the larger electrode, the potential is smaller resulting in lower bombardment. Typically in the PECVD condition n=2. It also results in unequal plasma potential and negative potential in the deposition side of the plasma sheath. This results in very low electron concentration in the sheath due to repulsion and mostly consists of ions. This reduced the high energy electron and makes ion deposition possible.

The electron density in the plasma is proportional to the plasma frequency. For higher frequency we obtain a higher density. The electron plasma frequency is given by the equation 4.2.

$$f_{pe} = 9000\sqrt{n_e}\ (\text{Hz}) \tag{4.2}$$

When the excitation frequency is below the plasma frequency, the electrons are able to respond and hence generate the plasma. The plasma sheaths change with frequency.

CHAPTER 5: MATERIALS FOR FABRICATION OF DEVICES

5.1 Introduction

The electronic materials required for the fabrication of the photodiodes should have some characteristic properties. Though the materials doesn't required to be a direct bandgap material as for luminescent devices like leds and lasers, but they must have very low defect densities to have an efficient and fast response. The defect centers acts as the recombination centers which reduce the efficiency. In addition to the defect centers respond at lower frequencies.

5.2 Amorphous Silicon

Amorphous silicon has hydrogen in between the dangling silicon bonds resulting in more passivated dangling bonds. Since Si-H bond energies are higher due to lower bond length compared to Si-Si bond, the effective bandgap of the amorphous silicon is higher around 1.8 eV. Also the material in direct bandgap with a much higher absorption coefficient requiring a much lower film thickness requirement compared to crystalline silicon. The bandgap can be varied a bit by addition additional hydrogen. The growth mechanism has been studied by Robertson et.al [39]. The mechanism is depicted in the schematic below.

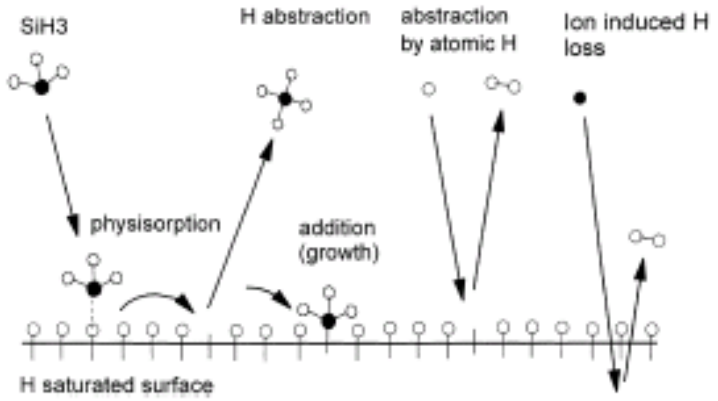

Figure 5.1: A schematic for the model of plasma film deposition.

But the materials have many defects resulting in midgap states within the bandgap of the material as shown in the figure 5.2.

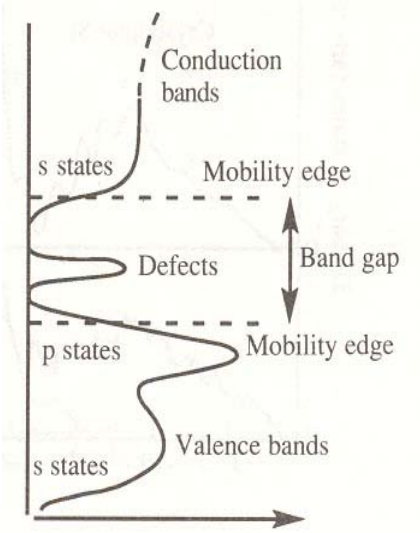

Figure 5.2: Density of states of amorphous silicon

Collection efficiency of the devices is also dependent on the thickness of the intrinsic layer. The efficiency decreases with increase of thickness above 0.5 microns as shown in the figure 5.3.

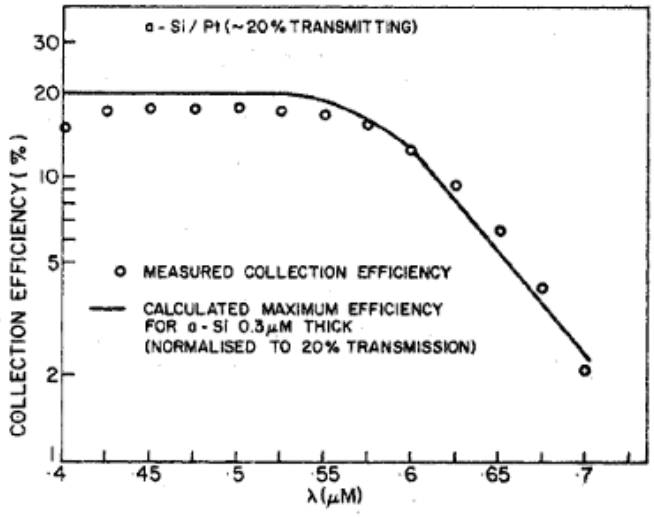

Figure 5.3: Dependence of collection efficiency on device thickness [40]

The efficiency also depends on the doping of the intrinsic layer. The doping of the intrinsic layer near the p layer is more deleterious and results in reduced current in the I-V

plots. Especially in the superstrate structures, where the p layer is grown first, there can be tremendous in grown boron diffusion resulting in the doping of the intrinsic layer.

5.3 Amorphous SiGe

This material has received some attention due to the bandgap engineering to achieve better device performance. Depending on the Ge content the bandgap can be varied and graded along the thickness of the device. But unfortunately Ge also introduces defects in the materials deteriorating the device properties. It has been observed that with higher Ge content the material becomes poorer. The materials properties have been studied in detail [41]. It has been observed that the bandgap varies linearly with the Ge content as shown in the figure 5.4.

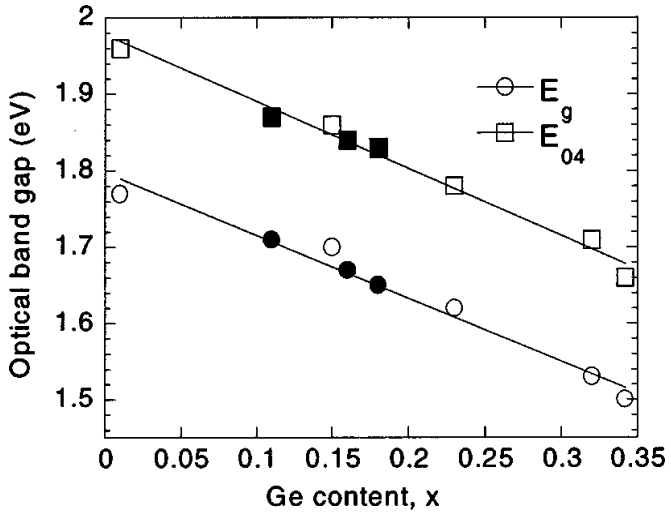

Figure 5.4: Variation of bandgap with Ge content (x) [42]

The bandgap can be modeled with x by linear regression fit of the above mentioned data. For amorphous silicon bandgap is 1.8 eV and hence is linearly reduces as given by the equation below:

$$\text{Bandgap} = 1.8 - 0.82\,x \tag{5.1}$$

The conduction and the valance band both vary linearly with the Ge content and hence the bandgap grading is gradual.

5.4 Nanocrystalline silicon

Nanocrystalline silicon has received recent attention due to the higher mobility compared to amorphous devices resulting in the faster device response especially useful for fast photodiode applications. Due to its lower bandgap it has higher absorption coefficient at higher wavelengths. Nanocrystalline silicon is characterized by crystallites within an amorphous matrix. Starting from the single crystal silicon in silicon wafer, we move to polycrystalline silicon with typical grain sizes of 100 nm compared to about 10 nm for nanocrystalline silicon as shown in the figure 5.5.

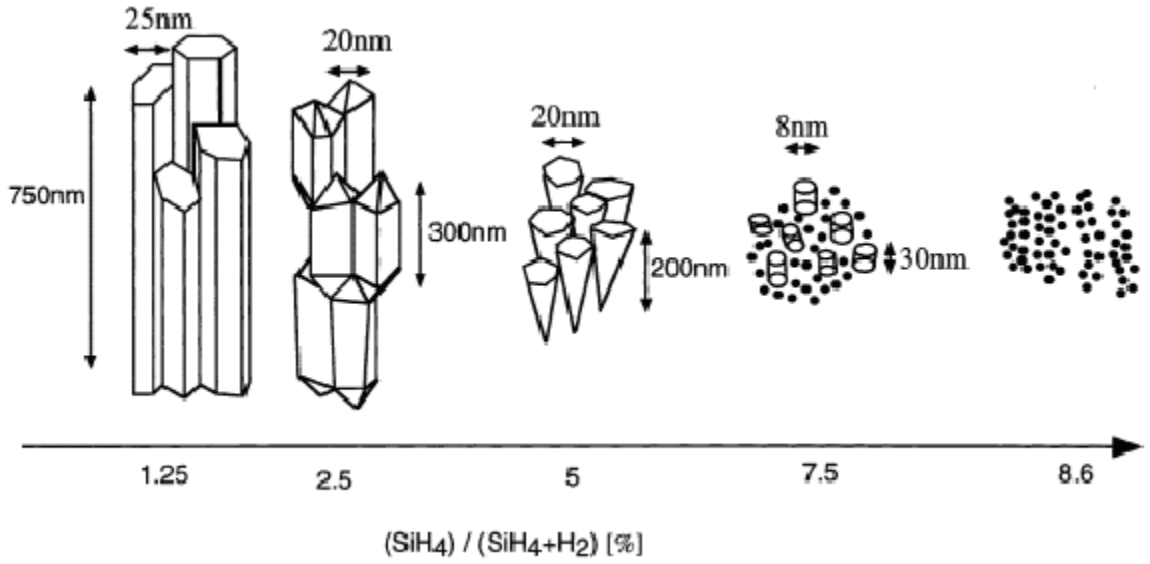

Figure 5.5: Variation of grain size with hydrogen dilution [43]

With smaller gain sizes, the grain boundary effects become much more prominent resulting in different characteristics compared to crystalline silicon.

Defect reduction has been reported on using hydrogen on annealing and during the growth of amorphous silicon films using plasma CVD techniques. Higher hydrogen dilutions results in transition to nanocrystalline films due to more ordered structure formation in presence of hydrogen [44]. Two models: surface diffusion and selective models have been proposed to understand the growth mechanism. In the surface diffusion model, high H flux impinging on the surface is attributed to enhance the mobility of the deposition precursors. In

the selective etching model, amorphous and crystalline phases are assumed to be deposited simultaneously, but H selectively etches the amorphous material leaving behind a nc-Si:H film. The chemical reactions and transport phenomena observed include [44]: (1) H adsorption onto the surface; (2) surface H abstraction by the impinging H atoms; (3) insertion of H into strained Si–Si bonds; (4) H diffusion into the bulk substrate/film; (5) sputtering of surface H atoms.

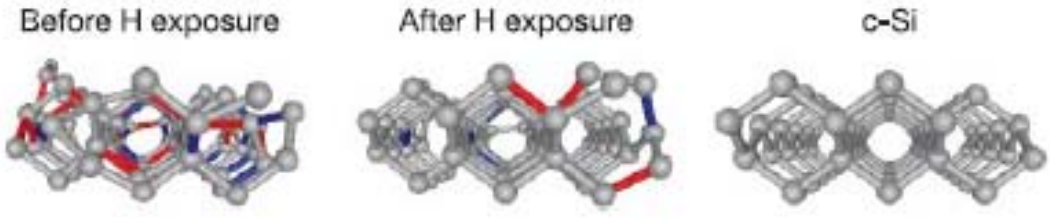

Figure 5.6: Effect of hydrogen plasma treatment on nanocrystalline growth

The growth of nanocrystalline silicon doesn't starts instantly. Instead it forms an initial amorphous layer and then seeds start to form in the incubation layers. The incubation layer needs high hydrogen dilution for initial seed formation. Hence the structure formed in conical around the seed layers as reported by Collins et. al [45].

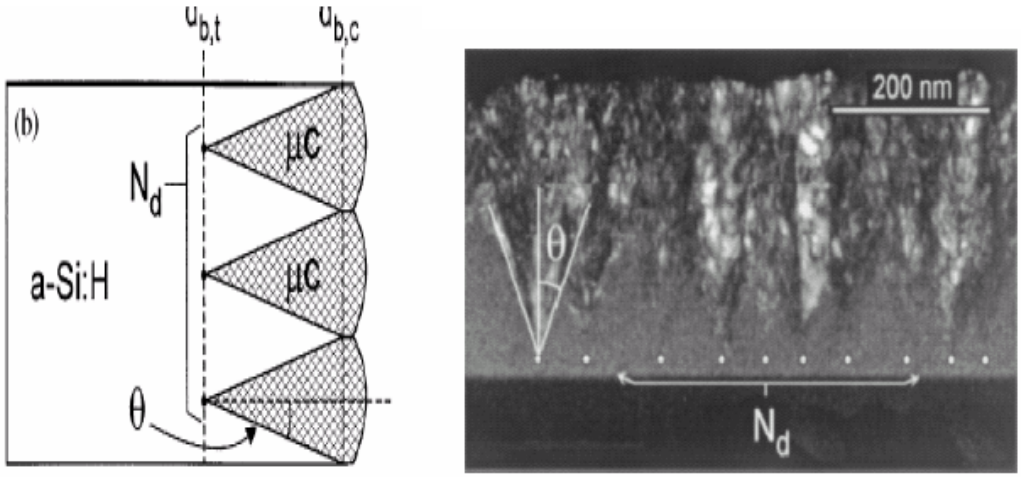

Figure 5.7: Seed formation and nanocrystalline growth

The nanocrystalline growth is higher in higher hydrogen dilution. But the growth rate also reduces at higher hydrogen dilution facilitating better nanocrystalline materials. The dependence in hydrogen dilution is studied by Collins [45].

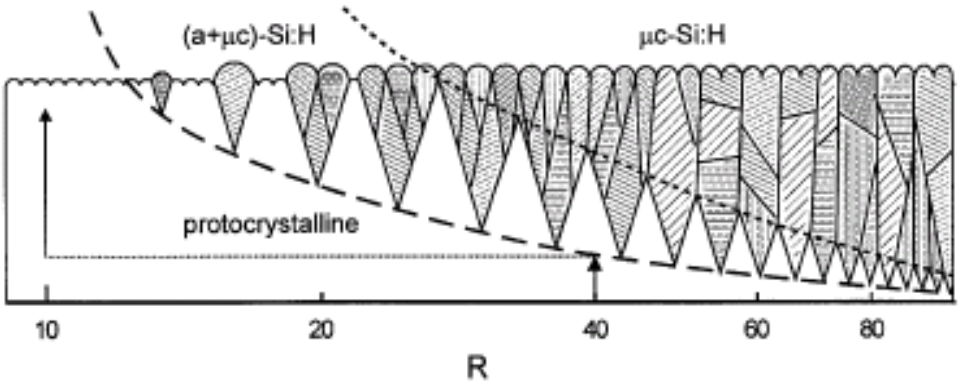

Figure 5.8: Nanocrystalline growth at different dilution R =$[H_2]/[SiH_4]$

For deposition of doped p layers needs to be done at much higher dilutions with R~150. This extremely high dilution in the p layer is required for two reasons: (1) dopant makes the nucleation more difficult requiring higher dilution; (2) p layer is very thin and hence the nucleation should start early in minimum incubation layer thickness.

The powder formation in the plasma is also very important and mainly occurs due to formation of higher order radicals especially at higher deposition pressures. Its formation has been also attributed due to instability in the plasma [46]. Surprisingly low defect density films are obtained in this powder formation regime resulting in a polymorphous material. The formation mechanism is shown in figure 5.9.

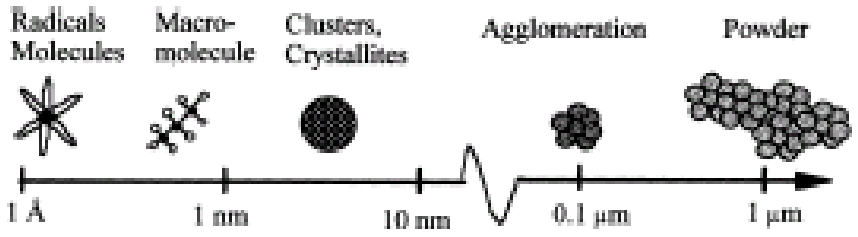

Figure 5.9: Schematic representation genesis of powder formation [47]

CHAPTER 6 CHARACTERIZATION TECHNIQUES

6.1 Thickness measurement

6.1.1 Optical Measurements

The thickness of the devices and the films were measured using a Lambda 9 UV/NIS/NIR spectrophotometer. This is a dual beam apparatus, where one of the monochromatic beams travels unobstructed, while the second beam is made to incident on the sample as shown in the figure 6.1.

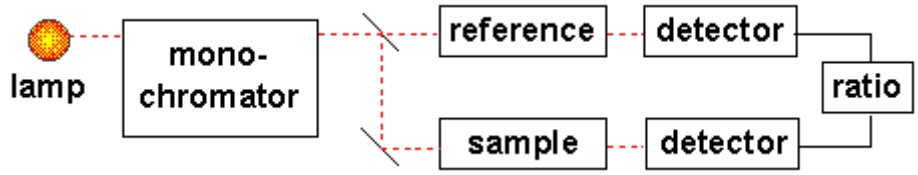

Figure 6.1: Dual beam spectrometer

A mirror assembly was used for creating an interference pattern due to the reflection from the top and bottom surfaces of the sample. Both the monochromatic beams are finally collected by a detector and their intensities were compared to the original beam. A typical interference pattern is shown in the figure 6.2.

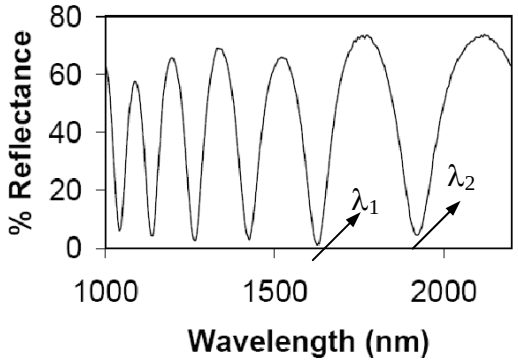

Figure 6.2: Interference spectra in reflectance measurement

The variation of the refractive index is also considered for the measurements and is especially important if we are doing the measurement at lower wavelengths, where the variation of refractive index is sharper. The thickness is calculated from the equation 3.1

$$t = \frac{\lambda_1 * \lambda_2}{2*(n_1\lambda_2 - n_2\lambda_1)}$$

Where n_1 and n_2 are the refractive indices at the wavelengths λ_1 and λ_2

6.1.2 Electrical Measurements

The electrical thickness measurements were done using capacitance voltage technique. Very simple method was used for the measurement. Most of the devices used were p-i-n devices. Reverse voltage was applied on the devices assuring that the whole intrinsic layer is depleted. This was verified by assuring that the capacitance almost saturates and does vary much with increasing voltage. At this moment the absolute value of the capacitance is an indicator of the intrinsic layer thickness. The thickness was estimated by the equation given below:

Thickness = (Area * dielectric constant) / Capacitance (6.2)

For the measurement frequency used was 100 KHz where the defects states shouldn't respond and interfere with the measurements. The dielectric constant variation may be a critical parameter affecting the accuracy of the measurements.

6.2 Electrical characterization

6.2.1 I-V Characteristics

The current voltage characteristic is the first characterization of any device. It estimates the device performance and indicates the possible problems in the device. Most common is the bandgap or interface mismatches, which is show up as kink in the I-V curve. Apart from that the open circuit voltage indicates the bandgap of the material if the doping and the composition of the doped layers are kept constant. It's an indictor of the built-in field of the device. This is especially useful for an idea about the crystallinity in the nanocrystalline devices. The short circuit current is an indicator of sensitivity and the series and shunt resistant indicates the device quality.

The photodiode works especially in the third quadrant, where a negative voltage is applied.

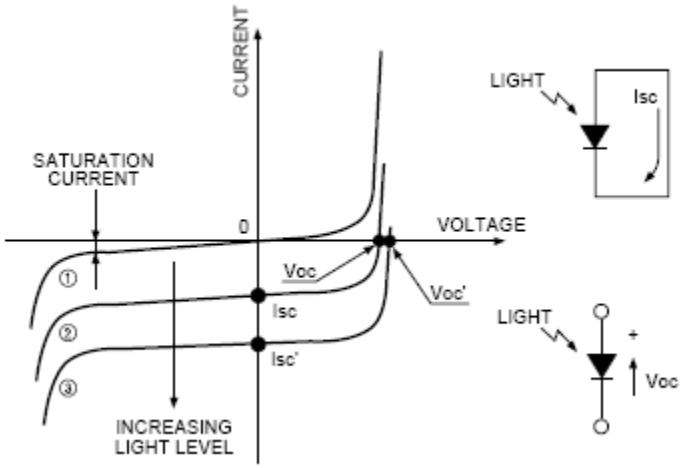

Figure 6.3: Photodiode under dark and illuminated conditions [12]

Generally for photodiode, there is a voltage dependence on the current. It's beneficial for the photodiode since we can put a reverse bias unlike the solar cells. Also putting forward bias reduces the capacitance and makes the photodiode respond faster. But we have to pay the price in the dark current. The dark current goes up as seen by the slope of the I-V curve in reverse bias, which in turn increases the noise and hence reduces the sensitivity. So for best operation an optimum voltage level should be chosen.

6.2.2 Quantum efficiency

The quantum efficiency of the devices is defined as the number of electron hole pairs produced with one photon. This is known as the internal quantum efficiency. But for actual measurements we measure external quantum efficiency, which is also affected by the collection efficiency of the device. The QE is given by the Equation 6.3.

$$QE = \frac{\eta * electronholepairs}{\#ofphotons} \tag{6.3}$$

Where η is collection efficiency of the device

A schematic of the Absolute QE measurement setup is shown in the figure 6.4. For absolute QE the signal from the photodiode is compared with the standard crystalline silicon photodiode.

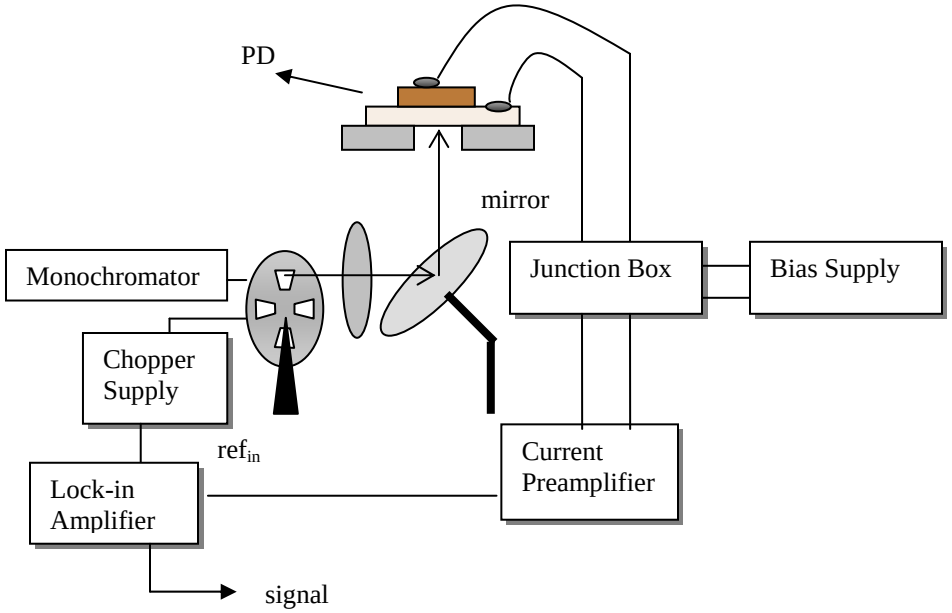

Figure 6.4: Schematic for Quantum Efficiency setup

A typical QE spectrum for a-Si is shown in the figure 6.5. We see maxima in the collection efficiency. The penetration depths also vary with the wavelength of light. The higher wavelengths penetrate deeper into the device and hence results

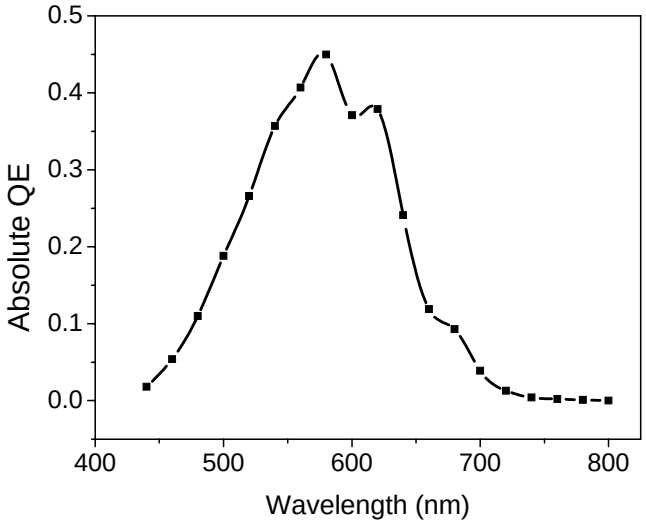

Figure 6.5: Sample QE of a-Si photodiode

The QE of the device are calculated by following methods. First the active area of the device as well as that of the standard silicon cell is determined. The amplification of the current amplified needed to be increased due to lower device area compared to the standard cell.

$$QE = \frac{SampleSignal}{\#\,ofincidentphotons} \tag{6.4}$$

$$QE = \frac{S_{Sample} * G_{sample}}{\frac{A_{sample}}{A_{cell}} * \frac{S_{cell} * G_{cell}}{QE_{cell}}} \tag{6.5}$$

The area of the standard cell is $1cm^2$ and the gain in the current amplifier used for the cell was 10^5 V/A. The gain for the sample varied from 10^6 – 10^7 depending upon the sensitivity. Hence the equation 6.5 reduces to equation 6.6

$$QE = \frac{S_{Sample} * G_{sample} * QE_{cell}}{A_{sample} * S_{cell} * G_{cell}} \tag{6.6}$$

The chopper frequency used was 13.5Hz and the samples were measured from 400 to 800 or 900nm depending on whether they were amorphous or nanocrystalline samples. To prevent the lower order harmonics to interfere during the measurements, a filter with cutoff below 700nm was used above 700nm. The device was tested both under bias and as well as unbiased conditions.

6.2.3 Capacitance Voltage measurements

The CV measurements are very informative especially for the estimation of the defect density of the device. The doping density or the shallow defect density and the deep defect density in the devices were evaluated from the CV data based on Kimerling's model [48]. The model predicted that under reverse bias and at lower frequencies, the capacitance voltage curve shows two distinct regions as shown in Figure 6.6. In the first region where the capacitance increases sharply with the reverse bias, the slope corresponds to the donor density or the shallow state defect density whereas the slope of the second region is used to evaluate the deep defect density. The low frequency assures enough time for the deep state carriers to respond to the applied bias.

The defect density is calculated by following method as shown in figure 6.6.

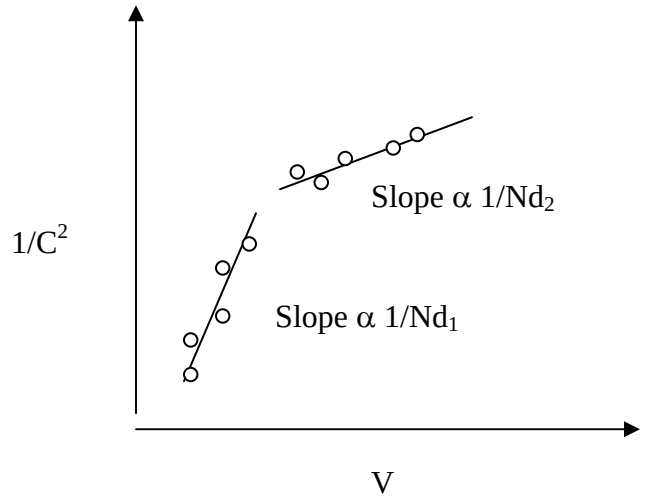

Figure 6.6: Kimberling method of defect density estimation

The defect density is calculated by subtracting Nd_1 from Nd_2. We observe that Nd_2 is larger since the slope is smaller. Nd_1 corresponds to the doping level density and corresponds to shallow defect states. The measurement was done at a frequency of 120Hz with a drive AC voltage of 100mV.

6.2.4 Frequency response

The frequency response measurement is critical for determining the response speed of the photodiode. The setup consists of inorganic LED pulsed using a pulse generator at varying frequencies. First the LED is calibrated using a fast response commercial silicon photodiode by Hamamatsu. This step was for verifying if the intensity of the LED changed with the pulsing frequency. It was observed that the capacitance of the photodiode was very critical for fast response. The measurement was done using lock-in detection to minimize the noise and fast response SR570 current amplifier was used for the measurement. If too high gain is used, it affects the response speed. Hence gain should be chosen so that the response speed becomes independent of the gain. Typically a gain of 10^4 was used for the device measurements. The current amplifier was used in high bandwidth mode to have fastest possible response, but it was achieved with increased noise in the system. Both the signal intensity and the phase were measured with respect to the input reference frequency and the cut-off frequency was defined as the frequency when the output signal went out of phase i.e. a phase difference of 90 degrees.

6.3 Crystallinity measurements

6.3.1 X-ray Diffraction

The fundamental principle for the X-Ray diffraction is the Bragg's law which is given by the following equation:

$$2d \sin\theta = n \lambda \tag{6.7}$$

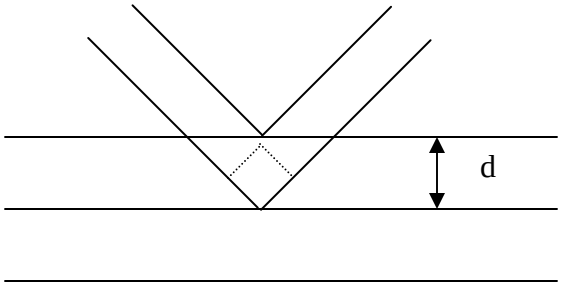

Figure 6.7: Interference from crystals planes in XRD

The path difference becomes 2d Sinθ and when it equals to the optical path n λ, we start to observe constructive interference and hence a peak in the XRD spectra as shown in the figure 6.8.

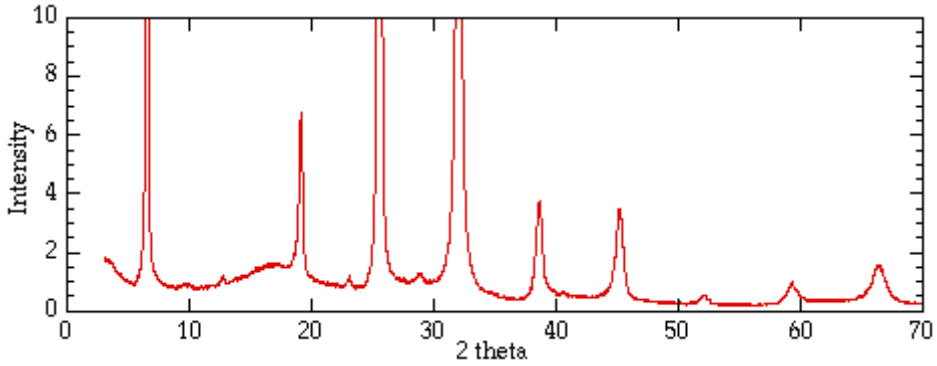

Figure 6.8: A typical XRD spectra

The different peaks correspond to the different crystal planes. The miller indices used are <hkl> in the crystal and they are related by the equation shown below:

$$d = \frac{a}{\sqrt{h^2 + k^2 + l^2}} \tag{6.7}$$

The most important planes to observe for the devices are (111) and (220) planes in the films. As we can understand that (220) will have lower d values and hence they occur at a higher 2θ values. For (111) it occurs at 28.5 degrees compared to 47 for (220). Another important information obtained in the grain size. This is computer by the Sherrer's Formula [49] as given by the equation 6.8.

$$S = \frac{0.9\lambda}{\beta \cos\theta} \tag{6.8}$$

where S is the grain size, λ is the wavelength of the X-rays, θ is the angle of incidence for the X-ray beam and β is the Full Width Half Maximum (FWHM) of the individual crystalline peaks. Hence in short the broader peaks correspond to lower grain sizes.

6.3.2 Raman Spectroscopy

The Raman spectroscopy utilizes the elastic and the inelastic scattering to characterize the material. The technique was first developed by Dr C. V. Raman and used now days for variety of material characterizations. A majority of the photons are scattered elastically resulting in same wavelength for incident and the scattered photons and this phenomenon is called Raleigh scattering. The second type involving inelastic scattering also known as the Raman scattering has a significant shift in wavelength between the incident and scattered photons. In in-elastic scattering, photons either create phonons referred as stokes or they annihilate the phonons also known as anti-stokes. These phonons vibrate in the lattice with a certain frequency, which is a characteristic of each individual material and accordingly a sharp peak is obtained in the final spectra at a wavelength corresponding to the vibrating frequencies of the phonons as shown in figure 6.9.

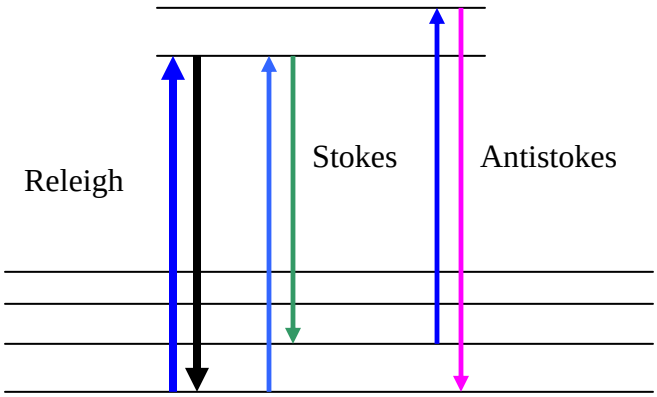

Figure 6.9: Stokes and antistokes shift in the raman scattering

For the measurement, the Raman shift was estimated and plotted. Reflex Raman Microscope by Renishaw was used for the measurements, where in a laser beam is incident on the samples and the scattered photons being collected by a CCD. During the measurement the laser intensity has to be low to assure that there is no laser induced crystallization during the measurement resulting in wrong interpretation. A typical Raman spectrum for nanocrystalline silicon is shown in the figure 6.10.

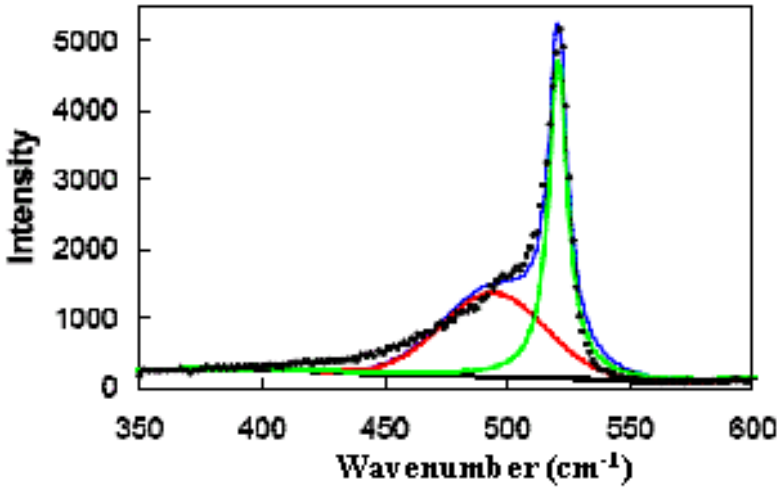

Figure 6.10: Raman spectra from nanocrystalline silicon

The Raman spectra above are a superimposition of two peaks, which can be deconvoluted into a Gaussian (amorphous tissue) and a Lorentzian (crystalline tissue) peak. Hence the ratio between peak heights indicates crystallinity and FWHM gives grain size.

CHAPTER 7 SENSOR DESIGN AND FABRICATION

7.1 Sensor design

The sensor was designed by integration of three components: OLED, oxygen sensitive sensor dye film and the thin film based photodiode. First the viability of the sensor was tested in a front detection mode utilizing the photoluminescence intensity quenching property of oxygen. The front detection mode is easy to integrate but requires a bandpass and a longpass filter for measurement. The back detection mode is where actual integrated sensor can be developed with both OLED and the photodiode on same side of the substrate resulting in encapsulation being possible and hence a better and higher integrated device lifetime. A schematic comparison is shown in the figure 7.1.

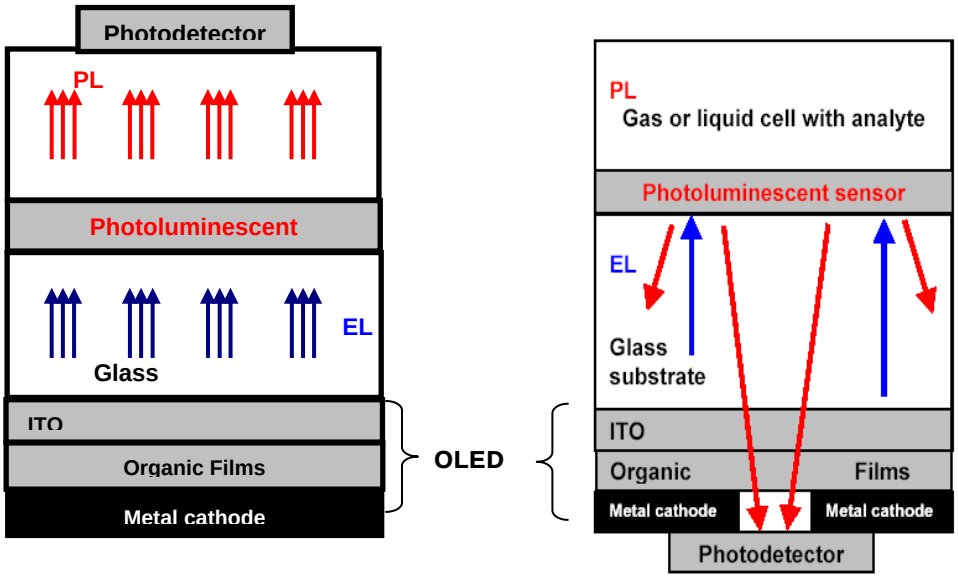

Front detection mode Back detection mode

Figure 7.1: Schematic comparison of front and back detection sensor design

Back detection mode has many challenges too including background light being detected by the photodiode due to its proximity to OLED. This necessitates the use of lifetime mode of detection with pulsed OLED so that measurement can be done only when OLED is off since there is no provision of putting any filter. This requires development of fast response photodiodes.

7.2 Integration of the components and challenges

The final three-component integration was done using the design given in Figure 7.2. The integrated structure was developed on a single substrate with the device thickness dominantly determined with the substrate glass thickness. The overall thickness was around 3mm resulting in a miniaturized and compact sensor.

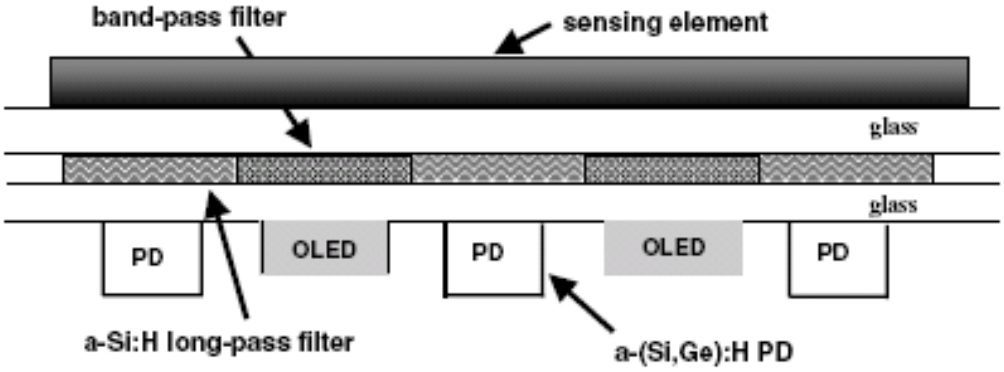

Figure 7.2: Design of the developed structurally integrated sensor [50]

There were many challenges like edge emission from the OLED and the electromagnetic noise being generated by OLED. The edge emission was blocked using aluminum film grown between the PD and the OLED, which acted as a light-blocking layer. Also there was some waveguiding effect through the glass substrate, which needs to be blocked by some mechanism, and it will be part of the future work.

7.3 Fabrication process flow

The fabrication was started using 2 x 2 inch substrate of ITO coated glass. First the ITO side is determined by using a multimeter. Then the substrates in scribed on the glass side using a diamond cutter. The best at write asymmetric letters like R for better visibility during processing. This glass was then precleaned in methanol. The substrate was then ultrasonically cleaned in methanol for 5 min. The substrate shouldn’t be cleaned too well otherwise it was observed to affect the sticking capability of the photoresist during the subsequent lithography steps.

7.3.1 Lithography of ITO

The process steps are given in sequential manner below:

1. Turn on the both the ovens in the lab to ramp up to 90 and 120 degrees respectively
2. Spin-coat the adhesion enhancer HDMS on top of the substrate with ITO side on the top.
3. Next spin coat photoresist AZ 5214 so that the resist is about a micron thick.
4. The photoresist is prebaked in oven at 90 degrees for 15min
5. Next it is irradiated with UV using a metal mask in Karl-Sus mask aligner. Since we desire ITO to stay in the region, which are getting illuminated, we need to use the photoresist as negative resist. The exposure was done for 1.5 min.
6. The sample was then put in the oven at 125 degrees for 5 min to facilitate the crosslinking to occur providing the negative resist property. This step in very critical.
7. Next the sample is put for a flood exposure of UV without any mask for 2.5 min. This step softens the earlier unexposed regions and this region gets dissolved in the developer in the next step.
8. The sample is developed next in the developer solution with photoresist only on top of the regions where we desire ITO to be present after patterning. The development is done in about 1 min and clear fringe patterns will be visible.
9. Next the sample is rinsed in DI water and then dried properly. Then it is put into the oven at 120C for post baking for about 10 min. Too long post baking results in difficulty of the photoresist removal after etching.
10. Next a 30% by volume solution of HCl is prepared for etching. I ideally the solution should be heated to around 50 degrees to achieve fast etching. It takes about 3min to etch the ITO. Golden color patterns will be visible at the edges when the etching in done. The sample should be rinsed in DI water and then tried with subsequent testing of conductivity with multimeter to assure complete ITO removal.

11. If things were ok, then the photoresist needs to be stripped and it can be done by first rinsing in acetone followed by rinsing in methanol. In some cases it might be required to ultrasonically clean the sample in methanol to remove the photoresist.

7.3.2 ZnO deposition

The ZnO deposition was done using RF sputtering. Both undoped and Al doped ZnO was used for the devices. It was observed that Al doped ZnO gave better performance due to higher conductivity. The deposition was done at 40W power in 10mT pressure with Ar plasma at 150 degrees. The chamber pressure before starting the run was kept around 1 x 10^{-6} torr. The Ar flow used was 40sccm. Deposition mask was used to deposit ZnO on top of the center ITO. This ZnO layer was the protective layer for the ITO under hydrogen plasma.

7.3.4 Device layer deposition

The device layer deposition was done using PECVD technique. First the p layer was grown using diborane and silane. Appropriate hydrogen dilution was used to optimize the process parameters. The deposition temperature used was 225 degrees. Next a dummy layer was done with shutter closed to minimize the memory effects due to the last deposited dopant layers. Then the intrinsic layer was grown and appropriate TMB grading was done to engineer a built-in filed in the device resulting in an enhanced carrier collection. The intrinsic layers were grown at 250 degrees. Next the n+ layer is grown using phosphine as the dopant gas. This layer was also deposited at 250 degrees. The sample is then cooled in silane and hydrogen environment before taking it out from the reactor.

7.3.5 Metallization

Aluminum was grown on top the n+ layer and the metal contact. It was deposited using thermal evaporation at a pressure of 1x 10^{-6} torr. The al was deposited at a rate of 25A/s with a total thickness of 2500A. The layer was intentionally grown thick to elongate the device life considering the constant scratching on the surface by the testing probes.

7.3.6 OLED deposition

First the ITO strips for the OLED are put under oxygen plasma treatment for increasing the work function of the ITO to achieve better injection in OLED and hence its

better performance. The OLED materials Alq_3 is deposited by thermal evaporation in a glovebox. Next the metal layers of aluminum are put of the top as other contact for OLED. The process needs to be done under low oxygen environment to have lower OLED device degradation during operation.

7.3.7 Encapsulation

The encapsulation is the very critical step determining the lifetime of the sensor during operation. Special care needs to be taken to have minimum possible oxygen and water vapors, which are the major contributors for degradation and failures. The encapsulation is done using another glass substrate at the back glued using an epoxy resulting in an airtight encapsulation. The whole process in accomplished inside a glove box to assure minimum possible oxygen incorporation in the material.

After encapsulation the final device is taken outside the glove box and testing wires are put on top the metal interconnects using indium. Now the whole device structure is ready for measurements.

The sensor dye film is prepared using polymers PtOEP and PdOEP are dissolved in polystyrene solution. The films are deposited using drop cast technique. The films are dried and they are ready for measurements.

The whole processing step is shown pictorially in the figure in the next page for simplified understanding.

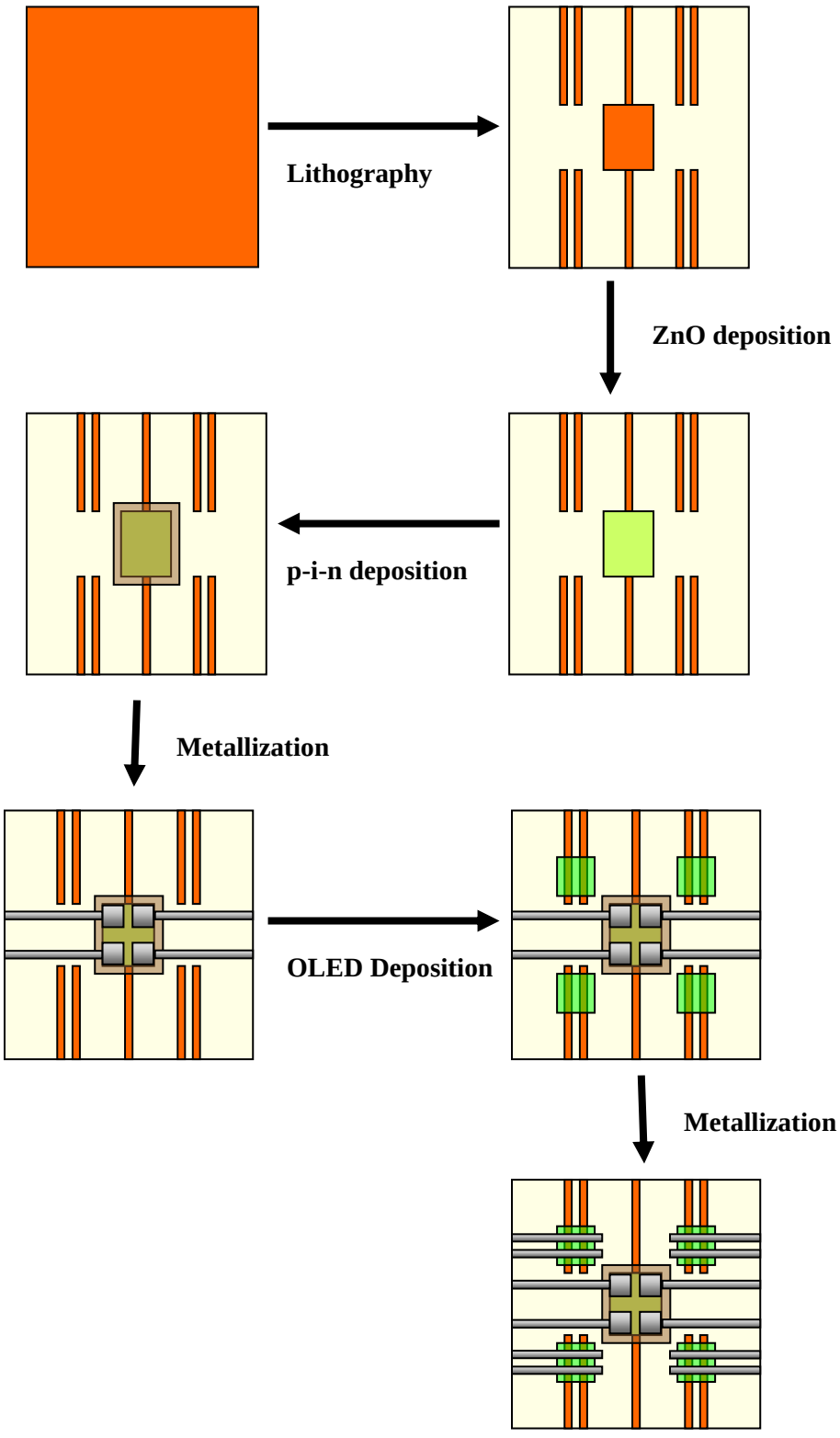

Figure 7.3: Schematic showing the fabrication process flow

CHAPTER 8 RESULTS AND DISCUSSIONS

8.1 Sensor design

The objective of this project was to fabricate a structurally integrated oxygen sensors using OLED as an excitation source, poryphyrin based oxygen sensitive dye film and PECVD grown thin film photodetctor as detection component. The idea was to monitor the photoluminescence from the sensor dye films PtOEp and PdOEp, which in turn is dependent on the oxygen concentration around its ambient, resulting in oxygen sensing capabilities. The novel idea about this work is the use of OLED excitation source instead of conventional laser sources, which make the systems very bulky. In this study, we will discuss the results of the integrated devices and the procedure used for characterization and the challenges towards the development of the final product. OLEDs were fabricated by thermal evaporation of AlQ_3 which has emission in the green part of spectrum (535nm) which gets partially absorbed by the poryphyrin films. The photoluminescence from these films were then monitored by thin film plasma enhanced CVD grown photodetectors. The Electron Cyclotron Resonance (ECR) and Very High Frequency (VHF) deposition regimes were used for this study. The photodiodes were engineered to have minimum sensitivity around 535nm (OLED spectrum) and have maximum sensitivity around 640nm, which is the emission from the sensor. The sensor viability study was done both in photoluminescence (PL) intensity and lifetime mode. The decay lifetime mode eliminates the need for filters and making the system immune to the degradation effects. This study though makes the frequency response study of these photodetectors very important. The design of the oxygen sensor is shown in the figure 8.1.

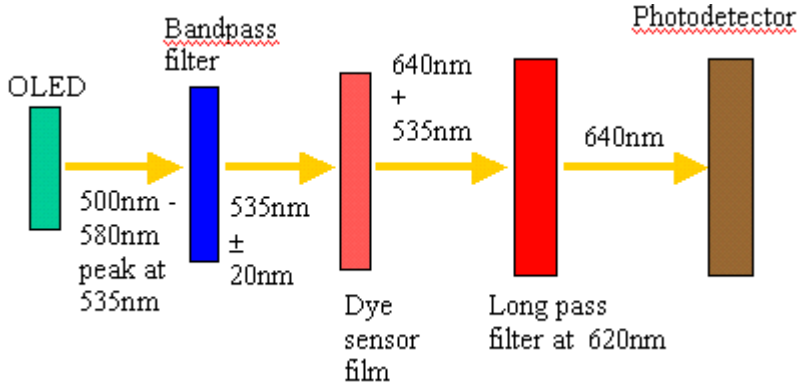

Figure 8.1: Schematic of design of the oxygen sensor in front detection

Hence we see that apart from the filters, the sensor can be divided mainly into three major components: OLED, sensor dye film and photodiode. The OLED and sensor dye film were developed by collaboration with other groups and the main research was devoted towards the development of the photodiodes with the subsequent integration of the components.

8.2 OLED fabrication and its emission spectrum

The OLED was deposited on ITO coated glass substrates. After cleaning and the ozone treatment of the substrates, the layers for the OLED are deposited using thermal evaporation. The top contact was also deposited by another thermal evaporation to fabricate the whole structure. The whole process was performed inside a glove box to enhance the lifetime of the devices and they were then encapsulated to further enhance the lifetime during operation. The device structure of OLED is shown in the schematic below:

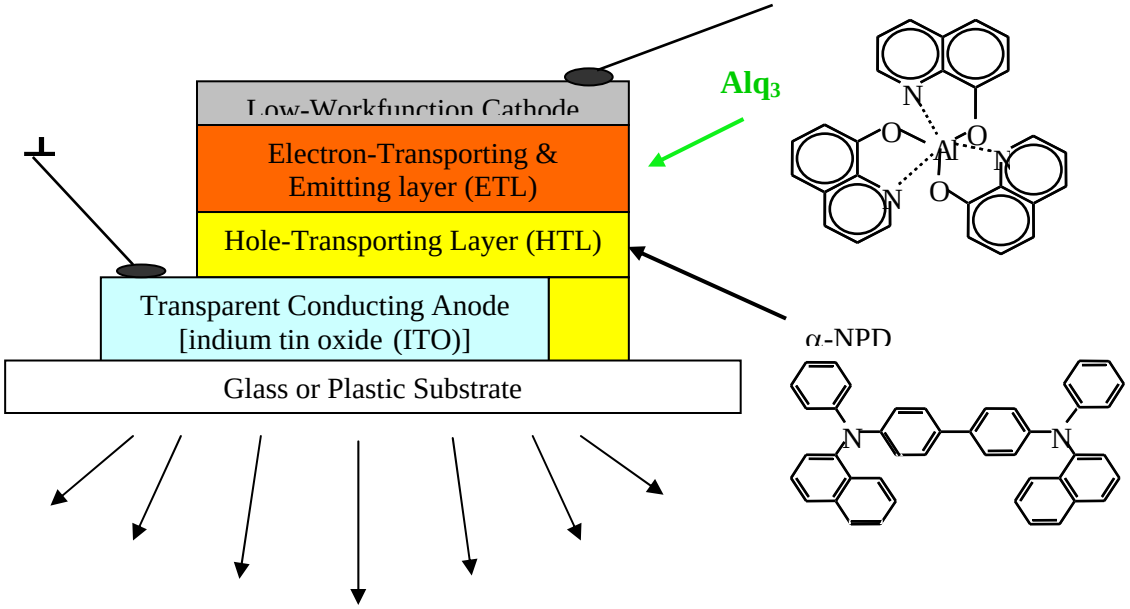

N,N'-diphenyl-N,N'-bis(1-naphthyl phenyl)-1,1'- biphenyl-4,4'-diamine (α-NPD)

Figure 8.2: OLED device structure

OLED fabricated comprised of AlQ_3 as the emissive layer. Coumerene doping was used to narrow down the spectrum of the OLED so that the background effects can be

minimized at source. The longpass filter mostly stops the background light, but it's not perfect. At such high brightness of OLED, there is always some minute leaking of the OLED light and it becomes significant considering the weak response of the sensor dye film.

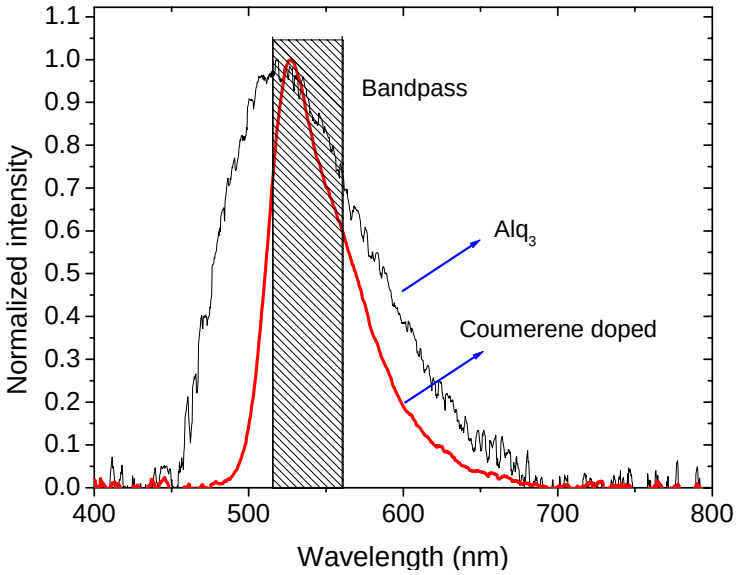

Figure 8.3: Narrower spectrum for coumarin doped OLED

8.3 Sensor dye film

The sensor dye film was embedded in polystyrene by drop casting. The thin film was formed and was exposed to the desired ambient to be used as oxygen sensor. Two porphyrin dyes were used for the study, PdOEP and PtOEP as shown in the figure 8.4:

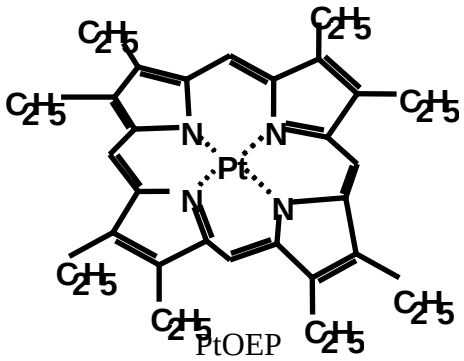

PtOEP

Absorption ~ 538 nm
Emission ~ 635nm

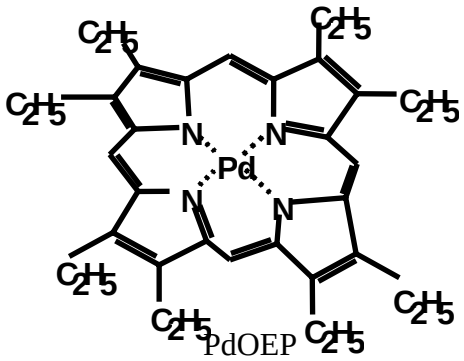

PdOEP

Absorption ~ 550 nm
Emission ~ 645nm

Figure 8.4: Molecular structure of the sensor dye films

The PdOEP film shows higher sensitivity compared to PtOEP film both in intensity and lifetime modes. Though the quenched lifetime is about 5 μs for both the films, but the unquenched lifetimes are 1.1ms and 90 μs respectively for PdOEP and PtOEP, resulting in 10 times higher sensitivity for PdOEP in frequency response mode. Also the absorption peaks of the two polymers are also different.

8.4 Optimization and development of photodiodes

8.4.1 Transparent contact characterization

The ITO coated glass was used as the substrate for the photodiode deposition with this side acting as the transparent contact for the entry of light. The PECVD deposition directly on ITO results in poorer performance and lower efficiency. It can be correlated to the reduction of ITO by the hydrogen plasma to indium and tin, resulting in decrease of transmission of the ITO substrate. This reduction of transmission results in reduction of sensitivity of the device. So two methods were proposed, one was to sputter a thin layer of molybdenum (Mo) on the top of ITO coated glass which is well known to block the hydrogen penetration and it also blocks the Na ions going into the device from the glass substrate. But unfortunately the devices using Mo resulted in more shorts in the device.

Alternative way was to sputter ZnO on top of ITO. It works best when the ZnO thickness is chosen such that it also acts as an antireflecting layer between ITO and Si. The undoped ZnO was deposited with 75W at 150C for 10 min resulting in a thickness of 0.91 μm thickness. The transmission was around 85% at 640nm. But the incorporation of ZnO resulted in two peaks in the QE spectra. The peaks were at 540 and 600 nm compared to 570 nm initially. So a thinner ZnO was tried to see if there is some change in the QE spectra of the device. But unfortunately it came out to be short, so we continued with the thicker ZnO. The damage to bare ITO under hydrogen plasma was also observed, which was eliminated by using a ZnO layer on top of it as shown in the figure 8.5.

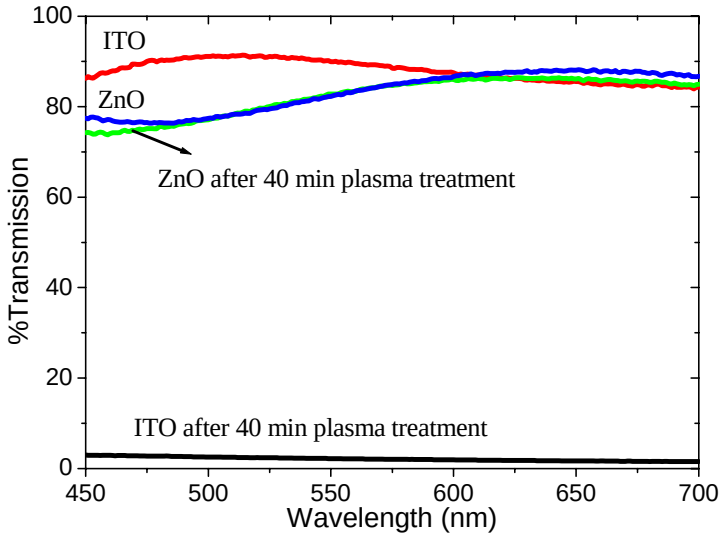

Figure 8.5 (a): Effect of hydrogen plasma

Figure 8.5 (b): ITO after hydrogen plasma treatment

We can see that there is very little change in transmission with ZnO layer after hydrogen plasma treatment. ITO transmission reduces in hydrogen plasma due to reduction to Indium and Tin, which are opaque.

8.4.2 ECR grown devices

Amorphous silicon devices were grown initially on top on TCO (transparent conductive oxide) which was ZnO in this scenario. The thin film devices using amorphous silicon has been developed over some period with moderate efficiency for photodiode devices in the ultraviolet spectrum [51]. The parameters required tuning for optimized device property improved performance. All the layers were grown in the same reactor sequentially one after another. Appropriate dummy layers have to be used in between the doped and undoped layers to minimize the contamination and memory from the previous runs. The temperature was chosen appropriately to have better expected device properties. Table 1 gives the summary of the parameters.

Table 8.1: Parameters for ECR deposition of amorphous silicon devices

Layer	**Temp**	**Time**	**Pres**	**Power**	**H_2**	**He**	**SiH_4**	**CH_4**	**B_2H_6**	**TMB**	**PH_3**
P+	180	30s	10mT	5		50	50		100		
		5min	10mT	5		50	50	7	100		
I	250	60min	15mT	5	60		15			15	
N+	250	10min	10mT	6.2	60		60				25

Table 8.2: Summary of I-V characteristic comparison before and after annealing

Parameter	Before annealing	After annealing
V_{oc}	0.736 V	0.736 V
I_{sc}	0.454 mA	0.443 mA
FF	50.8	52
R_{series}	253 ohm	220 ohm
R_{shnt}	16.7 Kohm	17.7 Kohm

The dark current was 0.5 μA @ 0.5 V reverse bias. The intrinsic layer thickness was 0.41μm. Then we measure the Quantum Efficiency (QE). The QE spectrum is given in the figure below:

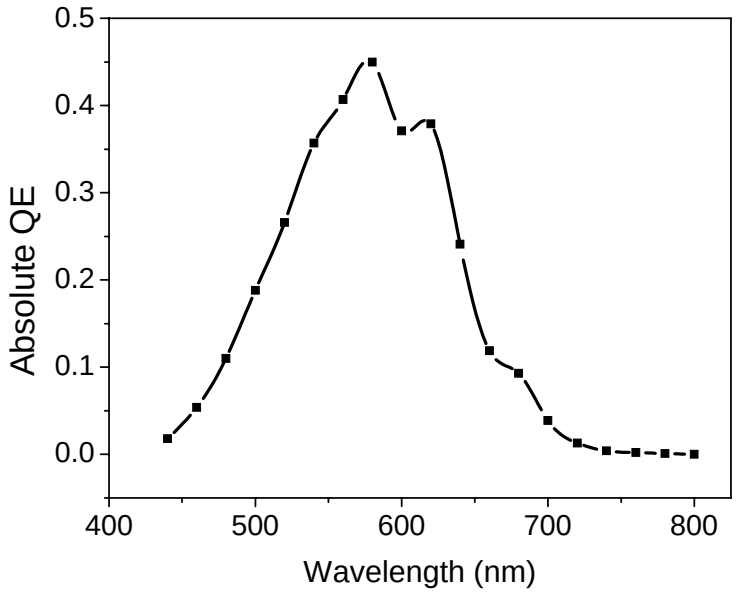

Figure 8.6: QE of a-Si device

Efficacy of using ZnO on top of ITO

So we first verify whether ZnO layer which we are putting is actually better for the device performance. To investigate that, we deposit ZnO only partly on the substrate and deposit the device layer half on ITO and half on ZnO as shown in the figure 8.7.

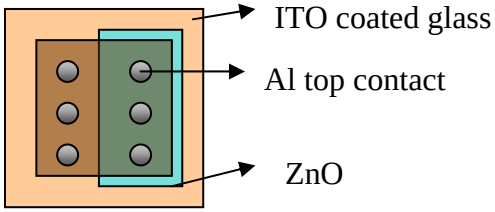

Figure 8.7: Device structure for evaluating the efficacy of using ZnO layer

The device was fabricated on both the parts at the same time and the metallization is also done together to ascertain similar device deposition conditions. The I-V characteristic comparison for the devices is given in table 3.

Table 8.3: Comparison of I-V spectra in ITO and ZnO layers

Parameter	Device on ITO	Device on ZnO
V_{oc}	0.5 V	0.49 V
I_{sc}	0.255 mA	0.377 mA
FF	40.4	39.2
R_{series}	642 ohm	488 ohm
R_{shnt}	7.7 Kohm	3.69 Kohm

We observe that device on ZnO is better since it has higher short-circuit current and also higher absolute QE compared to ITO contact due to protection from hydrogen plasma reduction of ITO as discussed earlier. The QE spectrum is shown in the figure 8.8.

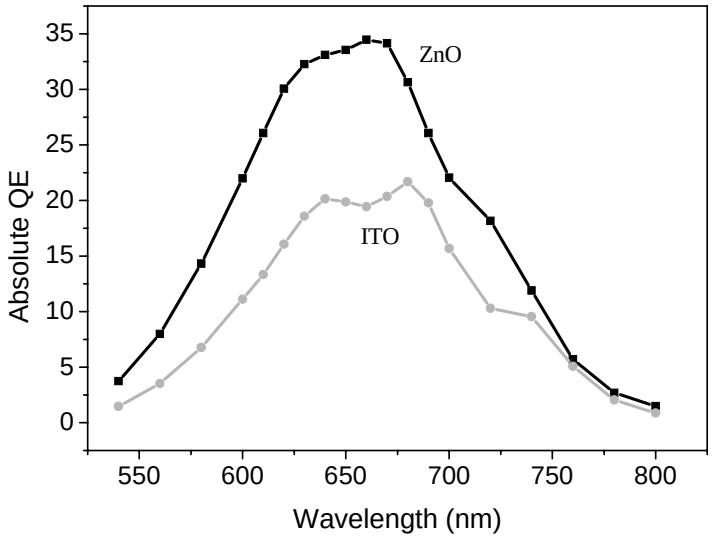

Figure 8.8: Improvement of QE on having ZnO layer

But the problem arises in the dark current. The dark current on ITO is 9 x 10^{-8} A at 0.5V compared to 6.8 x 10^{-5} A on that on ZnO. This indicates that the ZnO layer needs improvement since there is a higher dark current as shown in the figure 8.9.

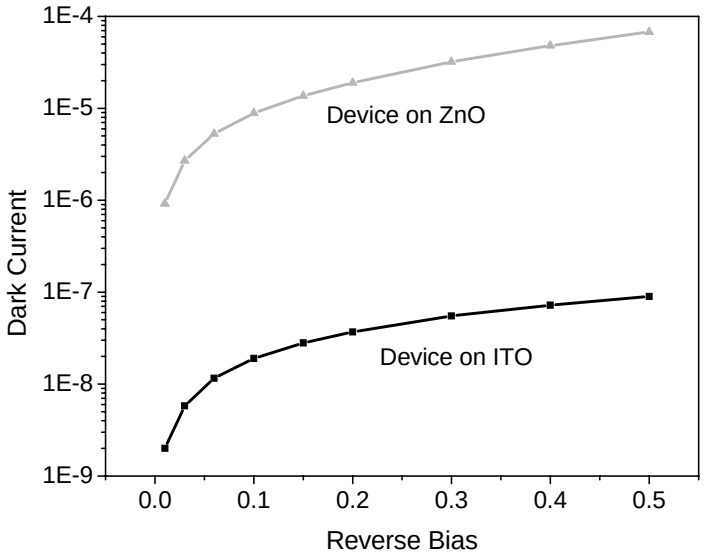

Figure 8.9: ZnO resulting in higher dark current

8.4.3 Optimization of ZnO layer

Effect of thickness and power on transmission and growth rate of ZnO has significant effect on the quality of the ZnO. Especially for lower it's well known that ZnO grown at

lower power is denser and has better electrical properties. The samples were grown using sputtering with 40 sccm flowrate of Ar and 20 sccm flow rate of O_2. The oxygen is very crucial is determining the sheet resistance of the grown film. In the general film grown with no oxygen shows higher resistance and hence will be inappropriate for the devices. The pressure of 10mT and temperature of 150 C was seen to be optimum for the ZnO deposition.

Table 8.4: Summary of optimization of ZnO layer

Power	**Deposition time**	**Thickness**	**Growth rate**	**Transmission @ (640nm)**	**Colour**
75 W	10 min	0.9 μm	90nm/min	85%	Bluish
75 W	5 min	0.47 μm	94nm/min	78%	Blackish
75 W	15 min	1.37 μm	91nm/min	84%	Reddish
60 W	20 min	1.32 μm	66nm/min	87%	Reddish
50 W	25 min	1.41 μm	56.4 nm/min	90%	Light red
40 W	25 min	1.08 μm	43.2nm/min	78%	Blackish
30 W	80 min	0.8 μm	10nm/min	83%	Bluish

We observe that the 30W ZnO is quite dense with good electrical properties. So we go ahead with using this ZnO but much thinner around 0.1μm compared to about 1μm used earlier. The reduction of thickness has two advantages, first of all it reduces the overall resistance, and in addition the lower thickness has denser ZnO and hence lower resistivity. The 0.1 μm thick film was light reddish in colour with transmission of 91% at 640nm. So we have only 1% loss of transmission due to ZnO since 8% loss is due to the glass substrate itself. But with the ZnO characterization, it was possible to reduce the sheet resistance of ZnO by half enhancing the performance of devices especially in having higher short circuit currents. The fill-factor also increased to 65.9 from 52 using the new ZnO though this is insignificant for photodiodes as we can apply bias to the devices unlike solar cells. But higher FF also implies lower sensitivity dependency of the photodiodes on the bias voltage. This has an indirect advantage since lower required bias voltage also implies lower dark

currents. The dark current was also 15 times lower, though the reason for the same is not well understood. It immediately resulted in higher QE as shown in the figure 8.10.

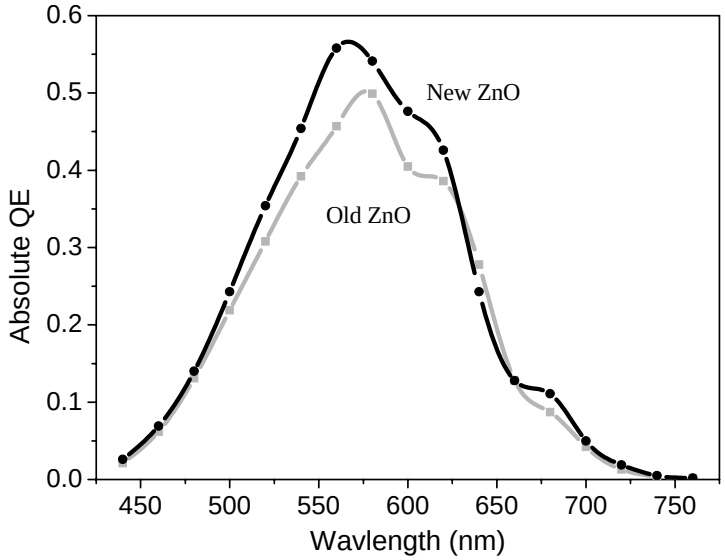

Figure 8.10: QE remains unchanged with new ZnO

8.4.4 Effect of adding Germanium

Then we realize that the QE spectrum needs to be shifted further towards higher wavelengths to the desired value of 640nm as max QE. One option was to make the p layer thicker, but that would result in decrease of absolute QE value. Se we decide to use amorphous SiGe instead of a-Si along with slight increase in the p+ layer thickness. The QE indeed shifted but the device quality deteriorated on adding 10% Ge to the intrinsic layer. Also the p layer is made intentionally thicker with no carbon resulting in lower bandgap p+ resulting in suppression of QE at lower wavelengths. The QE spectrum is shown in the figure 8.11.

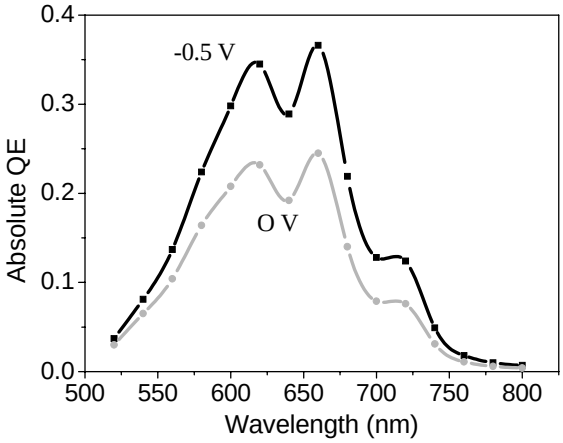

Figure 8.11 (a): No Ge in p+ layer

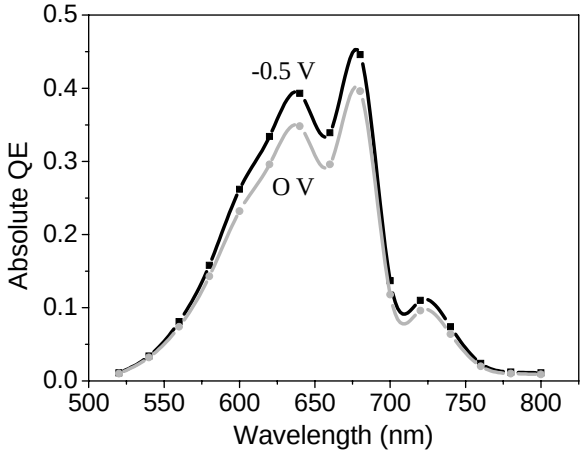

Figure 8.11 (b): Ge in p+ layer

We see that there is lower bias dependence on adding Ge to p layer indicating better collection efficiency. In addition the absolute QE is also higher, which will be better for the sensor performance. But unfortunately there is tremendous increase in dark current on addition of Ge in the p layer. So we compensate by adding higher Ge in I layer and correspondingly reducing in the p layer. So we need to tune the p and I layer further to increase the absolute QE. The I-V summary for the devices is given in the table 8.5.

Table 8.5: Effect of Ge on the I-V parameters

Parameter	a-Si device	10% Ge in I layer	2.4% Ge in p and 10% Ge in I layer	1.6% Ge in p and 13% Ge in I layer
V_{oc}	0.736 V	0.657 V	0.656 V	0.6 V
I_{sc}	0.454 mA	0.287 mA	0.33 mA	0.393 mA
FF	50.8	41	44.6	41.4
R_{series}	253 ohm	320 ohm	372 ohm	383 ohm
R_{shnt}	16.7 Kohm	4.98 Kohm	9.13 Kohm	5.72 Kohm

It is observed that the V_{oc} has gone down due to addition of Ge which was expected as the bandgap of the materials is decreasing with Ge incorporation. The I_{sc} has gone down due to poor film quality compared to amorphous silicon. The FF detoriated drastically and is prominent in the I-V curve. The I layer thickness was also pretty close which was 0.475 microns compared to 0.41 microns for a-Si. We observe that there is tremendous increase of dark current on addition of Ge in the p layer. So we decrease the Ge in p layer and to

compensate, we increase the Ge in the I layer. It indeed reduces the dark current by a huge amount, but still it was higher than that without Ge in p+ layer. So the effect of adding Ge can be summarized in the figure 8.12.

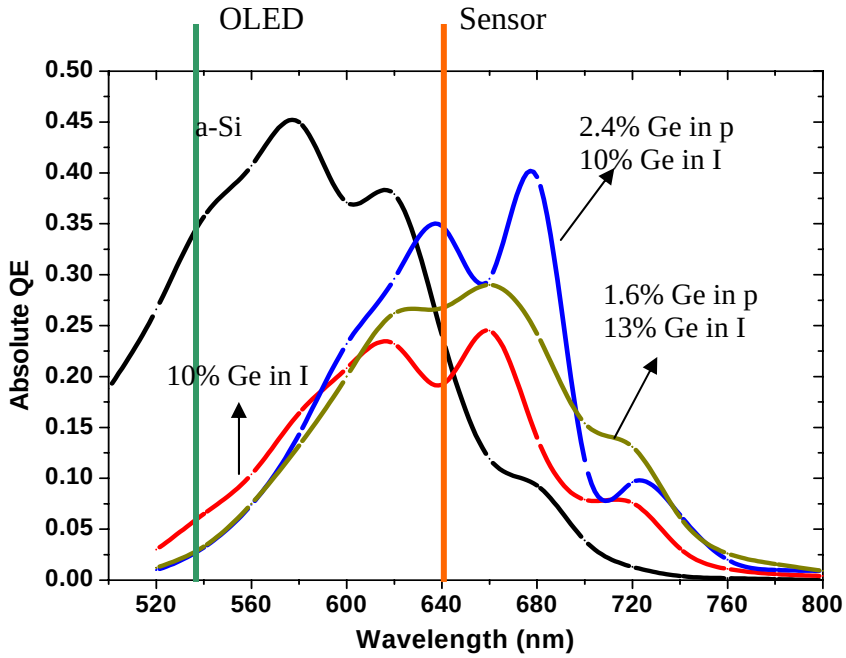

Figure 8.12: Comparison of QE of photodetectors

The dark current reduces in compensating with higher Ge in I layer. The I-V characteristic of the devices are also dependent on the Ge concentration both in the p and I layers. The I-V is shown in the figure 8.13.

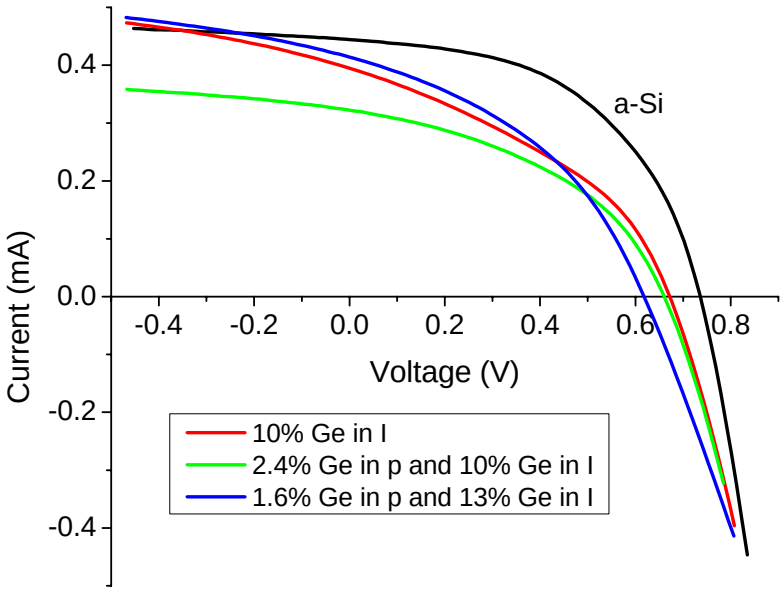

Figure 8.13: Comparison of I-V of photodetectors

The current reduces on increasing the Ge content in the p layer, which can be partially compensated by increasing Ge content in I layer. Also we can observe the decrease of open circuit voltage with more and more Ge incorporation. The dark current goes up prominently with the addition of more Ge in the P and I layers. The comparison of dark currents is shown in the figure 8.14:

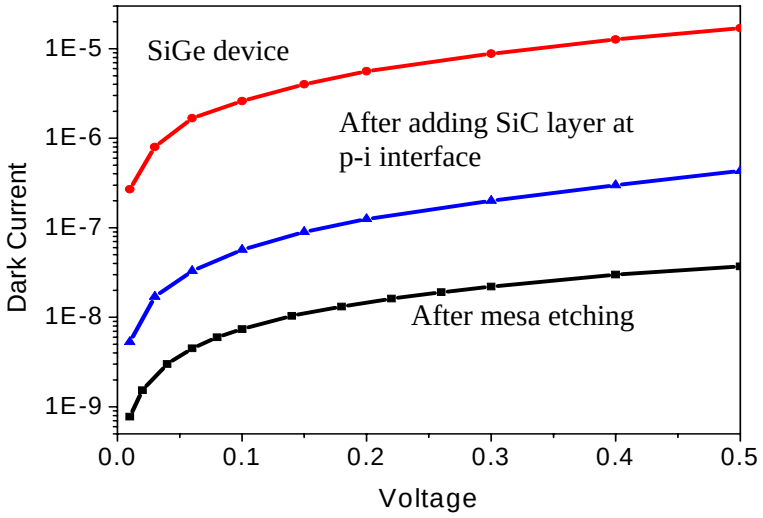

Figure 8.14: Comparison of dark current of photodetectors

Dark current can be reduced significantly by incorporating SiC as the window layer. In addition to that there is a significant reduction of surface leakage current with mesa-etched structure.

8.4.5 Effect of deposition pressure

The figure below shows the possible improvement of the SiGe device with deposition under lower pressure. The lower pressure results in higher ion bombardment due to larger mean free paths of the ions. In general SiGe requires harsher deposition environment to facilitate better surface mobility of the heavier Ge ions.

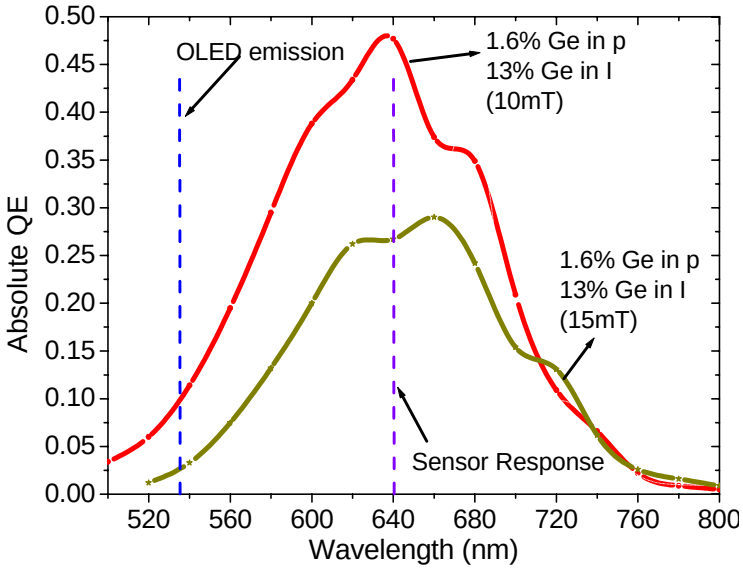

Figure 8.15: Effect of lower pressure deposition

8.4.6 Effect of adding Silicon Carbide on dark current

Next we see the effect of adding SiC in the p-i interface on the QE of the device. We expect the dark current to go down along with restricting the diffusion of boron across the p-i interface. The QE goes down due to the addition of the SiC layer and also shifts slightly towards lower wavelengths. But the advantage was observed in the reduction of dark current by an order of magnitude.

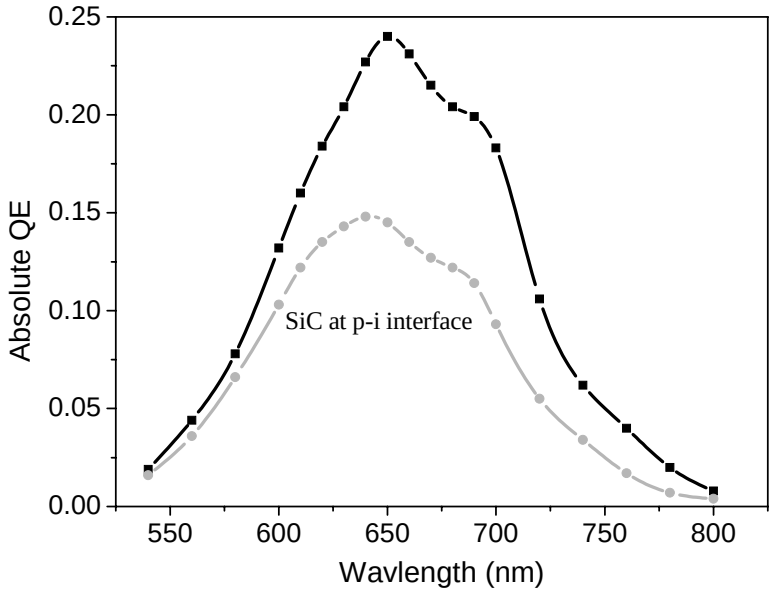

Figure 8.16: Effect of adding silicon carbide at p-i interface

Hence we try a different regime by placing the same thickness of SiC as a window layer prior to growing the p+ layer. The V_{oc} increases very slightly, but the dark current goes down by an order of magnitude as observed earlier. But unfortunately the I_{sc} also goes down very slightly compared to earlier case. The QE spectrum is better with SiC as a window layer as shown in the figure 8.17.

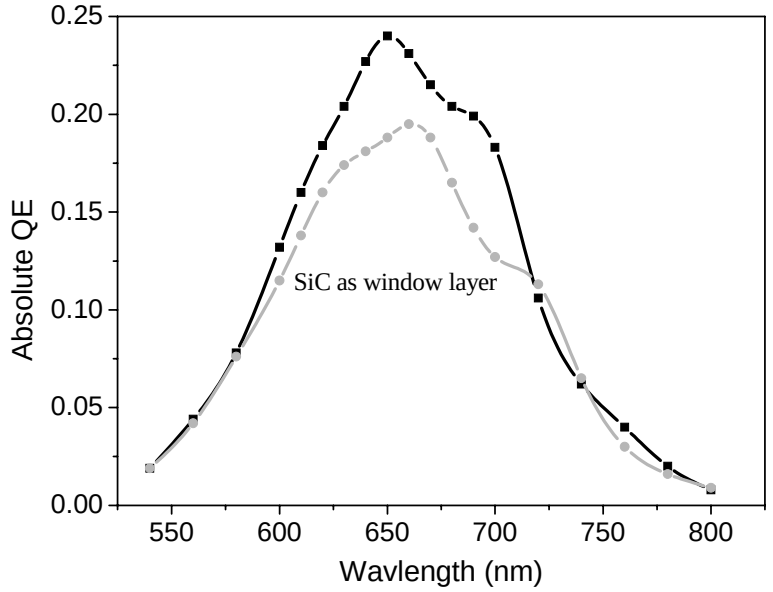

Figure 8.17: Effect of adding silicon carbide as window layer

8.4.7 Effect of intrinsic layer thickness

Next we study the effect of I layer thickness on the device characteristics. The QE spectrum is shown in the figure 8.18.

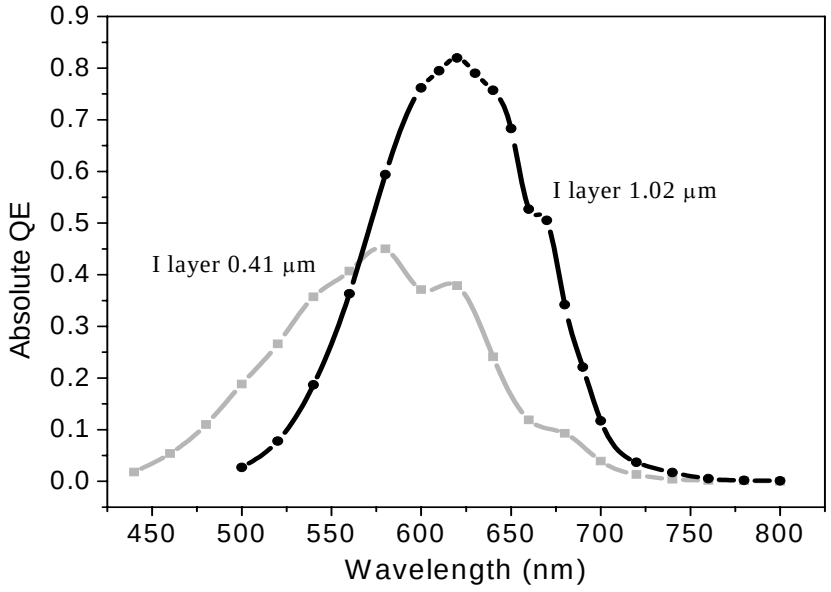

Figure 8.18: Effect of I layer thickness on QE

I layer thickness increases the absolute QE and shifts the spectrum towards higher wavelengths. The increased QE can be attributed to the increased absorption in the layer. But the shifting of spectra results due to improper collection of electrons generated by low wavelength photons, which are absorbed in the initial layers of I layer after P side. These electrons now have to travel through the thick I layer to reach the n+ side. This phenomenon is explained with a figure 8.19.

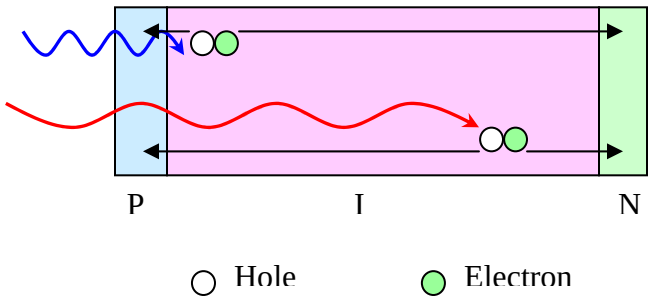

Figure 8.19: Different carrier generation position for different wavelengths

Hence we see that there a difference arises due to different penetration depths of wavelengths. The different penetration depths results due to reduction of absorption coefficient at lower energies. The lower QE at low wavelength is attributed to improper electron collection.

But the recombination problems also start becoming dominant with higher and higher thickness due to the low diffusion lengths for the amorphous silicon compared to nanocrystalline and crystalline silicon. This in turn results in slower frequency response due to higher carrier transit time. The frequency response if thicker device should be faster due to lower device capacitance but after a limit it becomes dominated by increased transit time resulting in slowing of response.

The dark current was an order of magnitude lower. The mesa etch further reduced the dark current of the device. The top n+ layer area surrounding the device was etched off, with slight over-etch to top part of I layer. We indeed see the improvement in dark current on doing RIE. The dark current before and after RIE is shown in the figure 8.20.

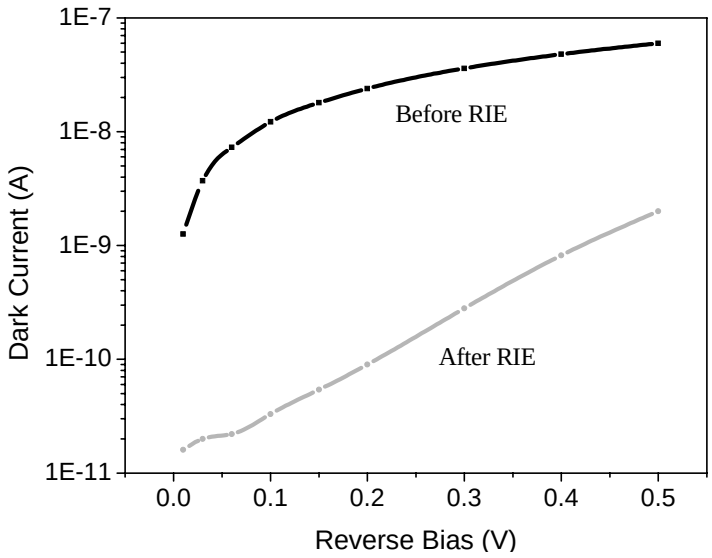

Figure 8.20: Reduction of dark current with mesa structure

8.5 Modes of oxygen sensor operation

Next we notice the modification of the photodetector response by the sensor. The sensor film used was PtOEP, which absorbs at 538nm and emits at 635nm. Hence for the

initial sensor and photodiode integration, the sensor film was excited using a monochromatic light. The experimental set-up used is shown in the figure 8.21.

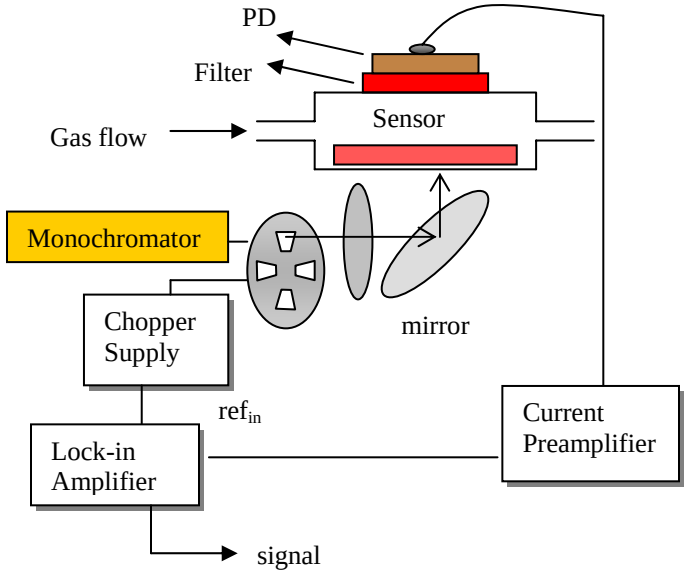

Figure 8.21: Experimental setup for quantum efficiency

The sensor modifies the response by partially absorbing the monochromatic light and emitting at 635nm, which is turn passes though the longpass filter and is being detected by the photodiodes as shown in the figure 8.22.

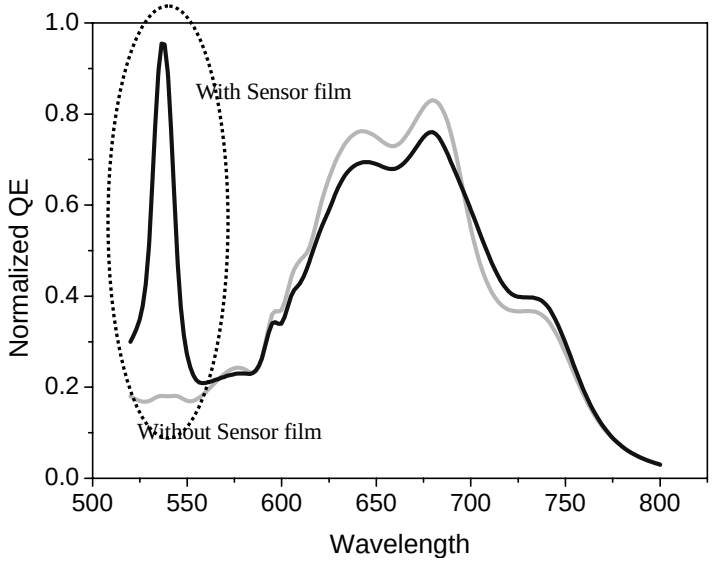

Figure 8.22: Sensor film response detection with photodiode

There are two ways for oxygen sensor operation

- Intensity mode
- Lifetime mode

The intensity mode being the most simple way of measurement, but suffers from degradation and photobleeching effects of both OLED and sensor film. The lifetime mode being dependent only on the photoluminescence decay lifetime and not on the actual intensity of excitation, is rather independent of those effects. So we first study the simplest intensity mode measurement.

8.5.1 Intensity mode measurements

Next we observe the effect of sensor dye ambient to the sensor response. The response was observed in 100% N_2, 20% O_2, 100% O_2. The sensitivity obtained was around 25 between 100% N_2 and 100% O_2. We observe that the sensor is more sensitive in low oxygen concentrations as shown in the figure 8.23.

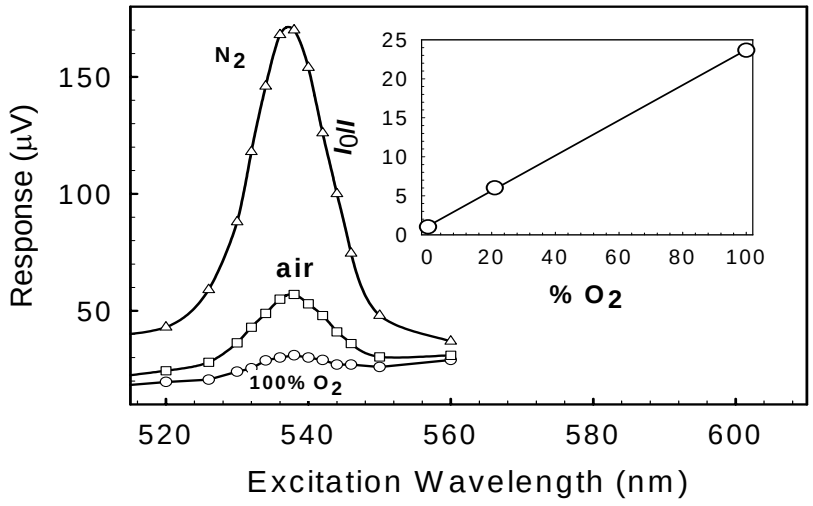

Figure 8.23: PtOEP response under different ambient

The ratio obtained was also dependent on the method of measurement and also on the photodetector. So chopped light method using a lock-in amplifier to minimize the noise at

other frequencies and hence enhancing the noise margin. The response for the thin film and the commercial photodetector is compared in the figure 8.24.

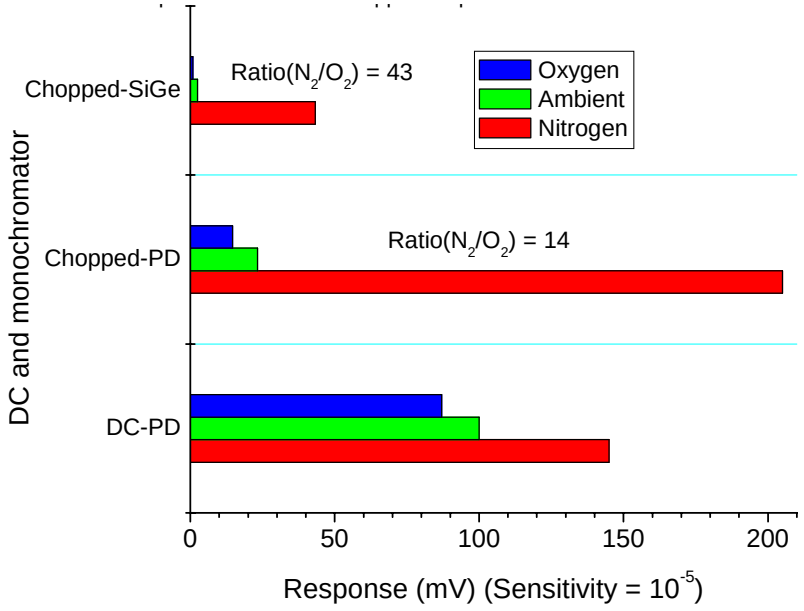

Figure 8.24: Effect of measurement method on sensor response

So we see that SiGe photodetector is more effective than the commercial crystalline silicon photodetector. This shows the efficacy of tuning the response of the thin film SiGe photodiode with minimized sensitivity to background light and maximum sensitivity to the wavelength of interest. Hence inspite of the crystalline Si PD being more sensitive, it gives lower sensitivity, as it is also more efficient in the background light. Also it was more effective when done with chopped light and lock-in rather than DC mode, which is largely influenced by noise due to dark current and stray light.

The sensitivity obtained was only 25 and we needed to enhance the sensitivity may be by using some other sensor dye. The solution was using PdOEP instead of PtOEP which shows higher sensitivity due to higher effect of oxygen on the photoluminescence decay lifetime as seen by the Stern-Volmer equation. Next we compare the absorbance spectra for PtOEp and PdOEp films in the figure 8.25.

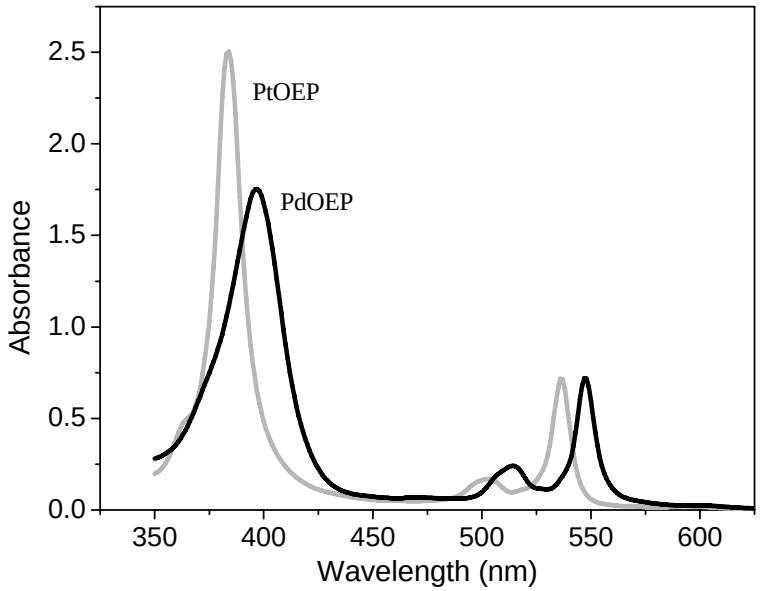

Figure 8.25: PtOEp and PdOEp sensor dye absorption spectra comparison

The absorption of PtOEp is at 538nm compared to 550nm for PdOEp. Also the absorbance in the UV region is higher compared to our current working wavelengths of 538 and 550nm indicating that sensor will work much better with UV excitation as it increases the background margin and also the response is higher. But it's restricted by the fast degradation of UV OLEDs and as well as the sensor dye film. Hence its results in a compromise for lower sensitivity of the oxygen sensor with increased reliability in the long run. The ambient response for the PdOEP film is shown in the figure 8.26.

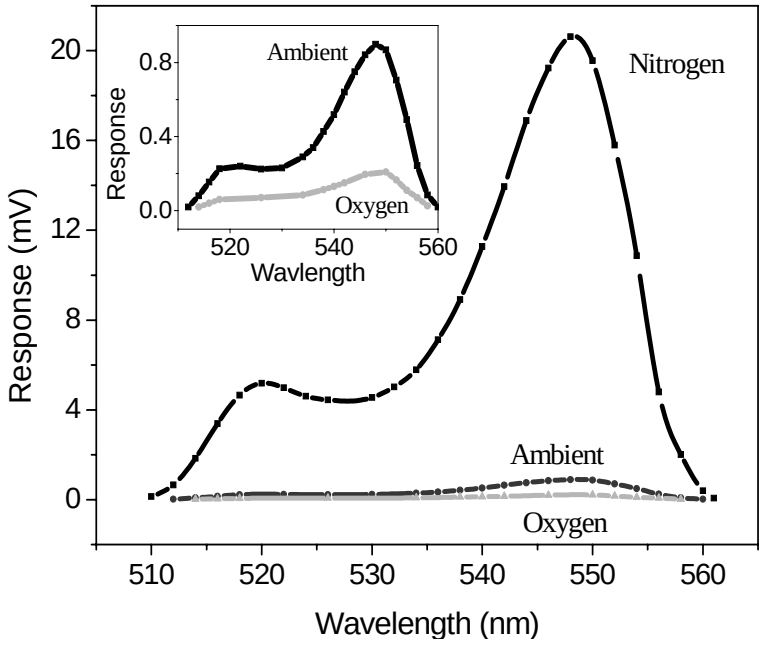

Figure 8.26: PdOEP response under different ambient

We obtain a much higher sensitivity of around 80 with the PdOEP sensor film. Hence we made a significant progress in terms of the sensitivity of the sensor dye film. We need the highest possible sensitivity to start with since on integration, we will obtain lower sensitivities. Next we had to confirm if the intensity of the light has any effect on the sensitivity of the sensor since it will affect the final sensor reliability.

8.5.2 Effect of intensity on sensitivity

The ratio of the sensor film remains unchanged on changing the intensity of excitation source. The intensity was varied using a neutral density filter along with a monochromatic light source. The figure 8.27 shows the independence of the sensitivity with the excitation intensity showing the bright side of the measurement.

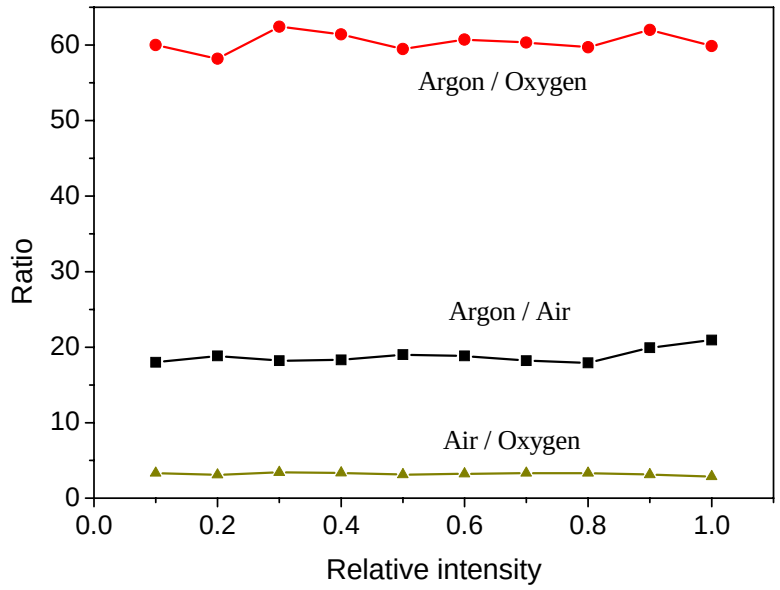

Figure 8.27: Independence of sensor response with excitation intensity

8.5.3 Effect of adding titania particles to sensor film

The sensor response on addition of TiO_2 increases by 4 times. Though the sensitivity remains almost the same, but the actual response increases also by 4 times. The advantage on having higher intensity is the ease of more accurate detection by the thin film photodiode. The increase of response facilitates better detection as shown in the figure 8.28.

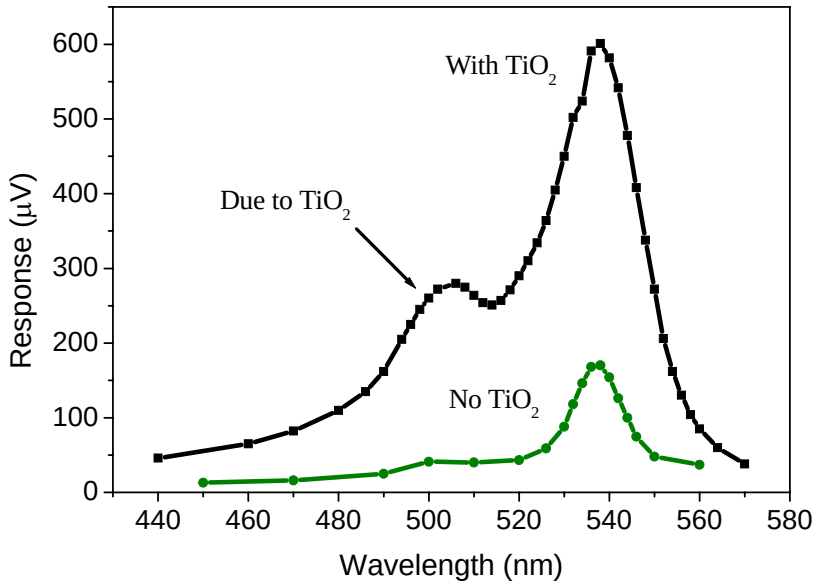

Figure 8.28: Effect of adding TiO_2 to sensor response

Similar effects were also obtained on adding TiO_2 to the PdOEP film. The enhancement of the response is attributed to the scattering of the excitation light in the TiO_2 particles resulting in multiple reflections within the film resulting in higher chance of absorption in the film as shown in the figure 8.29.

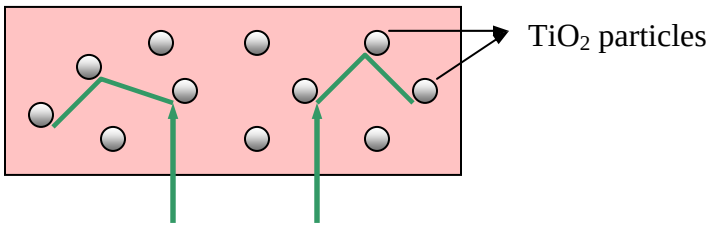

Figure 8.29: Scattering of light due to TiO_2 particles

It was also confirmed that TiO_2 neither absorbs the excitation wavelength and nor the emitted wavelength. The sensitivity was also confirmed to be about the same. But it was observed that the response to argon was slower due to presence of titania particles. It was inferred that its happening due to higher porosity of the film and the slow response is due to the trapped and adsorbed oxygen molecules in the pores. So inspite of the advantage of increased response it might restrict the sensor speed to ambient.

8.5.4 Lifetime mode measurement

The lifetime mode measurement monitors the change of lifetime of phosphorescence of the sensor dye film with oxygen and nitrogen ambient. For these mode to work we require fast photodetector operation which in turn necessitates the study of the frequency response of the photodetectors. In this mode the oxygen shortens the photoluminescence decay lifetime as shown in the figure 8.30.

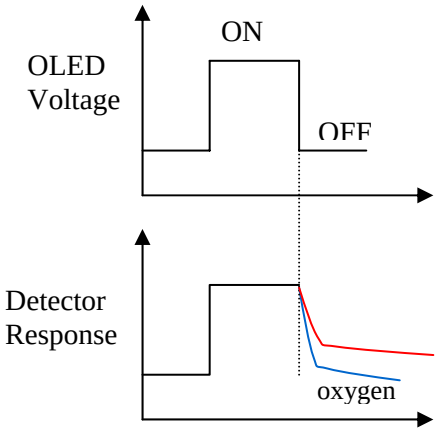

Figure 8.30: Lifetime mode of sensor operation

8.5.5 Wavelength dependent frequency response of Photodiode

The frequency response for both a-Si and a-SiGe photodetectors were studied at different chopping frequency of monochromatic light followed studying the effect of different wavelength on response speed. The frequency response of a-Si device is shown in the figure 8.31.

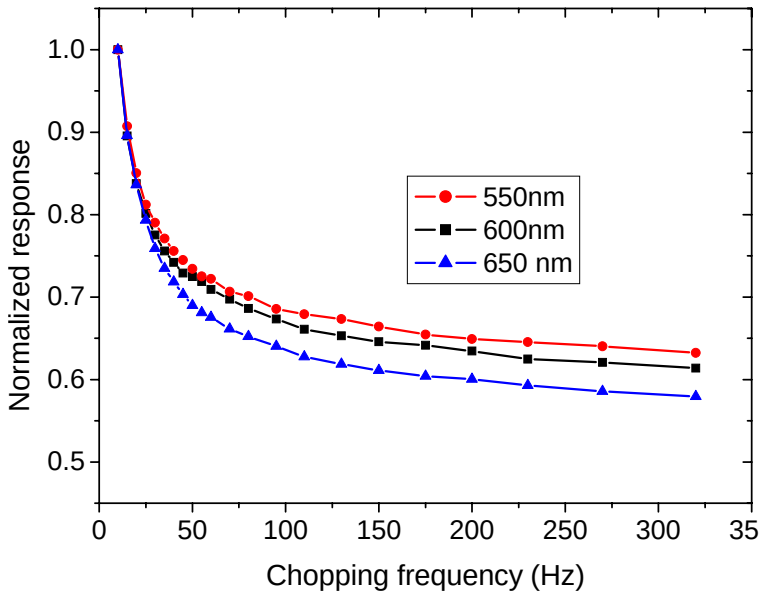

Figure 8.31: Response of a-Si device at different wavelengths

The change in absolute value of response can be related to the different QE at different wavelength. But the normalized response can be explained by the different penetration depth for different wavelengths resulting in different defect state resulting in different recombination pattern in the device. Similar effect has been observed by Georgigeskaya *et*^{al}. Similarly we also observe the a-SiGe device ad that also shows similar pattern as shown in the figure 8.32.

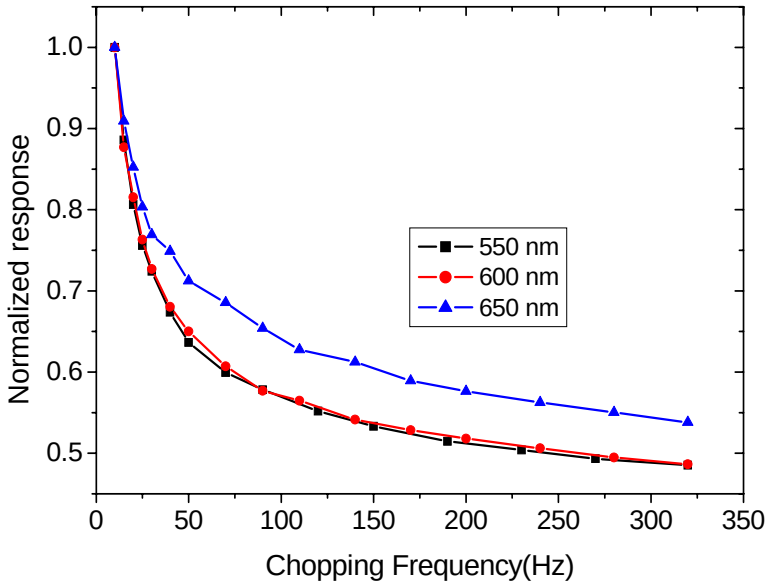

Figure 8.32: Response of a-SiGe at different wavelengths

We see that the normalized response goes to 0.66 for a-Si compared to 0.55 for a-SiGe. This happens due to the presence of more defects in the SiGe device, which starts responding in the lower frequencies. It was observed that the device is fastest at the wavelength of maximum QE which shows a correlation between the carrier collection and the frequency response. The comparisons for QE spectrum for both the devices are shown in the figure 8.33.

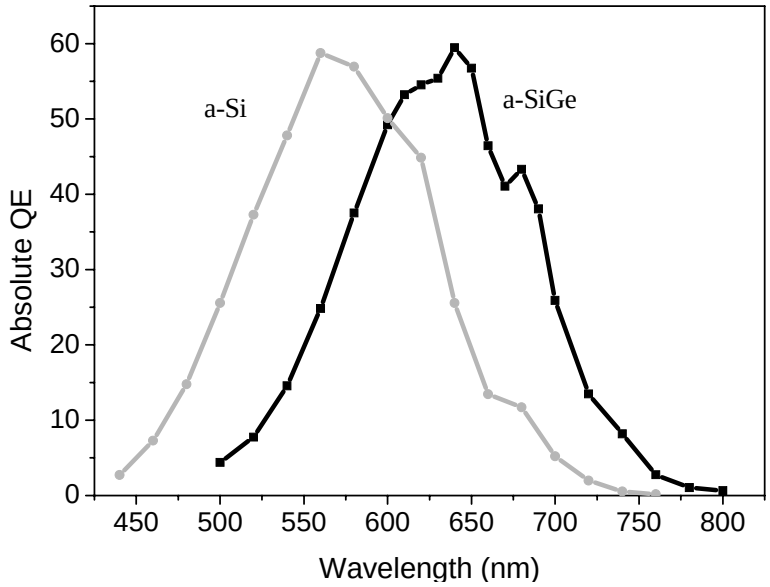

Figure 8.33: Comparison of a-Si and a-SiGe device

VHF grown devices

The VHF growth is quite a bit different from the ECR growth. Much higher growth rates are achievable due to higher possible deposition pressure. But the VHF deposition also results in higher ion bombardment and hence higher damage. The growth rate for amorphous silicon was increased from 6nm/min to about 20nm/min. The deposition pressure used for a-Si was 50mT compared to 15mT for ECR and then 25mT for VHF compared to 10mT for ECR. VHF at 25mT gave good devices due to higher intrinsic ion bombardment facilitating higher surface mobility.

8.6 Frequency response studies

The frequency response studies were carried out by applying intermittent electrical pulse to an inorganic LED and measuring the response of the photodiode. It was important for the lifetime mode operation of the sensor. The experimental setup is shown in the figure 8.34.

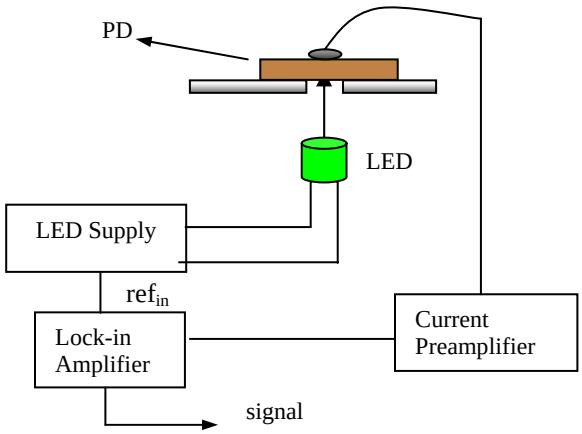

Figure 8.34: Frequency response measurement setup

8.6.1 Effect of TMB grading in the I layer

Two devices were fabricated, one with TMB grading in the I layer and one without. The I-V characteristics, the QE and also the frequency response were improved on reducing the p layer thickness.

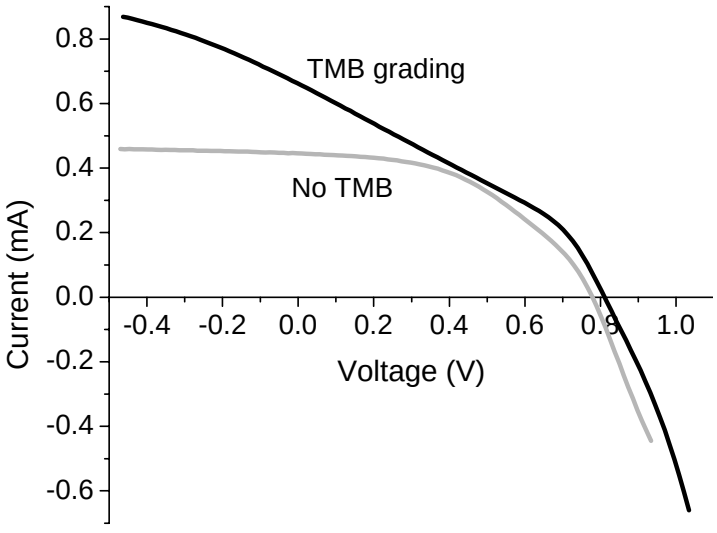

Figure 8.35: Effect of TMB grading on I-V

The short circuit current is higher for TMB graded device. The collection is better which is indicated by higher short circuit current. There is presence of built-in field due to the presence of TMB grading.

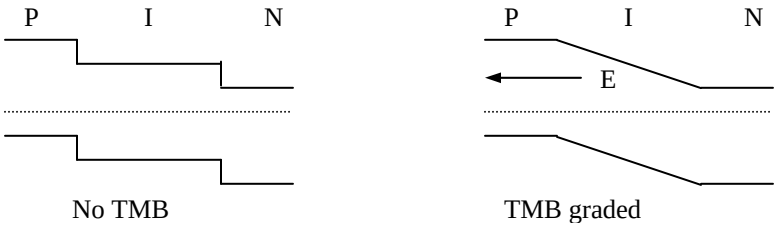

Figure 8.36: Built-in electric field with TMB grading

This also enhances the collection efficiency also resulting in faster frequency response. The increase of response with TMB also indicates that holes collection problem dominantly restricts the response speeds of the devices. The freq response is shown in the figure 8.37.

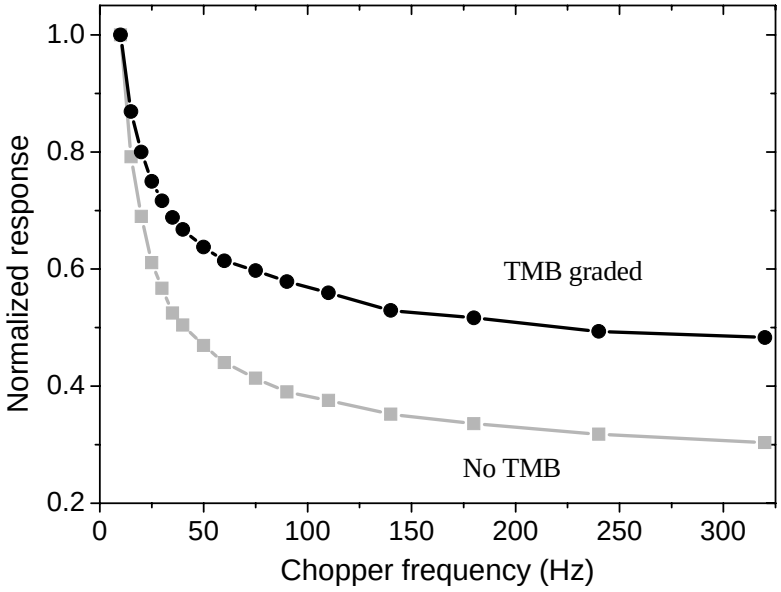

Figure 8.37: Effect of TMB grading on frequency response

So we suspect that collection is critical for faster frequency response. Next we intend to study the factors influencing the frequency response of the photodiode.

8.6.2 Effect of boron diffusion at p-i interface during growth

Accidentally we observe a strange effect with the devices. The same device was annealed first at 250^0C and then at 300^0C. Surprisingly when their frequency response was studied, they looked pretty different as shown in the figure 8.38.

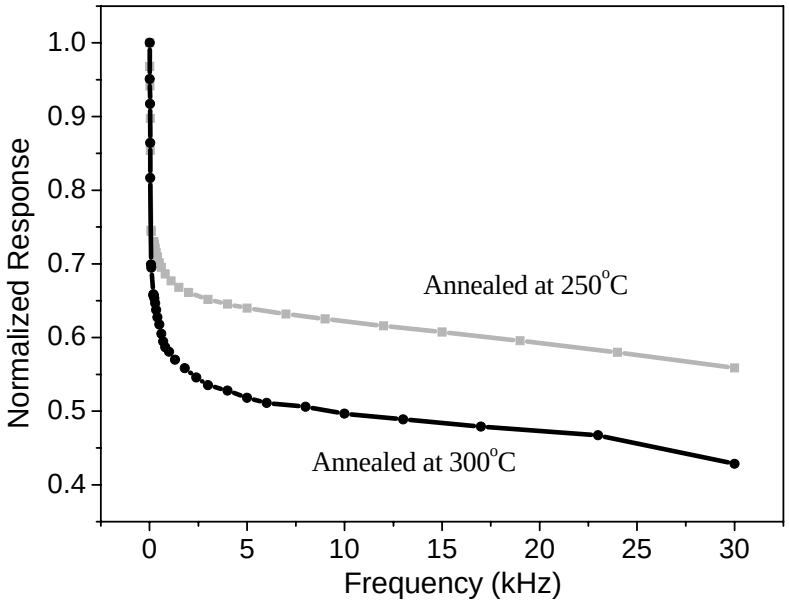

Figure 8.38: Effect of growth temperature on frequency response

Initially we wrongly interpreted the phenomena as the i layer defects changing with the annealing temperature. But that was unlikely since annealing should reduce the defects and should result in a faster response. The next possible explanation was the boron diffusion from the p+ layer to the i layer. To confirm the same we made n-i-p device instead of p-i-n and the frequency response was analyzed. The boron diffusion has been observed also by another group when the deposition temperature was above 200 degrees [52]. The boron diffusion is shown in the figure 8.39.

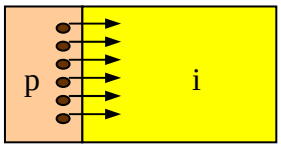

Figure 8.39: Boron diffusion during growth

A group has also verified the boron diffusion by a Secondary Ion Mass Spectroscopy (SIMS) profile to show the enhanced diffusion at 250 degrees as shown in the figure 8.4.

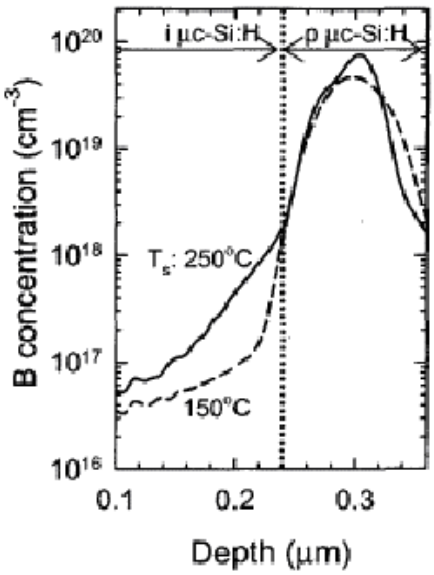

Figure 8.40: SIMS profile of the p-i interface [52]

The nip structure was n+ layer grown first followed by I layer and p+ layer was grown last. In addition one p-i-n device was also grown with exactly same parameters. To further confirm the same, we fabricated another device with a SiC barrier layer at p-i interface to hinder boron diffusion. The frequency response is shown in the figure 8.41.

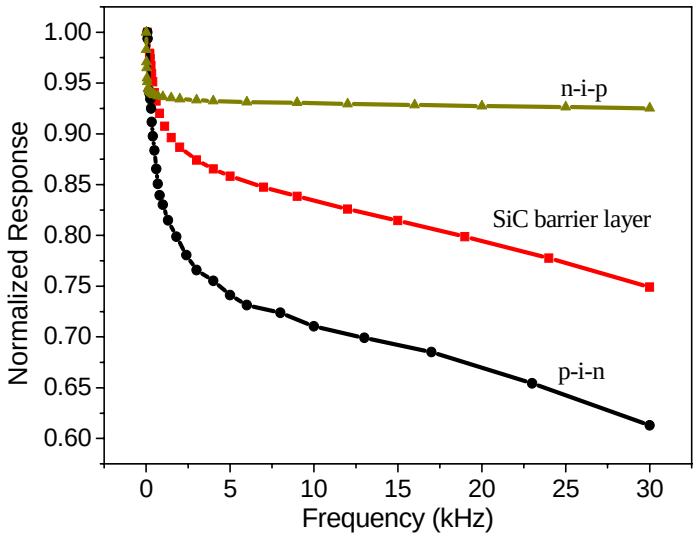

Figure 8.41: Improvement of frequency response with structural modification

The n-i-p structure has much lower boron diffusion since the p layer is grown last restricting the time for boron diffusion. It was observed that phosphorus diffusion wasn't a significant problem may be due to larger size of phosphorus atoms resulting in lower diffusion constants. In addition SiC layer was also beneficial for faster operation, but it also results in increased short circuit currents as discussed in the earlier sections. But SiC layers also reduce the dark current and hence may be beneficial considering both the factors.

Holes are most difficult to collect due to their lower mobility compared to the electrons. This was reflected by the lower collection in n-i-p device resulting in lower short circuit current. To test the same a device was fabricated with ITO contacts on both sides which made possible the study of effect of direction of illumination as shown in the figure 8.42.

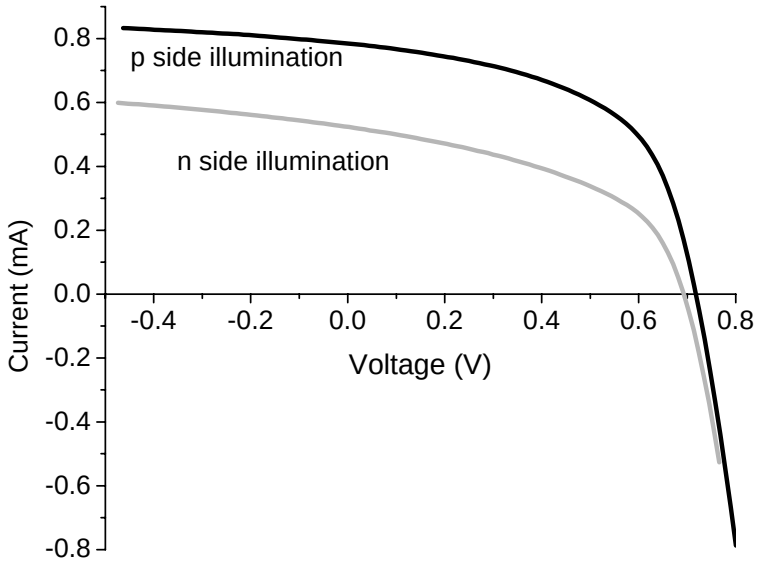

Figure 8.42: Effect of direction of illumination on I-V

We observe that there is mot much difference in the open circuit voltage. The improper hole collection is also reflected in the QE spectra. One p-i-n and other n-i-p device QE responses are compared side by side. The QE for p side illumination is higher compared to n side illumination. In the QE spectra n-I-p device shows larger variation with voltage which further justifies the logic of improper hole collection.

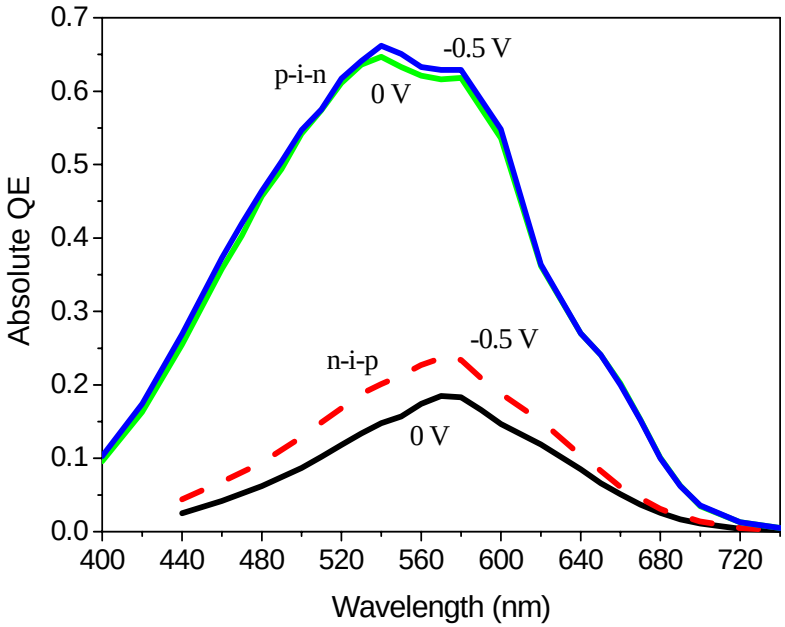

Figure 8.43: Effect of illumination side on QE

8.7 Sensor integration with OLED

On examining the better frequency response, we used a pulsed OLED to excite at different frequencies. An anomalous behavior was observed for the sensor film at different frequencies as shown in the figure 8.44.

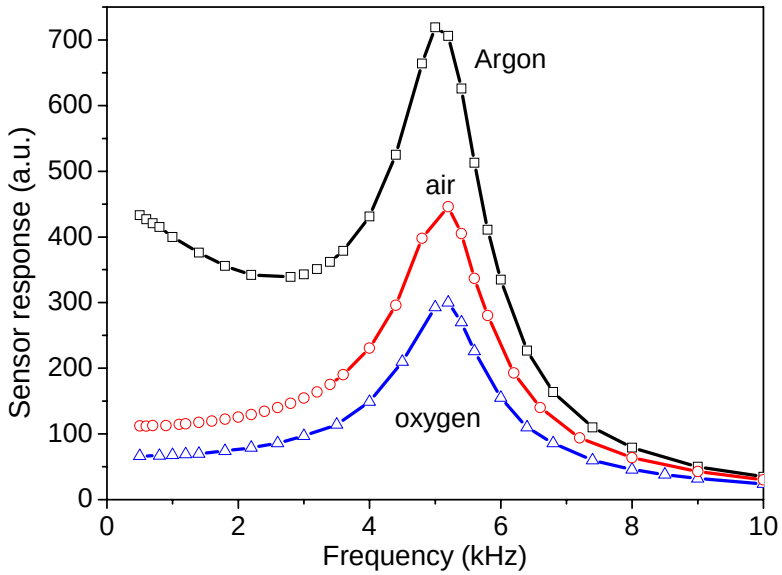

Figure 8.44: Effect of frequency in response at different ambient

8.7.1 Effect of excitation frequency on sensitivity

This behavior can be attributed to some artifacts arising from the system. It was especially confusing why the signal with argon ambient goes down compared to increase at lower frequencies at air and oxygen environments. Also we observed that the obtained sensitivity was only 7 compared to about 90 obtained with monochromatic light using the same film as shown in the figure 8.45.

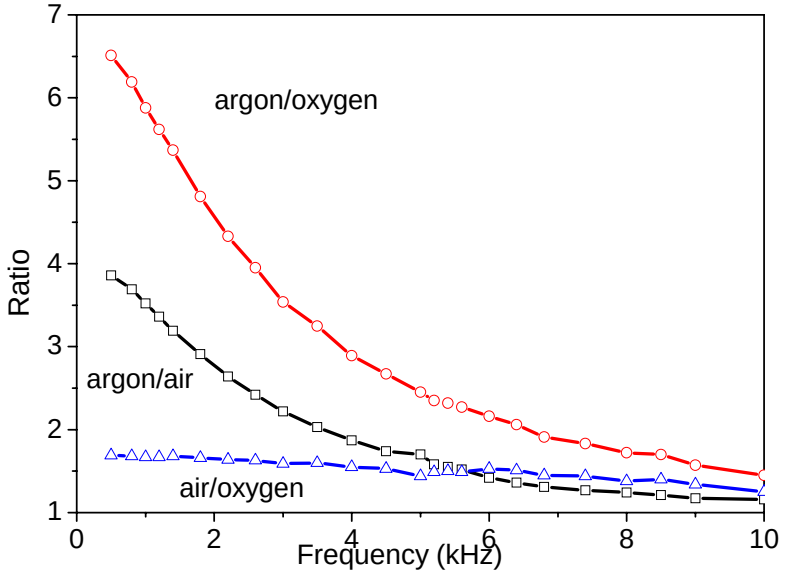

Figure 8.45: Effect of frequency on sensitivity ratio

The decrease of the response ratio with increasing frequency can be explained by the reduction of integrated light intensity due to the prolonged PL decay lifetime of the oxygen sensitive poryphyrin dye. The explanation is further clarified by the effect depicted in figure 8.46.

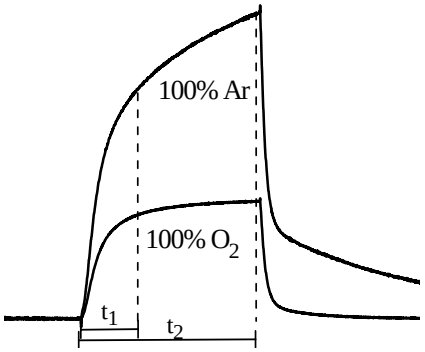

Figure 8.46: Decreasing integrated intensity with higher frequency

The higher frequency results in lower time t_1 and hence a lower difference in intensities. The dye PdOEP has a PL decay lifetime of 1ms. Hence for a frequency higher than 500Hz, we should start seeing a reduction of ambient response ratios as we observe in the previous plot

8.7.2 Effect of OLED generated noise on sensitivity

The low ratio was a result of some noise stemming from the OLED, which was acting as the background for the detection and hence resulting in lower sensitivity. To verify the noise theory, we applied voltage to the OLED and just put the floating probes on top of the OLED, which was then connected to the amplifier with same gain as used for actual measurement as shown in the figure 8.47.

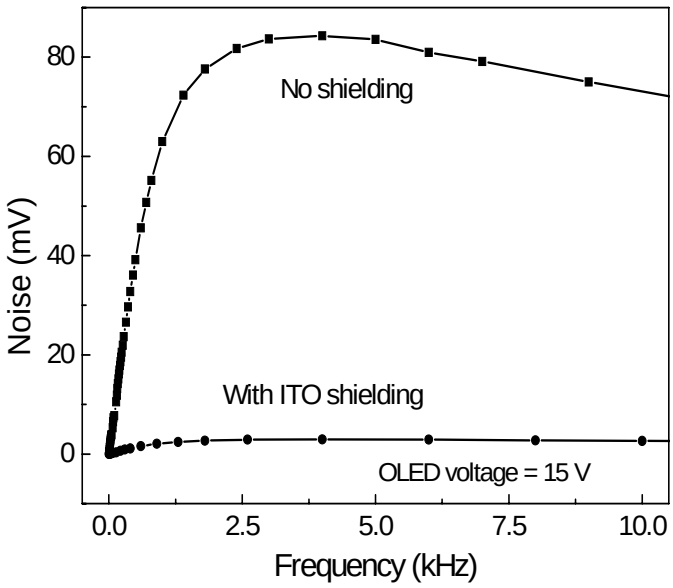

Figure 8.47: Efficacy of noise shielding

Ideally with no photodiode, there shouldn't have any effect, but actually indeed we se the effect of noise which also increased with the degradation of OLED with time resulting in similar noise levels, but reduced OLED intensities at similar applied voltages and hence resulting in lower SNR. Noise was also seen to be dependent on the applied frequency to the OLED as shown in the figure 8.48.

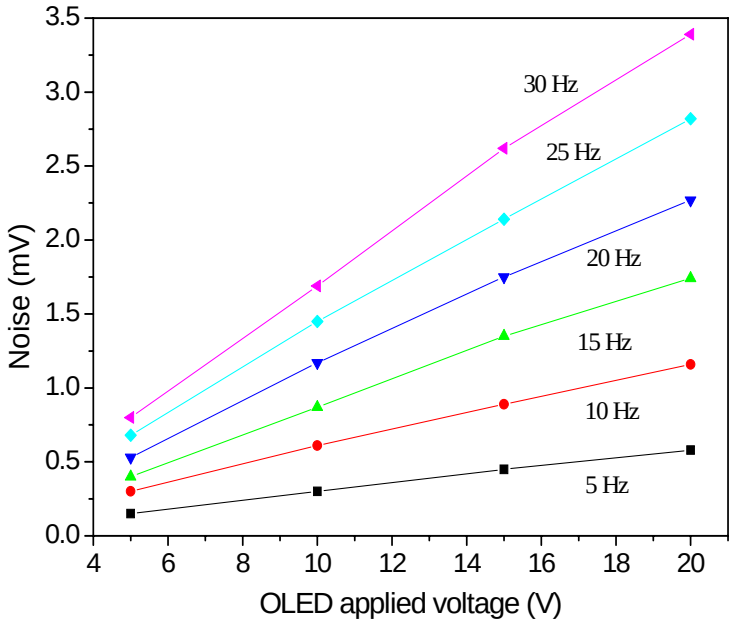

Figure 8.48: Effect of applied voltage frequency on OLED generated noise

8.7.3 Shielding of OLED noise

It necessitated a shielding technique, which has to allow passage of light, and should provide the electromagnetic shielding as well. We had to move for ITO coated glass substrates which when grounded, can significantly reduce the noise levels with very less interference to the light compared to using thin metal or metal meshes. The ITO substrates we used for fabrication was used itself for this purpose and it was then grounded it make it an effective shield as shown in the figure 8.49.

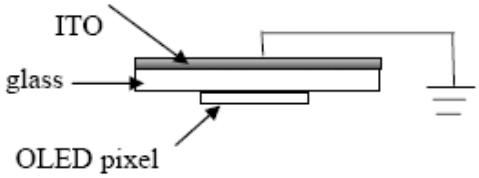

Figure 8.49: Shielding mechanism

On experimenting with the response at different ambient with single shield resulted in better results especially for higher excitation frequencies as shown in the figure 8.50.

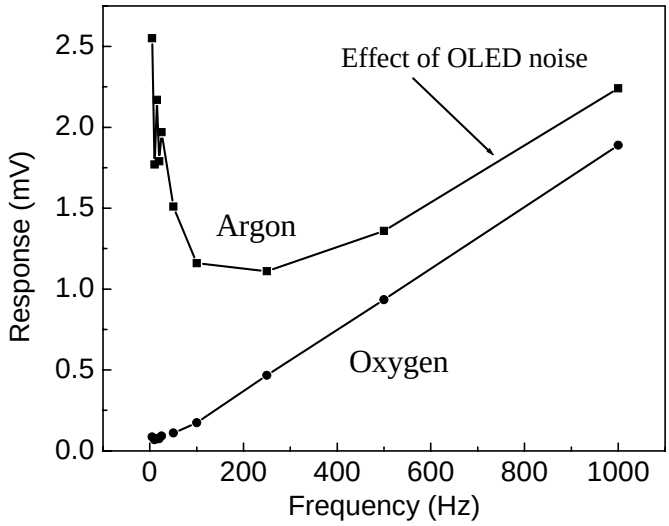

Figure 8.50: Sensor response with single shield

With the single shield configuration sensitivity at lower frequency was enhanced to about 19 compared to 7 obtained before. This was a significant improvement in the sensor performance. We observe that still the noise starts to dominate above 100 Hz, which is clearly observed in the oxygen ambient and is prominent in the argon ambient too. The magnitude of response in argon ambient being larger results in lower percentage effect of the noise.

It was observed that using a double shield with two ITO layers in contact sandwiched between glass substrates gave better shielding capabilities due to higher overall conductivity of ITO enhancing the electromagnetic shielding as shown in the figure 8.51.

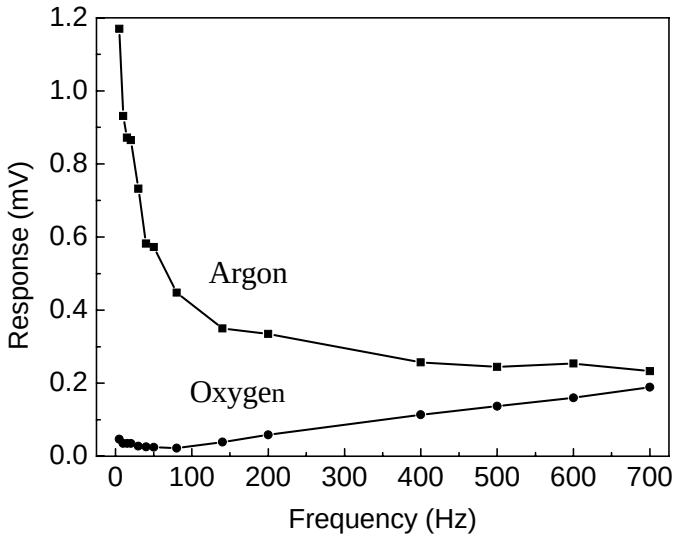

Figure 8.51: Sensor response with double shield

The sensitivity is further increased to 25 with the double shield configuration. We see that the argon response is almost unaffected by the noise, but we indeed see some effect in the oxygen response. On using a coumarin-doped OLED with narrower response shown in previous section resulted in further improvement of sensitivity to 47 as shown in the figure 8.52.

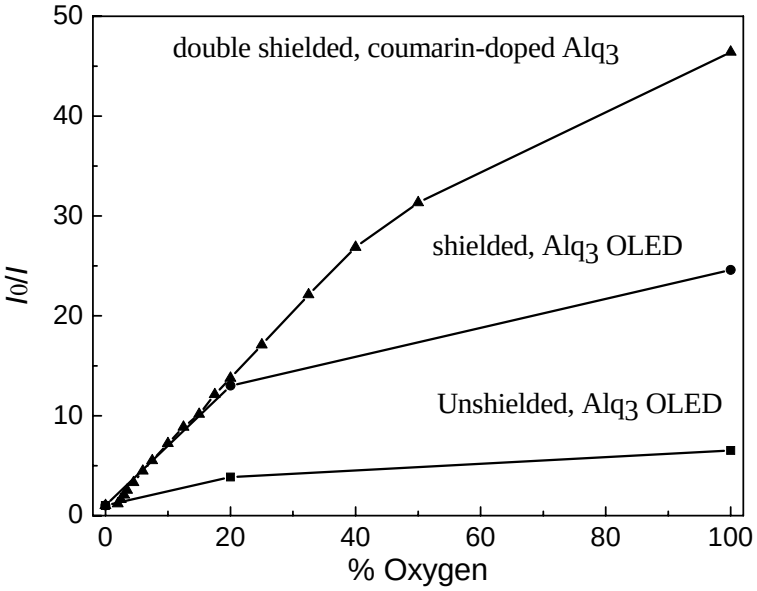

Figure 8.52: Improved sensitivity with coumarin doped OLED

Our next target was to move on to the photoluminescence decay lifetime based measurements requiring faster photodiode response. We move to nanocrystalline devices to have even better response with higher mobility and hence a faster expected frequency response.

8.8 Nanocrystalline devices

For the nanocrystalline films, we observe that the film quality is very much dependent on the previous deposited layers. So we grew the nanocrystalline silicon layer in an undoped reactor and that substantially improved the quality of the film. The growth of nanocrystalline silicon is conical is structure as proposed by Collins et. al [45].

8.8.1 Effect of hydrogen dilution

The QE and the I-V were dependent on the crystallinity of the devices as shown in the figure 8.53.

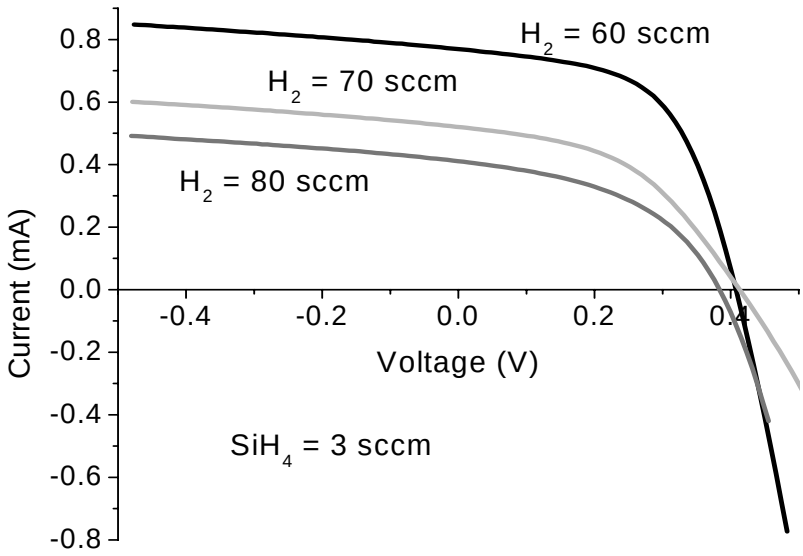

Figure 8.53: Effect of crystallinity on I-V

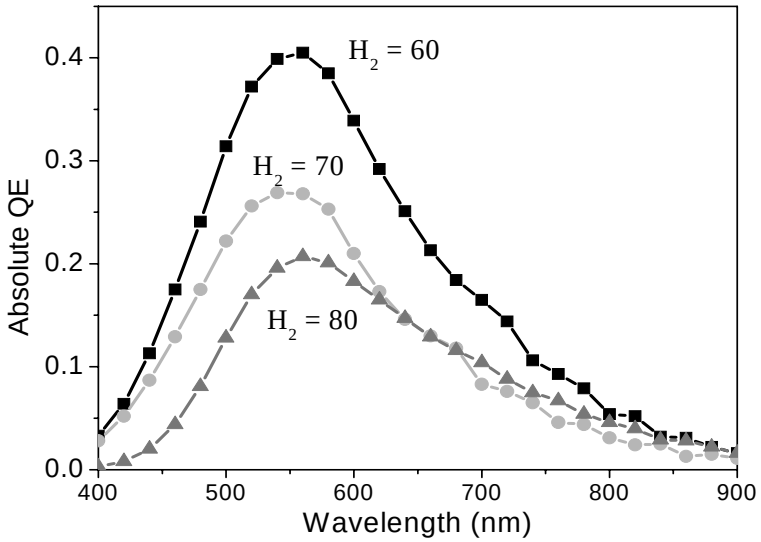

Figure 8.54: Effect of crystallinity on QE

We see that the current as well the absolute QE goes down with increasing crystallinity with higher hydrogen dilution. Also the diffusion length goes from 1.587 μm → 0.547 → 0.014 μm and this indicates the increase of defect density with higher hydrogen dilution.

8.8.2 Factors affecting frequency response of nanocrystalline devices

We measure the frequency response of the nanaocrystalline device in contrast to the amorphous devices grown using VHF plasma. It was observed that the nanocrystalline device was indeed faster than the amorphous devices. But at lower frequency we see the effect of grain boundary defects dominating the frequency response resulting in a sharp decrease of the response to lower frequencies.

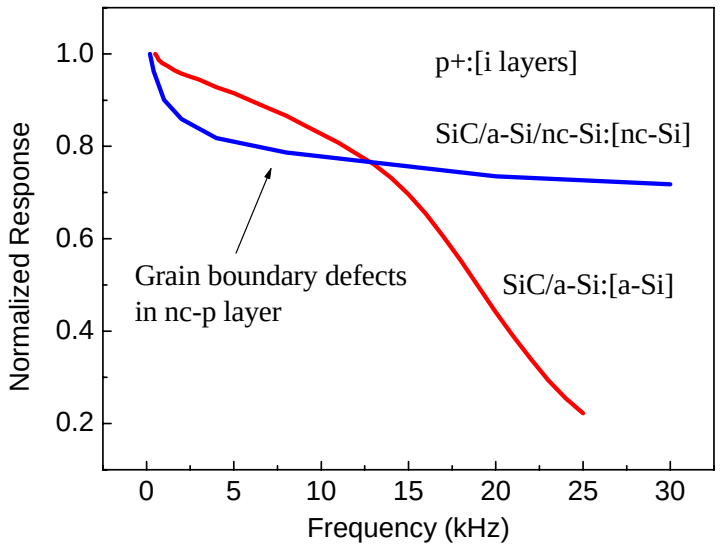

Figure 8.55: Effect of grain boundary defects in frequency response

In addition to that we also see that the frequency response is also bit dependent on the thickness of the p layer used. It was seen that the response was especially dependent on the thickness of the nanocrystalline p+ layer. Hence to prove that similar devices were grown with identical n+ and I layer. The only difference in p layer was one grown with a thicker nx-Si p+ compared to the other. The result is shown in the figure 8.56.

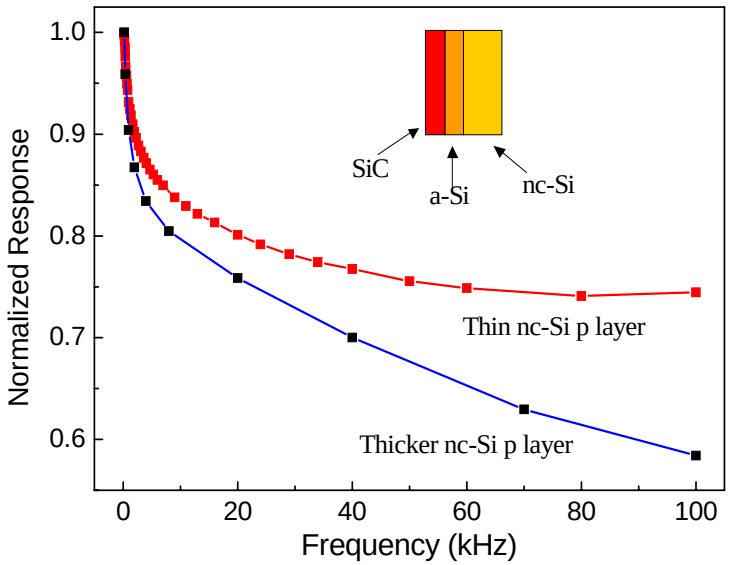

Figure 8.56: Effect of nx-Si p layer thickness frequency response

8.9 Sensor performance in the frequency response mode

The sensor was first characterized using commercial crystalline silicon Hamamatsu photodiode along with the shielding techniques described above with OLED excitation. The initial calibration showed quite encouraging results as shown in the figure 8.57.

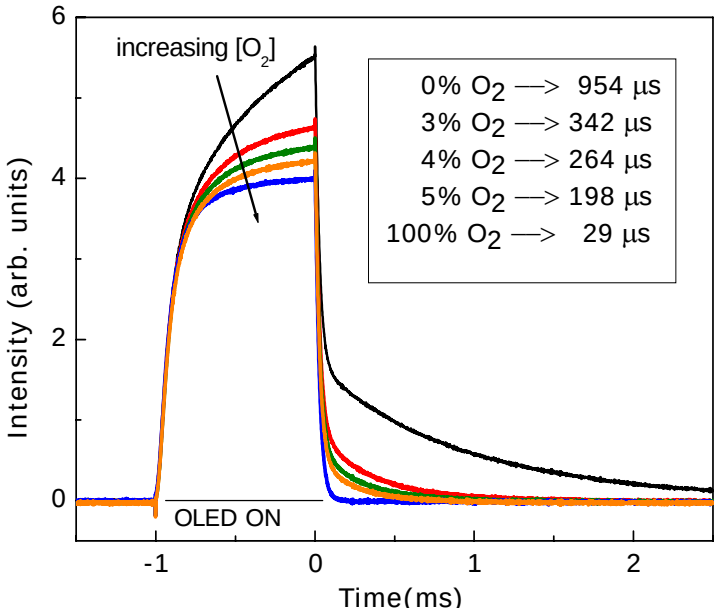

Figure 8.57: Sensor operation in the lifetime mode

We can observe that there is a significant difference between the oxygen concentrations in the lifetime mode at different ambient. The difference during the OLED pulse is indicator of the response in the intensity mode. But the difference obtained is lower since in this case only the longpass filter was used and hence enhancing the OLED background. But that was immaterial in the lifetime mode of detection. On using both the filters the signal was too weak to detect. The lifetimes were calculated using a double exponential. Two lifetimes were obtained with this fit with one of the time constant remaining same to about 25 µs which corresponds to the measurement system's response time including the current amplifiers and other equipments. The formula used was:

$$I = I_o + A\exp(-t/t_1) + B\exp(-t/t_2)$$

The double exponential was very important for the decay time estimation especially at high oxygen concentrations.

8.10 Nanocrystalline passivation using amorphous silicon

The nanocrystalline layers suffer from grain boundary and surface defects, which affect the response speed and sensitivity of the photodiode. We observed improved performance on incorporating passivation layers to reduce the defect density in the thin film material. A nanocrystalline layer was grown followed by a very thin passivation layer by varying the plasma power level during the thin film VHF PECVD deposition using programmable HP8116 pulse generator.

The nanocrystalline layer thickness was kept constant and the thickness of the amorphous layer was varied with similar gas, power, temperature and pressure condition. With H_2 = 60 and SiH_4 = 25 @ 300^0C temperature. The varying amorphous layer thickness, provide various degrees of passivation. They are summarized in the table below:

Sample No	nx-Si deposition time	a-Si deposition time	Cycles	Thickness	Crystalline/ amorphous ratio
6001	50 s	10 s	100	1.42 μ	4.18
6002	50 s	20 s	86	1.32 μ	4.13
6003	50 s	40 s	67	1.09 μ	4.14
6004	50 s	80 s	46	0.99 μ	4.02

The reduction in intensity of the peak is due to the increase of amorphous content resulting in lower Raman signature. The effect is more prominently visible in the XRD for the samples as shown in the figure 8.58.

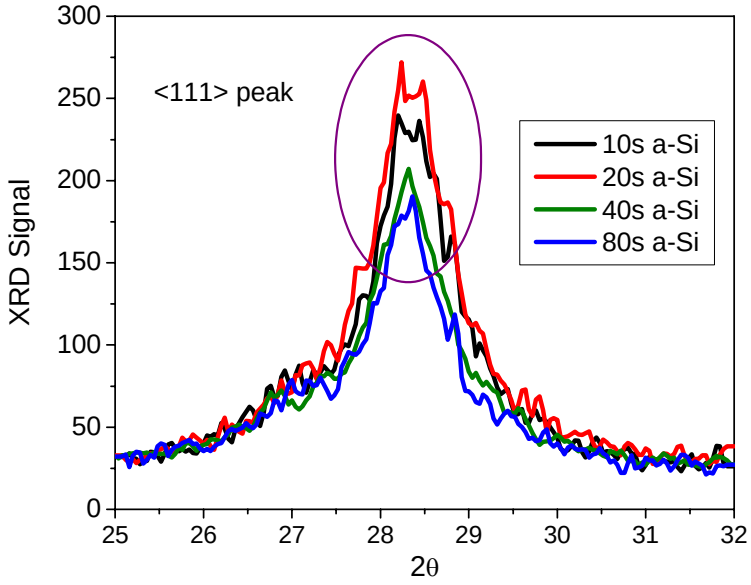

Figure 8.58: XRD change with higher amorphous content

The <111> peak intensity continues to go down due to the reduction of crystallinity in the films with higher amount of amorphous phase. Similar reduction was also observed for <220> peaks. Also we see that the thickness reduces with more cycle time for amorphous, indicating that the growth rate of amorphous silicon is slower than that of nanocrystalline silicon. So after performing multivariate linear regression analysis, the growth rate comes out to be 1.1 A/s for a-Si and 2.42 A/s for nx-Si.

8.10.1 Effect of amorphous phase on electrical properties

We observe that the device performance is better if there is more amorphous tissue present, which may be due to better surface passivation. It has been seen before that hydrogen passivates the grain boundaries in silicon [53]. The I-V QE characteristic is shown in the figure 8.59.

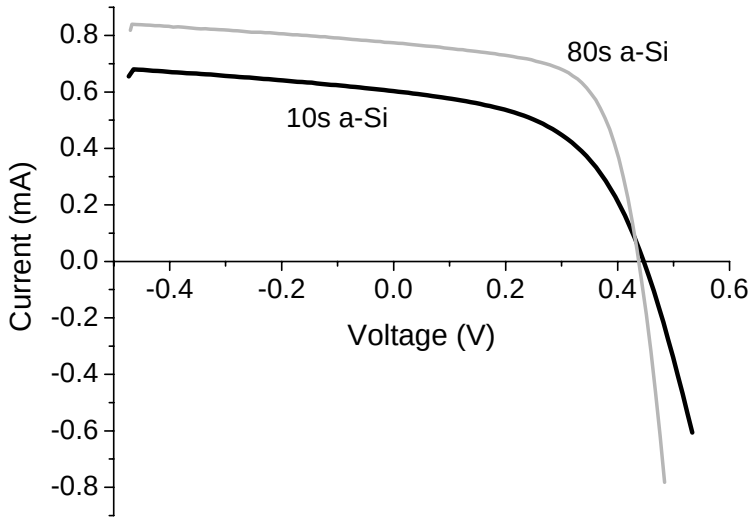

Figure 8.59: Effect of amorphous phase on IV

The improvement of the current also shows up as an increase in the QE of the devices as shown in the figure 8.60.

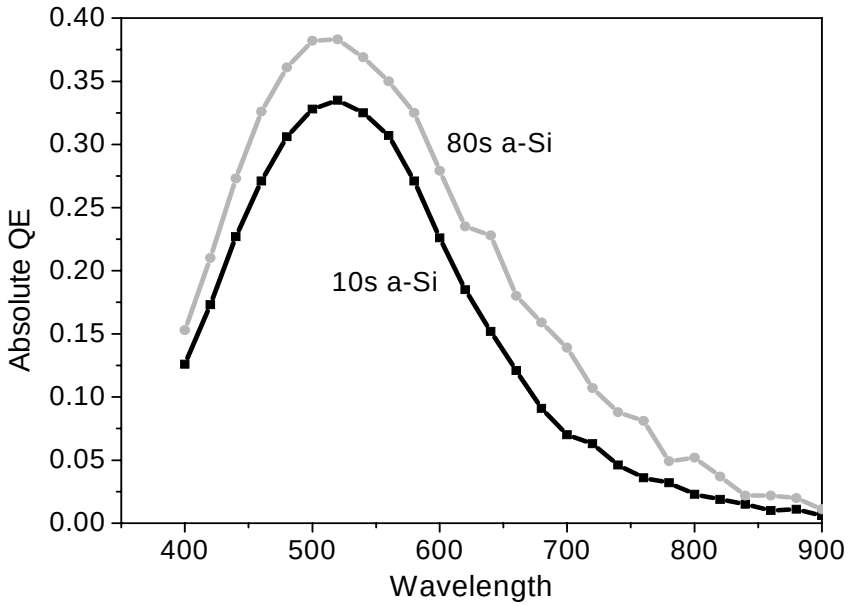

Figure 8.60: Enhanced QE with higher amorphous content

The lower recombination in I layer for 80s a-Si passivated device was validated by the diffusion length measurements, with 3.06 microns compared to 0.062 microns for 10s a-Si passivated device. Also the defect densities measured by capacitance measurements is

$2.5x10^{16}/cm^3$ compared to 6.25 $x10^{16}/cm^3$ for 9935. All these evidences indicate towards better surface passivation, hence reducing grain boundary recombination and scattering.

8.10.2 Effect of amorphous phase on frequency response

The effect on frequency response was also observed and the device responded faster with better passivation. A series of four devices were made with 10s, 20s, 40s and 80s amorphous layers. The frequency response also improved indicating better passivation is shown in figure 8.61.

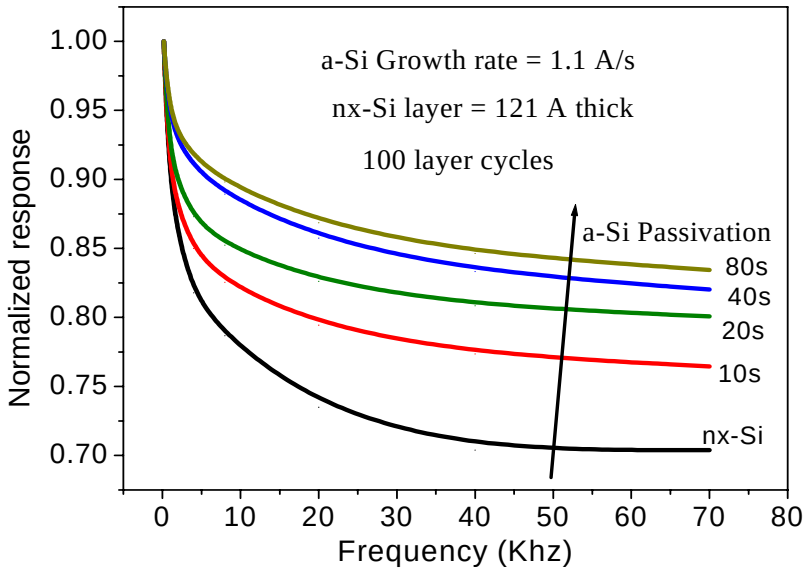

Figure 8.61: Frequency response improvement with passivation layers

8.10.3 Effect of TMB and hydrogen grading

We study the films for same deposition temperature at different condition with film thickness of 0.3 μm for all devices as shown in the table below:

Sample No	Grading	H_2	SiH_4	nx-Si deposition time	a-Si deposition time	Grain size <111>	Grain size <220>
6032	TMB grading	60	25	50 s	80 s	8.3 ± 1 nm	7.6 ± 0.8 nm
6034	No grading	70	20	50 s	80 s	9.3 ± 1.2 nm	

6035	H_2 grading	70	20	50 s	80 s	7.3 ± 0.8 nm	9.1 ± 1.1 nm

We can see that the grain size reduces on TMB grading though the film. On comparing 6032 with 6004, we that that the cycle time period is different for them, but the ratio is same. 6032 has TMB grading. So if 6032 was for 46 cycle, it would have been 0.3*(46/20) = 0.69 μm, but 6004 is actually 0.99 μm thick. So TMB grading also reduces the growth rate of the film.

From the data comparing 6034 and 6035 we see that H_2 grading actually decreases the grain size. The devices were studied for different cycle times with hydrogen and TMB grading as both of them results in lower grain size. The temperature was 250C and H_2 was 60 and SiH_4 was 25 with pressure 100mT during the deposition. So two devices were made, one with 50s-nx/80s-a-Si (sample 10032) and other with 50s-nx/50s-a-Si (sample 10045) for same deposition time. The hydrogen and TMB graded device is comparatively poorer in performance compared to the non graded one at 275C.

CONCLUSION

The PECVD grown thin film photodiodes were optimized for the efficient and high sensitivity when integrated with OLED and sensor dye to fabricate the integrated oxygen sensor. Integration issues relating to the noise stemming from the OLED was solved using appropriate optically transparent electromagnetic shielding technique.

The photodetector device performance was found to be dependent on the growth temperature, pressure and the composition of layers. Bandgap engineering was implemented to tune the sensitivity and wavelength selectivity. It was observed that addition of Ge in I layer deteriorates the electrical properties and hence the device performance. The addition of Ge to the p+ layer was to achieve a higher wavelength QE spectrum, but resulted in a worse device performance due to higher dark current. Thick p layers resulted in desired lower sensitivity at lower wavelengths, but at the same time it also resulted in reduced QE. It was also observed that addition of SiC at p-I interface reduces the dark current by order of magnitude, but also reduces the QE.

ZnO protective layer grown at higher power results in increased dark current in the devices due to the porous structure of ZnO, hence a lower power grown ZnO being denser results in better quality thin film deposition on top of it. Making a mesa structure using reactive ion etching also reduces the dark current further. The sensor dye PtOEP is less sensitive to oxygen compared to PdOEP. Also the TiO_2 doping further enhances the response from the film. The locking method of measurement is more efficient compared to other methods due to better noise immunity. Also the sensor response ratio is independent of the intensity of excitation. The intensity mode detection suffers from the reliability problems due to background and degradation effects. But still a sensitivity of 47 was achieved for integration with OLED.

The frequency response for the photodiode was important for the lifetime mode of measurement with an inherited advantage of filter less, degradation effects immune method of measurement. But the measurement is more complicated requiring faster photodiode response. The factors affecting the frequency response were studied and it was observed that

the boron diffusion at the p-I interface was dominantly affecting the frequency response. The ECR grown devices were slower due to higher deposition time due to lower growth rate compared to VHF growth. Also nip devices configuration was faster compared to pin device further confirming the boron diffusion. This diffusion could be partially checked by drafting SiC at the p-i interface. TMB grading of I layer was seen to be detrimental for the photodetector's performance even-though it resulted in higher short circuit current and faster response.

Nanocrystalline photodetectors were faster than amorphous silicon counterparts due to higher carrier mobilities. But dark current was higher due to lower bandgap. The nanocrystalline devices were observe to be very sensitive to the hydrogen dilution, where higher dilution resulted in improper grain boundary passivation and hence higher recombination centers. The nanocrytalline defects in the p layer responds significantly and have a prominent effect at lower frequencies. The passivation was improved using amorphous passivation layer resulting in lower defect densities and faster response which was obtained with proper passivation.

FUTURE WORK AND DIRECTIONS

For the future work, the frequency response of the photodiodes needs to be improved further for implementation with the oxygen sensor working in the lifetime mode. Appropriate circuitry for the analysis of the lifetime data also needs to be designed for better readout and faster analysis resulting in lower response time. Also the shielding techniques have to be implemented along with the edge emission removal in the final integrated patterned structure. Inspite of sensitivity of around 47 obtained in the intensity mode, the lifetime mode has a huge prospect of improvement to sensitivity of about 200.

Proper encapsulation techniques also have to be implemented to achieve a more reliable and longer sensor performance. Also the developed device has prospect of commercialization in the startup Integrated Sensor Technologies Inc. at Ames, Iowa.

PUBLICATIONS FROM THIS WORK

- "Amorphous and nanocrystalline p–i–n Si and Si,Ge photodetectors for structurally integrated O2 sensors", **J. Non Crys. Solids** 354 2606 (2008).

- "PECVD Grown p-i-n Si and Si,Ge Thin Film Photodetectors for Integrated Oxygen Sensors", **Mater. Res. Symp. Proc.** 989, A12-01 (2007)

- "Influence of Amorphous Layers on Performance of Nanpcrystalline/Amorphous Superlattice Si Solar Cells", **Mater. Res. Symp. Proc.** 989, A18-02 (2007)

- "Advances in OLED-based oxygen sensors with structurally integrated OLED, sensor film, and thin-film Si photodetector", (submitted to) **SPIE (Optics & Photonics) Proceedings** (2007)

- "Luminescence-based oxygen sensors structurally integrated with an OLED excitation and an amorphous Si photodetector", **J. Non Crys. Solids** 352 1995 (2006).

ACKNOWLEDGEMENTS

I would like to express my sincere gratitude to my major professor, Dr. Vikram Dalal, for his invaluable guidance and support throughout this research. I would like to thank Dr Ruth Shinar and Dr Joseph Shinar for providing with important guidance and suggestion during the tenure of this work.

I am also honored to have Dr. Rana Biswas, Dr. Gary Tuttle, Dr. Joseph Shinar and Dr. Mani Mina on my committee and would be thankful for their helpful suggestions and review of my work. I am grateful to Max Noack for all his technical help and healthy discussions. I would also like to thank Kay Han and Nanlin Wang for help during sample preparation and fruitful discussions.

I would like to thank Bhaskar Choudhury, Zhoqun Zhao and Yankun Cai for making this collaborative project a success. I also appreciate their patience and understanding with me during the tenure.

I would also like to thank Jane Woline for helping with smooth completion of all official paperwork and celebrating the birthdays with self prepared cakes.

I would like to thank my friends Puneet Sharma, Durga Panda, Kamal Muthukrishnan, Vishwas Jaju, Atul Madhavan, Satya Saripalli, Edward Li and Dan Pates for providing me with the support and encouragement during my course of research.

.

REFERENCES

[1] D. B. Papkovsky, "*New oxygen sensors and their application to biosensing*", Sensors and Actuators B **29**, p.213 (1995)

[2] M. Mulato, Y. Chen, S. Wagner, A. R. Zanatta, J. Non-Cryst. Solids, **266**, p.1260 (2000)

[3] R. Moos, F. Rettig, A. Hurland, C. Plog, "*Temperature-independent resistive oxygen exhaust gas sensor for lean-burn engines in thick-film technology*", Sensors and Actuators B **93**, p. 43–50 (2003)

[4] F. Rettig, R. Moos, "*Direct thermoelectric gas sensors: Design aspects and first gas sensors*", Sensors and Actuators B (2006) in press

[5] J. Ren, H. Zhang, S. Liu, J. Wang, "*Simulations and modeling of planar amperometric oxygen sensors*", Sensors and Actuators B (2006) in press

[6] R. Ramamoorty, P. K. Dutta, S. A. Akbar, "*Oxygen sensors: Materials, methods, designs and applications*", Journal of Materials Science **38, p.** 4271 – 4282 (2003)

[7] F. Garzon, I. Raistrick, E. Brosha, R. Houlton, B. W. Chung, "*Dense diffusion barrier limiting current oxygen sensors*", **Sensors and Actuators B 50,** p.125–130 (1998)

[8] E. I . Tiffee, K. H. Hardtl, W. Menesklou and J . Riegel, **Electrochim. Acta 47,** p. 807 (2001)

[9] T. Kawada ,M. Sase, M. Kudo, K. Yashiro, K. Sato, J. Mizusaki, N. Sakai, T. Horita, K. Yamaji, H. Yokokawa, "*Microscopic observation of oxygen reaction pathway on high temperature electrode materials*" , **Solid State Ionics 177,** p. 3081–3086 (2006)

[10] R. Kocache, "*Gas* Sensors", **Sensor Rev**. **14,** p. 8 (1994)

[11] O.S. Wolfbeis, I. Klimant, T. Werner, C. Huber, C. Kosch, G. Krause, G. Neurauter, A. Du¨ rkop,. "*Set of luminescence decaytime based chemical sensors for clinical applications*". **Sens. Actuators, B, Chem. 51**, p. 17– 24 (1998).

[12] **Hamamatsu Photodiode Technical Information**, (Hamamatsu Photonics K. K., Hamamatsu City, Japan)

[13] D. Caputo, G. de Cesare, A. Nascetti, F. Palma amd M.Petri, '*Infrared photodetection at room temperature using photocapacitance in amorphous silicon structures* ', **Appl. Phys. Lett., 72,** p. 1229 (1998)

[14] J. Wind and G Muller, **Appl. Phys. Lett., 59,** p. 956 (1991)

[15] G. de Cesare, F. Irrera, F. Lemmi and F. Palma, '*Amorphous Si/SiC three-color detector with adjustable threshold'*, **Appl. Phys. Lett.**, **66**, p. 1178 (1995)

[16] S. Morrison, P. Servati, Y.Vygranenko, A. Nathan and A. Madan, **Mat. Res. Soc. Symp. Proc.**, **715**, A7.4.1 (2002)

[17] "Technical Information SD-28" ***Hamamatsu Corp.***

[18] O. M. Nayfeh, S. Rao, A. Smith, J. Therrien, and M. H. Nayfeh, "*Thin Film Silicon Nanoparticle UV Photodetector***" IEEE PHOTONICS TECHNOLOGY LETTERS**, **16**, p.1927 (2004)

[19] http://www.nogi.ch/chemistry/oxygensensor.html

[20] D. B. Papkovsky, "*New oxygen sensors and their application to biosensing*", **Sensors and Actuators B, 29**, p. 213 (1995)

[21] R. C. Evans, P. Douglas, J. A. G. Williams and D. L. Rochester, **Journal of Fluorescence**, **16**, p. 201 (2006)

[22] L.F. Vallvey, L.J. Asensio, J. Gonz´alez, M.D. Ramos, A.J. Palma, "*Oxygen-sensing film coated photodetectors for portable instrumentation*", **Analytica Chimica Acta, (**article in press)

[23] E. Thrush, O. Levi, L. J. Cook, J. S. Harris, S. J. Smith, J. Deich and W.E. Moerner, , **J. Crystal Growth, 284** p. 97273 (1988)

[24] W. Trettnak, C. Kolle, F. Reininger, C. Dolezal, P. O'Leary, "*Miniaturized luminescence lifetime-based oxygen sensor instrumentation utilizing a phase modulation technique*", **Sens. Actuators B 36**, p. 506–512. (1996)

[25] C. McDonagh, C. Kolle, A.K. McEvoy, D.L. Dowling, A.A. Cafolla, S.J. Cullen, B.D. MacCraith, **Sensors and Actuators B 74** p. 124-130 (2001)

[26] V. P. Chodavarapu, D. O. Shubin, R. M. Bukowski, A. H. Titus, A. N. Cartwright, and F. V. Bright, **IEEE Trans. Circuits & Systems 54**, p. 111 (2007)

[27] M. Yoshioka, S. Sato and T. Kikuchi, **J. Lightwave Tech. 23**, p. 2112 (2005)

[28] D. Caputo, G. de Cesare, M. Tucci, **Sensors and Actuators A, 88,** p. 139 (2001)

[29] A. Bogaerts, **Spectrochimica Acta B, 57** p. 609 (2002)

[30] N. Wang, **Ph.D Thesis**, Iowa State University (2006)

[31] J. Meier, E. Vallat, S. Dubail, U. Kroll, J. Dubail, S. Golay, L. Feitknecht, P. Torres, S. Fay, A. Shah, **Solar Energy Materials 66** p. 73-84 (2001).

[32] H. Curtins, N, Wyrsch, A. Shah, Electron Letters **23** p. 228 (1987)

[33] S. Oda, J. Noda, M. Matsumura, **Jpn. J. Appl. Phys**. **29** p. 1889 (1990)

[34] P. Chabloz, H. Keppner, D. Fischer, D. Link, A. Shah, **Journal of Non-Crystalline Solids 198-200** p. 1159-1162 (1996)

[35] M. Surendra and D.B. Graves, **Appl. Phys. Lett. 59** p. 2091 (1991)

[36] A. Howling, J,L. Dorier, Ch. Hollenstein, U. Kroll and F. Finger, **J. Vac. Sci. Technol**. **A10** p. 1080 (1992).

[37] J.Dutta, U.Kroll, P.Chablor. and A.Shah, **J. Appl.Phys. 72 (7)** p. 3220 (1992)

[38] P. Sharma, **Ph.D Thesis**, Iowa State University (2005)

[39] J. Robertson, **J. Non-Cryst. Solids 266-269**, 79 (2000)

[40] C.R. Woronski, "*Electronic Properties of Amorphous Silicon in Solar Cell Operation*", **IEEE Trans. Elec. Dev. 4** p. 351 (1977)

[41] S. Hazra, A. R. Middya and S. Ray, **J. Non Crys. Solids**, **202** p. 81 (1996)

[42] M. E. Gueuniera, J. P. Kleider, R. BrXggemann, S. Lebib, P. R. Cabarrocas, R. Meaudre and B. Canut, **J. Appl. Phys. , 92** p. 4959 (2002)

[43] A. Shah, E. Vallat-Sauvain, P. Torres, J. Meier, U. Kroll, C. Hof, C. Droz, M. Goerlitzu, N. Wyrsch, M. Vanacek, **Materials Science and Engineering B69–70** p. 219–226 (2000)

[44] S. Sriraman, S. Agarwal, E. S. Aydil and D. Maroudas, **Nature**, **418** p. 62 (2002)

[45] R.W. Collins, A.S. Ferlauto, G.M. Ferreira, Chi Chen, Joohyun Koh, R.J. Koval, Yeeheng Lee, J.M. Pearce and C.R. Wronski, **Solar Energy Materials & Solar Cells 78,** p.143 (2003)

[46] R. A. C. M. M. van Swaaji, B. S. Girwar and J. W. Metselaar, **J. Vac. Sci. Rechnol A**, **18** p. 2116 (2000)

[47] P. R. Cabarrocas. **J. Non Crys. Solids, 266 – 269** p. 31 (2000)

[48] L. C. Kimerling, **J. Appl. Phys**. **45**, p. 1839-1845 (1974)

[49] B.D. Cullity, **Elements of X-ray diffraction, Addison-Wesley Publishing Company, Inc. Boston, MA** p. 101-102 (1978)

[50] R. Shinar, D. Ghosh, B. Choudhury, M. Noack, V. L. Dalal and J. Shinar, **J. Non Crys. Solids**, **352** p. 1995 (2006)

[51] G. de Cesare, F. Irrera, P. Palma, E. Jannitti, G. Naleto and P. Nicoloski, "*Amorphous silicon/silicon carbide photodiodes with excellent sensitivity ans selectivity in the vacuum ultraviolet spectrum*" **Appl. Phys. Lett 67,** p. 335 (1995)

[52] T. Matsui, T. Fujibayashi, Y. Nasuno, H. Fukuhori, Y. Kanemitsu, M. Kondo and A. Matsuda, **3rd World Conference *on Photovoltaic* Energy Conversion**, **5P-D4-29**, (2003) 1831

[53] I. Martın, M. Vetter, A. Orpella, C. Voz, J. Puigdollers, R. Alcubillaa, A. V. Kharchenko and P. R. Cabarrocas, **Appl. Phys. Lett.** , **84** p. 1474 (2004)